UCLouvain

AGRO LOUVAIN

Faculté des bioingénieurs

Modelling the influence of organic acids and rainfall inputs on the weathering of a volcanic ash deposit: a case study in the northern Ecuadorian Andes

Auteur : Junique Marion

Promoteur(s) : Pr. Delmelle Pierre (UCLouvain/ELI/ELIE)
Dr. Calispa Marlon (UCLouvain/ELI/ELIE)

Lecteur(s) : Pr. Perez Fodich Alida (University of Chile/ Geology Department)
Pr. Vanacker Veerle (UCLouvain/ELI/ELIC)

Année académique 2020-2021
Mémoire de fin d'études présenté en vue de l'obtention du diplôme de Bioingénieur : Chimie et bio-industries

Abstract

The páramo in the tropical Andes is notable for its large water retention capacity, its high soil carbon content and rich biodiversity. The resulting ecosystem is the main source of water for many large Latin America cities. The current climate change affects these regions with predicted rainfall pattern alterations. In addition, human activities may lead to modifications in vegetation cover. However, very little is known about the impact of such changes on the weathering of the páramo soils. In this study, we innovatively used the reactive transport model approach to simulate the chemical weathering of a volcanic soil under different rainfall inputs and vegetation covers. We focus on the páramo of the Antisana region in northern Ecuador. Its soils developed on the ash deposit from the 800 years B.P. eruption of Quilotoa volcano.

Successive model versions were iteratively elaborated to progressively correspond to actual measurements of soil chemistry. The computer simulations were run using the Crunchflow engine and were based on a 1 m dacitic porous ash deposit reacting with an aqueous solution of rainfall composition (infiltration rate: 0.4 m/yr).

In order to take into account the soil respiration effect and to reproduce the pH values of the field soil solution, the CO_2 had to be increased 100 times (30 000 ppmv) compared to atmospheric CO_2. Due to the acidity consumption by the primary solid phases weathering, the pH increases with depth and decreases with time. Thus, the concentrations of $SiO_{2(aq)}$, Ca^{2+}, Mg^{2+}, Na^{+} and K^{+} increase with depth and decrease with time. Free Al^{3+} is the only cation which concentration decreases with depth and increases with time. Allophanes and gibbsite precipitation are visible.

Then, to represent the two different vegetation types, i.e. tussock-like grasses (TU, low DOC) and cushion-forming plants (CU, high DOC), oxalic acid was incorporated in the weathering solution in two different DOC concentrations. The soil solution pH under CU is lower and the mobilisation of Al is stronger, compared to under TU. Allophanes are the only secondary solid phases that precipitate (∼12 %v at 5 kyr).

Once the model was tuned, different water flows were tested to study the impact of changing precipitation patterns on the soil solution and mineralogy. A double rainwater flow decreases slightly the soil solution pH under TU and up to 1.5 units under CU. It also decreases the concentrations of $SiO_{2(aq)}$, Ca^{2+}, Mg^{2+}, Na^{+} and K^{+} in solution, with a soil solution almost free of Ca^{2+} and Na^{+} after 5 kyr of weathering, but with a free Al^{3+} concentration at the bottom of the profile is 100 times higher under CU than under TU. The depth at which the allophanes precipitate is also lowered by respectively, 5 and 25 cm under TU and CU. On the contrary, decreasing the flow by half has an opposite effect: the pH and the dissolved element concentrations increase and the allophanes precipitate at shallower depths.

Further studies need to be carried out including for extrapolating consequences on the ecosystem and in particular on its water quality. However, it is also essential to significantly enrich the actual field data to further tune the model, specifically regarding pH, soil solution chemistry, as well as a robust determination of the water infiltration rate.

To the Andean populations,

with hopefully in the future a *digital twin* of the páramo

to understand how to protect it and exploit it safely.

Acknowledgements

To start with, I would like to show my deepest gratitude to my master thesis supervisor, Pr. Pierre Delmelle. I thank him for sharing his expertise and giving me judicious advice. His continuous feedback helped me to elaborate my thinking and to keep a higher vision on the required approach. Thank you also for your good mood and dynamism. Arigato!

To continue, I am also deeply grateful to Dr. Marlon Calispa, my co-supervisor. He was always enthusiastic and willing to assist me in any way he could throughout all the steps of the project. His contribution was essential for the development of the RTM. Muchísimas gracias por tu disponibilidad y tu paciencia Marlon!

I would like to extend my sincere thanks to my two readers: Pr. Alida Perez Fodich and Pr. Veerle Vanacker, for spending time reading this dissertation. Thank you Alida for sharing your knowledge and for providing insightful suggestions to this thesis.

This work is part of the ARES-funded PRD project “Paramosus”. The Ecuadorian project partners FONAG (Fondo para la protección del Agua) and EPMA (Empresa Pública Metropolinata de Agua Potable y Saneamiento de Quito) have provided access to the field site at Antisana since 2017. This allowed collection of the data utilised in this study.

To continue, I would like to express appreciation for Maxim Wirard. Throughout a big part of the thesis we worked together as he was doing his dissertation on another dimension of the páramo. His optimism and support were essential for the completion of this dissertation. Merci!

I also wish to thank my father for his wise counsel and for proofreading this thesis. I am grateful to my mother for her support throughout my whole studies. Thank you to my brother and sister for their encouragement.

Last but not least, I would like to offer special thanks to all my friends and my boyfriend Adrien, for their unwavering support and belief in me. They made my studies and life at university so bright and memorable. Thank you so much!

Table of Content

List of Tables

List of Figures

1. Introduction

The páramos are tropical high-altitude ecosystems found mostly in the Andes (Podwojewski and Poulenard, 2004). Owing to their outstanding capacity to regulate water fluxes and quality, they provide a crucial ecosystem service to large South American cities, including Quito in Ecuador (Crespo et al., 2010). Moreover, the páramos play other key environmental roles such as storing remarkable amounts of carbon and sheltering many endemic species (Correa et al., 2020). These environmental services relate predominantly to the unique properties of the volcanic soils on which most Andean páramos have developed. In particular, these soils, which are mainly Andosols (Poulenard et al., 2001), drain well but also retain water efficiently (Shoji, 1985). This is due to their exceptional capacity to stabilise organic matter (OM) via aluminium and/or iron complexation, interactions with the surfaces of secondary solid phases (allophanes and ferrihydrite) and physical protection in aggregates (Shoji et al., 1993c).

Anthropogenic activities have taken place for thousands of years in the Andean páramos (Correa et al., 2020). Since the last century, the páramos have been increasingly utilised for agricultural and touristic activities, while being subjected to rapid climate changes (Hofstede et al., 2014). In the next century, the global surface temperature is projected to continue to rise (IPCC, 2014). This will likely be accompanied by changes in the precipitation regime. Although, it is not yet entirely clear how this will affect the high Andes, some studies suggest that the annual rainfall will increase across most of the tropical Andes (Herzog et al., 2011). A variety of impacts linked to these anthropogenic and environmental stresses on the páramo have already been observed. They take the form of increased evapotranspiration, increased soil density and reduced porosity, reduced water regulation and storage capacity (Correa et al., 2020) and changes in vegetation (Podwojewski et al., 2002).

However, many uncertainties subsist regarding the processes underpinning the changes that are taking place in the Andean páramo (Buytaert and De Bièvre, 2012). In this context, obtaining a process-based understanding of the impacts on soil properties and functioning is a key priority. Such knowledge would certainly contribute to improving the management of páramos in order to protect them efficiently (Buytaert et al., 2006b).

In this dissertation, we select a geochemical modelling approach to investigate how Andean páramo soils may respond to climate change-related rainfall patterns. More specifically, we innovatively use a reactive transport model (RTM) to simulate the weathering of a volcanic soil under different hydrological conditions and soil solution compositions. The study focuses on the Jatunhuyacu catchment in the Antisana region, north Ecuador. The catchment is characterised by two main types of vegetation cover, i.e. tussock-forming grasses (TU) and cushion-like plants (CU). The latter may have gained importance over time due to previous utilisation of the páramo for cattle grazing (Podwojewski et al., 2002).

The specific objectives of our research are: (1) to parameterise a model that can simulate the chemical weathering of a ash deposit; (2) to apply this model in order to assess the evolution of the páramo soil solution chemistry and solid phase composition as weathering progresses with time; (3) to determine the influence of water flow on soil weathering and (4) to quantify the effect of dissolved OM on soil weathering.

2. State of the art

2.1. The Ecuadorian páramos

2.1.1. General description of páramos

Páramos are tropical alpine ecosystems present at high altitudes. They most prominently extend from 11°N in Venezuela to 8°S in Peru, in the Northern Andes (Figure 1). They are also found to a smaller extent in Central America (Correa et al., 2020). They are located between the upper limit of the montane cloud forest and the permanent snow line (Christmann and Oliveras, 2020), i.e. at altitudes between ~ 3500 and 5000 m, depending on the region (Buytaert et al., 2011). Páramos are categorised into three main zones according to altitude: the sub-páramo, grass páramo (the páramo at *sensu stricto*) and supra-páramo (Christmann and Oliveras, 2020). The total area covered by the páramo is ~ 35 000 km² (Madriñán et al., 2013). Beltrán et al. (2009) estimates that 5 %, or ~13 000 km², of Ecuador are occupied by páramos.

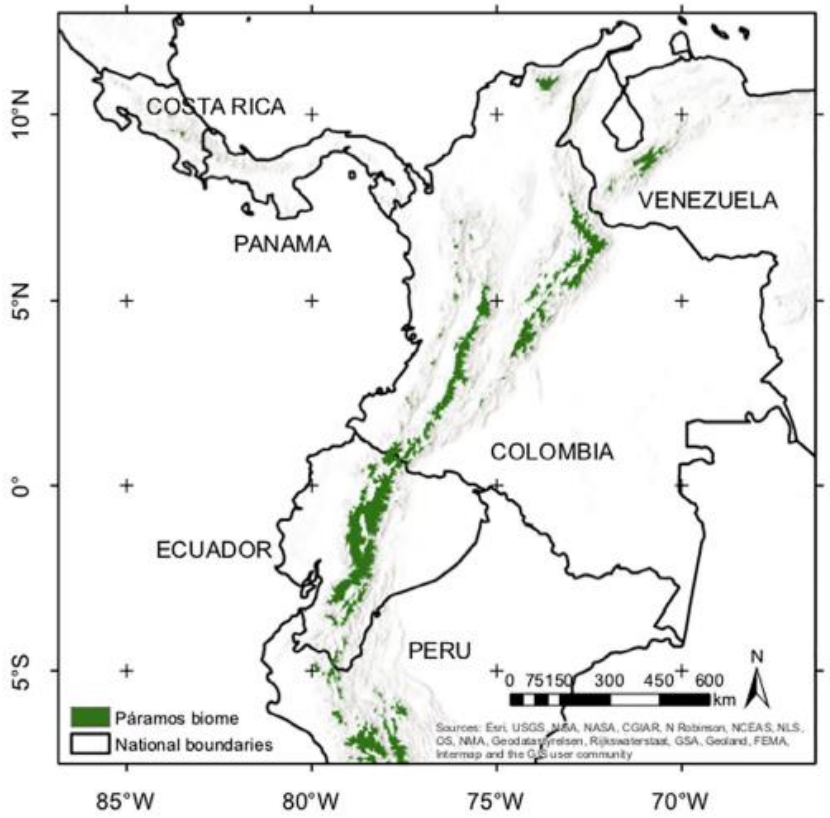

Figure 1. Páramos distribution in the northern Andes and Central America ***(Correa et al., 2020)***

Páramos are humid ecosystems with typical annual rainfall ranging from ~ 1000 to 2000 mm, although they can be found in wetter or drier environments with rainfall exceeding 3000 mm/yr, or as low as 500 mm/yr. In addition to rain, fog, dew and interception by plants also bring humidity (Buytaert et al., 2006a). The mean annual temperature (MAT) varies with altitude: it ranges from ~ 10 °C at lower altitudes to 0 °C at the upper limit. Due to the low latitude and near-constant solar radiance intensity through the year (Buytaert et al., 2011), the seasonal

temperature variability is limited. Nevertheless, large temperature fluctuations occur between day and night (Correa et al., 2020). Temperature can reach 20 °C during the day and fall below 0 °C at night (Podwojewski et al., 2002).

2.1.2. Environmental context

The páramo provides important environmental services and as such it represents a socio-economically crucial ecosystem for the Latin American population. For example, it is directly involved in the water, carbon and nutrient cycles at a regional level and hence has a direct impact on people livelihood (Correa et al., 2020).

Regulation of water fluxes and quality

The soils of the páramos typically derive from volcanic ash deposits. They generally have a high water retention and hydraulic conductivity and are held responsible for páramo's capacity to regulate water quality and flux (Buytaert et al., 2006a). Many authors have reported low evapotranspiration rates in the páramo (Buytaert et al., 2011), with values ranging from 0.8 to 1.5 mm/d (Célleri and Feyen, 2009). This low rate is due to the low temperatures prevailing at high altitude, frequency of fog events, cloud cover, high relative humidity and the xerophytic vegetation (Buytaert et al., 2011). As a result, conditions favourable to elevated water fluxes can develop in the páramo. Páramo ecosystems are known to produce high-quality waters and to regulate their fluxes. In the Andes, due to the difficulty of extracting groundwater in the highlands, páramo watersheds serve as the main water source for domestic and industrial usages (Buytaert et al., 2006a; Crespo et al., 2010). They are also utilized in hydro-electrical powerplants and for irrigation purposes. Many northern Andes' large cities (e.g., Quito and Bogota) benefit from páramo's waters. About 40 million people depend directly on this water resource (Josse et al (2009) cited by (Anderson et al., 2011)). In Ecuador alone, more than 3 million people take advantage of the páramo as a source of water (Crespo et al., 2010). Yet, the impacts of human water consumption on the long-term sustainability of the páramo are still unknown (Buytaert and De Bièvre, 2012).

Carbon storage

Another major ecosystem service offered by páramos is the high carbon storage capacity (Buytaert et al., 2006a). Most páramos are sustained by volcanic ash soils, i.e. soils developed from volcanic pyroclasts (section 2.2). These soils' A[1] and tephra-buried A horizons store large quantities of humus. According to Nanzyo (2002), up to 200 h kg^{-1} of organic carbon is stored in such a type of soil. This accumulation is mainly due to the formation of organometallic complexes (Al-humus complexes) and/or organo-mineral associations (Tonneijck et al., 2010),

[1] The A horizon corresponds to the soil surface organo-mineral horizon composed of a mixture of mineral and organic materials.

but also to the low redox potential (resulting of wet and cold environment) and the high soil moisture (Carrillo-Rojas et al., 2019) which both slow down the mineralisation of OM.

The páramos are often qualified as fast evolving biodiversity hotspots. Through time, the geographical distribution of the páramos changed in response to glacial and interglacial periods. This resulted in a rapid diversification of species. The páramos contain over 3 500 plant species (Sklenář et al., 2011). Hofstede et al. (2014) estimated that about 628 of them are endemic. The type of vegetation varies with altitude. In the most widely spread grass páramo, tussock grasses are dominant (*Calamagrostis, Stipa and Festuca sp.*) (Figure 2). In the supra-páramo, acaulescent rosettes (e.g. *Werneria nubigena*, *Hypochaeris sessiliflora*) and cushion plants (e.g. *Azorella sp.*, *Plantago rigida*) (Figure 2) are most abundant (Christmann and Oliveras, 2020; Correa et al., 2020). Changes in vegetation have been reported in some páramos (Podwojewski et al., 2002), yet few studies have been published on the likely association between the type of land cover and the water infiltration in the páramos (Benavides et al., 2018).

Figure 2. Tussock-forming grasses (left) and cushion-like plants (right) in the Antisana páramo (by Marlon Calispa)

2.1.3. Vulnerability of the páramo to climate change and anthropogenic activities

The páramos are under increasing pressure due to climate change and population growth (Buytaert and De Bièvre, 2012). In the tropical Andes, the water demand is predicted to rise by 50 % by 2050 due to population growth (Buytaert and De Bièvre, 2012). Despite their crucial socio-economic roles, the páramos are among the least studied ecosystems (Flores-López et al., 2016). Thus, a better understanding of the impacts of the environmental and anthropogenic threats is urgently required.

Impacts of anthropogenic activities

Humans activities have taken place in the páramos for thousands of years, but it has intensified since the early 20th century (Correa et al., 2020; Harden, 2006). The main anthropogenic activities are livestock grazing, cultivation, afforestation, road construction and building activities (Crespo et al., 2010). These activities directly affect the water supply function of the páramo and may consequently impact significantly its hydrological behaviour (Hribljan et al.,

2016). Among these activities, changes in the land-use cover of the páramos could result in a lowered water availability and quality (Ochoa-Tocachi et al., 2016) as well as to a net flow of carbon from the soil to the atmosphere (Tonneijck et al., 2010).

Soil erosion and degradation of the natural vegetation significantly influence the soil properties, water retention capacity, quality of the superficial and infiltrated water, nutrient losses and OM decomposition (Morales et al., 2007). The removal of the "natural" vegetative cover will increase evaporation, and could result in an irreversible degradation of the soil structure and in a loss of water retention capacity (Buytaert et al., 2006a).

Human activities, such as livestock grazing and contemporary agriculture, can also cause soil compaction, modify rainfall infiltration rate and patterns, and alter runoff (Harden, 2006). Soil compaction reduces soil porosity and hence its ability to store water. Overgrazing can also lead to a vegetation change (tussock grasses being replaced by short carpet grass vegetation) and to an increase in bare land amount (Podwojewski et al., 2002) and thus variations in the infiltration rate. Benavides et al. (2018) found that the highest infiltration rates are found in soil under tussock grasses. In their study, Podwojewski et al. (2002) reported that intensive grazing also produces important changes in the mineralogical, physical and chemical properties of the soil, thereby threatening the important environmental services provided by the páramos. These changes result in a severe decrease in water retention capacity, a loss of water flux regulation capacity and a reduction in carbon storage.

Climate change impacts

For more than half a decade, a rapid climate change has been observed in the tropical Andes region. Amongst the effects observed are: precipitation pattern change, extreme events (e.g. droughts and flooding), glaciers retreat and plant and shift in animal species range (Herzog et al., 2011). Additionally, a rise in atmospheric temperature of 0.11 °C/decade from 1939 to 1998 and of 0.34 °C/decade from 1974 to 1998 has been recorded (Buytaert et al., 2014). In general, climate change models predict that this temperature rise will continue (Buytaert et al., 2011), with a higher warming rate at high elevations compared to the lowlands (Bradley, 2006).

However, detailed climate change projections for the tropical Andes and how these change the ecosystem service in the páramo are still sorely missing. The Intergovernmental Panel on Climate Change (IPCC) adopted several potential future CO_2 emission scenarios (IPCC, 2014). Among which are RCP2.6 (optimistic) and RCP8.5 (pessimistic) scenarios. Both scenarios predict a rise in temperature and in precipitation compared to the mean temperature and precipitation of 1986 – 2005 period (Figure 3). Most studies seem to agree on the rising trend of temperature but the prediction on precipitation regimes are more variable (Buytaert et al., 2011). Nevertheless, increases in precipitation (Haylock et al., 2006) and precipitation variability are probable (Buytaert et al., 2011). The uncertainty of the predictions in the Andean region are

due to the scarcity of meteorological stations at altitudes above 3000 m a.s.l (Buytaert et al., 2014), the high local variability and the complex topography of the Andes (Buytaert et al., 2011).

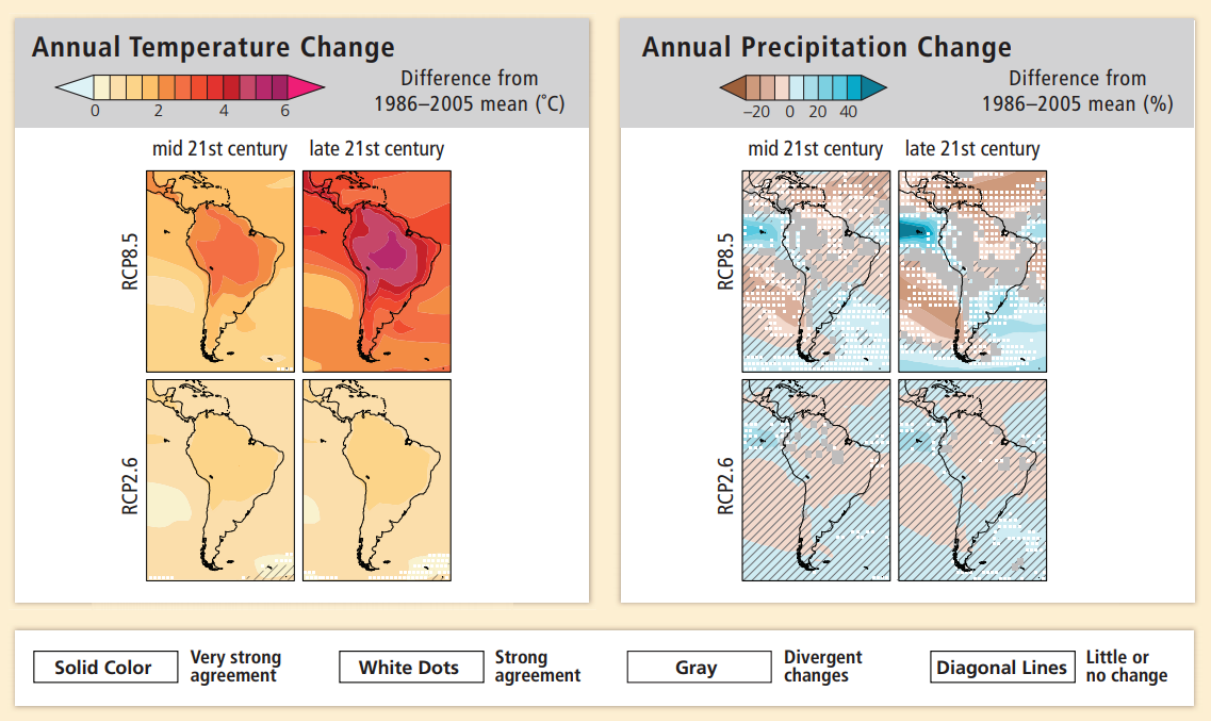

Figure 3. CMIP5 multi-model average projections for 2046 – 2065 and 2081 – 2100, relative to 1986 – 2005, of mean annual temperature (left section) and average changes in annual mean precipitation in percentages (right section), under RCP2.6 and RCP8.5. The analysis employs methods and model data from WGI AR5 Figure SPM.8 (IPCC, 2014).

Evaporation and evapotranspiration will also be affected by climate change. A rise in temperature would contribute to enhance these processes, thereby leading to decreased runoff and groundwater resource recharge (Buytaert and De Bièvre, 2012). Under the A1B scenario (intermediate emission scenario) of the Special Report on Emissions Scenario (SRESS), CIMP3 models predict an increase of 7 % in evapotranspiration in 2079 - 2098 (IPCC, 2014).

Importantly, modifications of the temperature and precipitation regime in the páramo ecosystems will alter the OM decomposition processes. With increasing temperature, the OM decomposition rate may increase and consequently the carbon storage capacity of the soil would be affected (Gutiérrez-Salazar and Medrano-Vizcaíno, 2019).

2.2. Volcanic soils formation and development

The majority of the páramo soils have a volcanic origin (ISSS Working Group RB, 1998) and most of these volcanic soils are ash derived Andosols (Delmelle et al., 2015). Nevertheless, other soil orders such as Regosols, Umbrisols and Histosols can be present (ISSS Working Group RB, 1998).

The name Andosols, term used by the FAO World Reference Base (WRB) classification (IUSS Working Group, 2015), also known as Andisols in the U.S. Soil Taxonomy (Soil Survey Staff, 1999), originates from the Japanese word *anshokudo* and *ando*, respectively meaning “dark coloured soil” and “dark soil”. This dark colour is due to the tendency shown by these soils to

accumulate large amount of OM (Delmelle et al., 2015; ISSS Working Group RB, 1998). They cover a small Earth land surface (it is estimated to be slightly less than 1 %) (Delmelle et al., 2015), but support 10 % of the world's population (Neall, 2009).

Figure 4 shows the different types of Andosols, divided according to their content in Al and Fe-oxides, phosphate retention and ratio of Al organic complexes to Al-oxides. The alu-andic type, which is rich in Al organic complexes, corresponds to the non-allophanic Andosols (Takahashi and Shoji, 2002). Andosols are generally divided into two categories: allophanic Andosols and non-allophanic Andosols, depending on the mineral composition of the A horizons. Allophanic Andosols are dominated by allophanes and imogolite, whereas non-allophanic Andosols are enriched in Al-humus complexes and 2:1 layer silicates (Shoji, 1985).

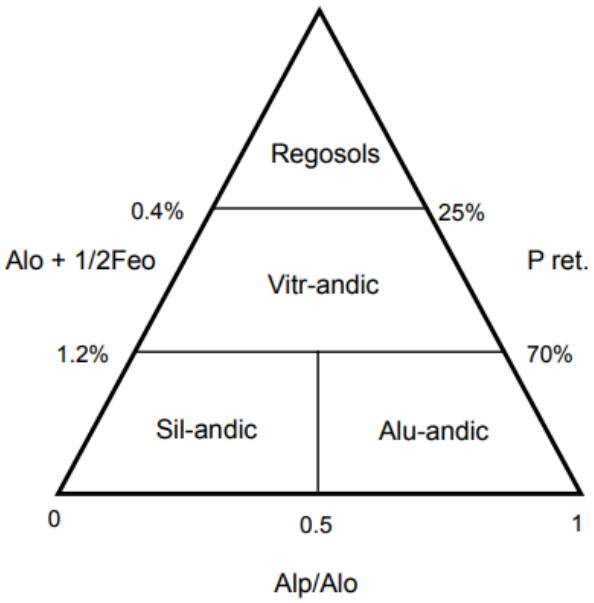

Figure 4. Generalised relationship between Regosols and the three subtypes of andic horizons in WRB classification ***(Shoji et al., 1996)****. Andic horizons is divided in two major types: the sil-andic type in which allophanes are dominant, and alu-andic type, which is mostly comprised of Al complexed by OM. The latter corresponds to the so-called non-allophanic Andosols* ***(Takahashi and Shoji, 2002)***

2.2.1. Parent material

Airborne pyroclastic materials[2] produced by volcanic eruptions are generically called tephra. The term volcanic ash refers more specifically to tephra with a size < 2 mm. Most volcanic soils developed from tephra (Shoji et al., 1993c) and are commonly called "volcanic ash soils" (Shoji et al., 1993a). Ash usually contains a high proportion of aluminosilicate glass, together with lesser primary crystalline minerals (Antos and Zobel, 2005). Ash-derived Andosols develop relatively rapidly under almost any types of climate, and thus are found in volcanic regions all around the world (Shoji et al., 1993b). In Ecuador the soil properties vary according to the

[2] Pyroclasts include close-to-source ballistics and scoria, tephra fallouts and deposits which relate to the explosive-fragmentation of magma during volcanic eruptions (Delmelle et al., 2015; Neall, 2009).

geographical location of the páramo. The northern Ecuador páramo soils on which our study focuses, are essentially non-allophanic Andosols developed on Holocenic volcanic ash deposits (Poulenard et al., 2001). In contrast, in the south of Ecuador, the soils are older (formed in the late Miocene and Pliocene (Buytaert et al., 2005)) and volcanic ash-free Histosols have developed ((Buytaert et al., 2005) from Buytaert, 2004).

Depending on the total silica content, volcanic rocks (and thus, also the ash materials) are classified as basalt (43 – 53.5 % SiO_2), basaltic andesite (53.5 – 58 %), andesite (58 – 62 %), dacite (62 – 70 %) and rhyolite (70 – 100 % SiO_2) (Shoji et al., 1975). Volcanic glass, a silica-based glass, is present in variable proportions in all volcanic parent materials. It is an amorphous solid made of a disordered arrangement of silicate oxides, in presence of different proportions of aluminum and other elements (Delmelle et al., 2015; Neall, 2009).

2.2.2. Physicochemical properties

Volcanic soil properties are strongly influenced by the parent material, degree of weathering, secondary mineral assemblage precipitating and accumulation of OM (Shoji et al., 1993c). Both allophanic and non-allophanic Andosols have the capacity to accumulate OM. The typical content of organic carbon of these two soil types is 8 - 12 % and up to 25 %, respectively (Shoji et al., 1993c). Through the formation of organic-mineral complexes, Andosols stabilise and physically protect the OM against microbial decomposition (Farley et al., 2004). This organic carbon storage capacity is also a consequence of an intermittent covering of the soil with fresh tephra. This layer of new tephra reduces soil aeration and isolates the carbon from soil fauna (Delmelle et al., 2015). Andosols usually have a low bulk density (< 0.9 g/cm³). This is a consequence of their high organic content, high porosity and the aggregation of soil materials (Delmelle et al., 2015). Such characteristics makes this type of soil an outstanding medium for the development of plant roots (Neall, 2009). The high porosity is also responsible for the high water-holding capacity. Moreover, OM enhances the productivity of Andosols by supplying nutrients and retaining plant-available water (Shoji et al., 1993c).

Additionally, Andosols often contain secondary components that develop very large surface areas (i.e. > 300 m²/g) (Shoji et al., 1993c) that carries a pH-dependent electrical charge. Above a certain pH value, some secondary minerals surfaces are mostly negatively charged, whereas below this value a positive charge will increasingly develop. Organic matter is also electrically charged, but is negative across a broad range of pH values. The variable surface charge of Andosols obviously impacts the transport of dissolved ions, including nutrients. Generally, at elevated pH values (i.e. a large negative charge), Andosols have a higher tendency to retain cations (Delmelle et al., 2015).

2.2.3. Pedogenesis

The weathering of an ash deposit over time leads to the formation of a volcanic soil. Soil formation is influenced by the nature of the parent material but also by the action through time

of other factors, including topography, vegetation (and to a lesser extent fauna) and climate. The formation of an Andosol results from a particular type of pedogenesis called “andolisation” (Shoji et al., 1993c).

The presence of alumino-silicate glass in the parent material is a critical component determining the trajectory of soil pedogenesis (Delmelle et al., 2015). Glass is the most abundant component in ash (Shoji et al., 1993b) and is amongst the primary solid phase, the least resistant to chemical weathering (due to its amorphous nature) (Shoji et al., 1993c). The weathering of ash releases mostly Si, Al and Fe. This results in the soil solution becoming oversaturated with respect to several secondary solid phases, which will eventually be able to precipitate (Delmelle et al., 2015; Ugolini and Dahlgren, 2002).

Many properties of the aluminosilicate glass influence its resistance to chemical weathering. In general, the rate of dissolution is inversely correlated with the silica content (Delmelle et al., 2015; Neall, 2009). In addition, the grain size and porosity of the ash also influences the kinetics of dissolution (and thus, of soil weathering); smaller particles are highly vesicular materials which develop larger reactive surface areas accessible for chemical reactions. The weathering rate is further influenced by the soil environment factors, such as soil temperature, amount of water percolating, pH, complexing ligand concentrations in soil solution and thickness of the ash that is weathered (Shoji et al., 1993c).

The formation of allophanic or non-allophanic Andosols seems to be controlled by the availability of Al^{3+} in solution (Ugolini and Dahlgren, 2002). The formation of allophanic Andosols is promoted in environments with pH values higher than 5. In such conditions, the concentration of complexing organic compounds is low and the inorganic Al species’ solubility is low. Thereby, Al released by weathering can react with Si to precipitate allophanes and/or imogolite (Ugolini and Dahlgren, 1991). Non-allophanic Andosols formation is favoured at pH values lower than 5, and in an environment rich in OM. Under these conditions, OM efficiently competes with aluminosilicates to form stable Al-OM complexes, and thus less Al is available in solution to coprecipitate with Si to form secondary aluminosilicates minerals (Delmelle et al., 2015)

With increasing soil age and weathering degree, Andosols often alter to other soil orders. This is nonetheless not true when new material (from repeated volcanic ash deposition) is added frequently to the soil. In this case, Andosols can be preserved in pretty stable conditions (Dahlgren et al., 2004). It is noteworthy that the physico-chemical properties of Andosols are favourable to plant growth, thereby enabling vegetation to quickly colonize ash deposits, thereby promoting soil formation (Shoji et al., 1993b).

2.2.4. Mineralogy

Primary mineralogy

In fresh ash materials, the most abundant primary magmatic solid phases are volcanic glass, plagioclase, quartz, pyroxenes, opaque minerals, hornblende, biotite and olivine. Figure 5 summarises the relative abundance of primary solid phases in magmatic rocks, as a function of chemical composition, i.e. silica content. The most abundant component is volcanic glass (Shoji et al., 1993b). Several authors have demonstrated that the relative stability of primary minerals towards weathering in volcanic ejecta, follows the following sequence: volcanic glass ≈ olivine < plagioclase < augite < hyperthene < hornblende < ferromagnetic minerals (Dahlgren et al., 2004).

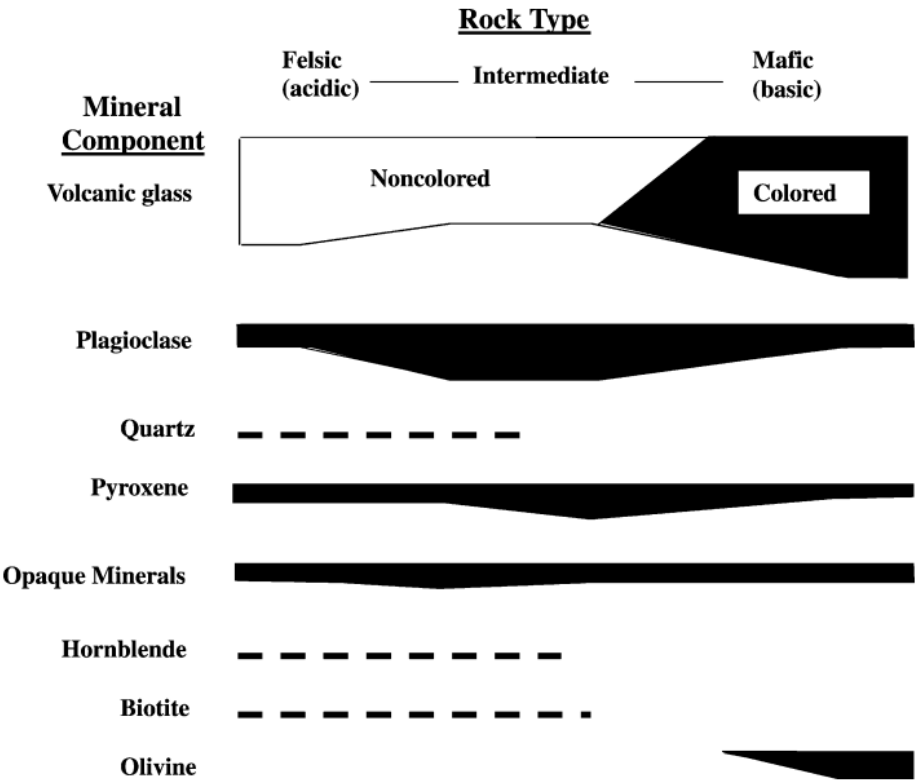

Figure 5. Relationship between rock types of tephritic materials and their mineralogy (Shoji et al., 1993c)

Secondary mineralogy

Due to rapid weathering of the glass-rich volcanic parent material, non-crystalline and poorly crystalline materials dominate the secondary alteration assemblage in volcanic soils. Thus, allophanes, imogolite and ferrihydrite are commonly found in these soils (Neall, 2009; Shoji et al., 1993c). Opaline silica may also occur (Shoji et al., 1993c; Ugolini and Dahlgren, 2002). Over time, crystalline minerals replace the metastable non-crystalline precursors. However, due to the small difference in free energy between them, this process is very slow (Dahlgren et al., 2004).

Many volcanic ash soils have allophanes and halloysite as dominant secondary solid phases (Zehetner et al., 2003). What dictates which secondary phase precipitates (Figure 6) is the leaching conditions, thus the infiltrating water amount. Under intense leaching, the dissolved Si concentration is relatively low. This favours allophanes formation and to a lesser extent imogolite formation (Delmelle et al., 2015). Allophanes ($Al_2O_3.SiO_2.nH_2O$) and imogolite ($SiAl_2O_5.2H_2O$) are aluminosilicates of poor crystallinity (Neall, 2009; Parfitt, 2009). The allophanes have a globular structure, and their Al:Si ratio can vary between 2:1 to 1:1 according to the composition of the soil solution from which they precipitate (Delmelle et al., 2015). Imogolite has a tubular structure (Parfitt, 2009) and is often in association with allophane, but in comparatively smaller quantities (Delmelle et al., 2015; Parfitt, 2009).

In humid climates where leaching is very strong and little Si is left during weathering, gibbsite ($Al(OH)_3$) forms instead of allophanes and imogolite. On the contrary, in dry climate, leaching is limited and Si concentration in solution is high. In this case, halloysite ($Al_2Si_2O_5(OH)_4$) is stable and can precipitate. It is thought that halloysite can form in volcanic soils in two distinct ways. On one hand, as this mineral generally forms in older ash deposits, it could be a result of allophanes weathering. For this to happen, the Si activity in the soil solution should be high, and thus is more likely to occur in rhyolitic tephras than in andesitic and basaltic tephras (Dahlgren et al., 2004). On the other hand, halloysite can form directly from volcanic ash weathering, but again if the Si activity in soil solution is high enough (Parfitt and Wilson, 1985). As Si activity in the soil solution is dictated by climate, drainage, tephra composition and vegetation, various proportions of allophanes and halloysite can be encountered in volcanic-ash soils. Usually, in Andosols, allophanes predominate (Parfitt, 2009)

As already mentioned, in an environment rich in OM and at pH ≤ 5, the availability of free Al in solution (Al^{3+}) becomes limited and the formation of secondary alumino-silicates is partially or totally impeded. It is well known that OM has a large capacity to form complexes with Al, thereby decreasing the concentration of dissolved Al^{3+} but overall increasing the solubility of Al (Parfitt, 2009). Less Al is then available to coprecipitate with Si, and as consequence, less aluminosilicate materials can form. This explains why, generally, the soil A horizon, which is continuously replenished with decomposing OM, contains less allophanes than the subsoil. This preferential complexation of Al with OM, instead of allophane/imogolite formation, is called the "*anti-allophanic effect*" (Shoji et al., 1993c).

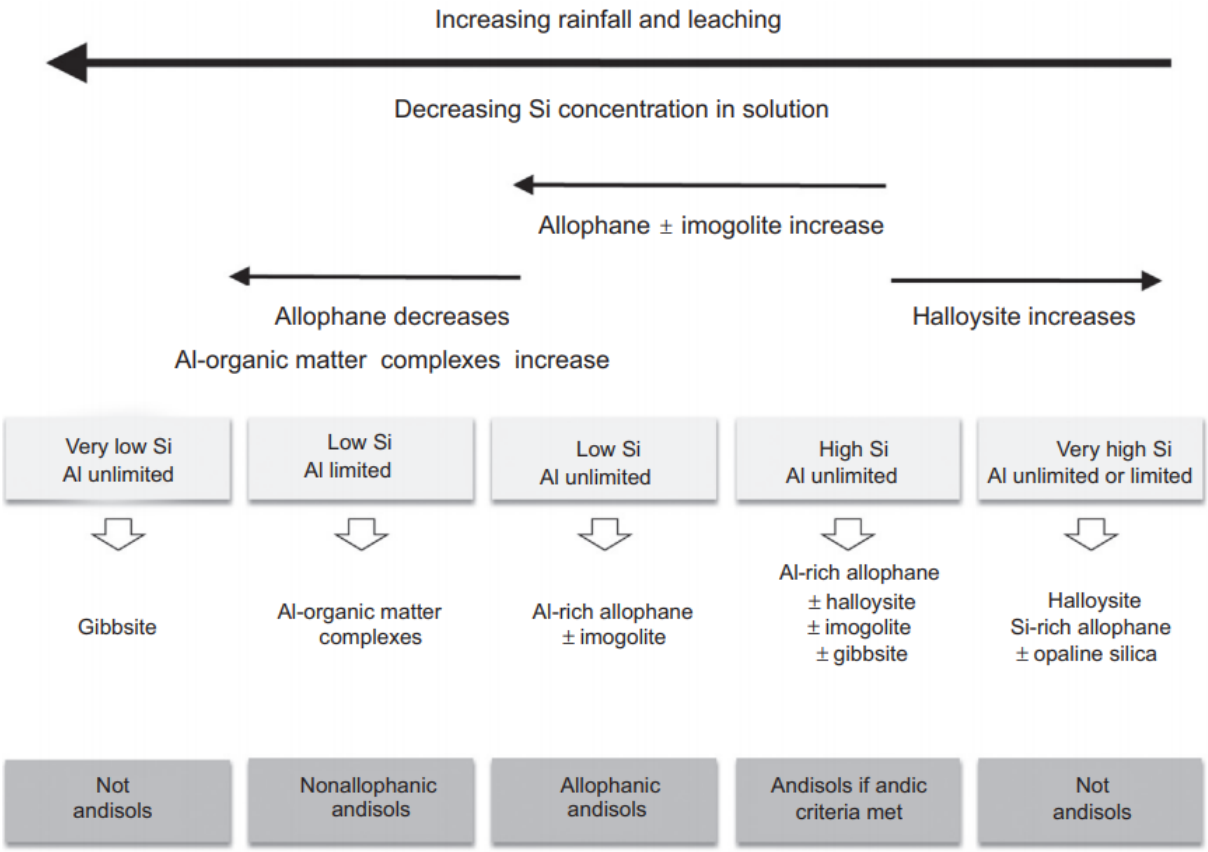

Figure 6. Simplified representation of the conditions under which different types of soil form as a result of volcanic weathering tephra. The influence of the leaching conditions of Al and Si on the secondary mineralogy is also indicated. The sign ± means that the mineral could also be present ***(Delmelle et al., 2015)***

As already mentioned, Fe is also easily released by volcanic material weathering. The main source of this element are mafic primary minerals such as pyroxenes, amphiboles, biotite and olivine, but it is also contained in volcanic glass. When in solution, Fe rapidly precipitates as ferrihydrite, a ferric iron oxyhydroxide ($Fe_5(OH)_8.4H_2O$) (Delmelle et al., 2015). Nonetheless, like imogolite, ferrihydrite content in volcanic ash soils is typically substantially lower than allophanes content (Parfitt and Wilson, 1985). Ferrihydrite precipitation is also prevented by the "anti-hematitic" effect of soil OM, which is the preferential incorporation of Fe into OM-complexes (Schwertmann, 1958).

2.3. Reactive transport modelling

2.3.1. Concept

Reactive transport modelling (RTM) designates the description – using mathematics – of the chemical and biochemical reactions that occur as an aqueous solution percolates downward through a solid porous material, for example a soil. The model once transposed on a computer allow to efficiently perform simulations with different input data and parameters. Reactive transport models have been applied to understand biogeochemical systems for more than four decades (Agrawal et al., 2017; Chapman, 1982; Moore et al., 2012). RTM has developed

noticeably in the 1990s, and many widely used RTM codes have surfaced, such as Hydrogeochem (Yeh and Tripathi, 1991), Phreeqc (Parkhurst and Appelo, 1999), and Crunchflow (Steefel and Lasaga, 1994). Reactive transport modelling is a powerful method to test with computers the effects of multiple space (from pore scale to field scale) and time scales in the Earth (Steefel et al., 2005). Hence, it enables to study the natural dynamics of Earth's systems and the human impacts on those systems. For example, it has been applied in geological carbon sequestration (Brunet et al., 2013; Xu et al., 2011), nuclear waste disposal (Saunders and Toran, 1995; Wilson et al., 2018), and environmental bioremediation (Bao et al., 2014; Fang et al., 2009). The foremost progress of modern RTMs is the coupling of flow and transport within a complete geochemical thermodynamic and kinetic framework (Steefel et al., 2015).

The most widespread application of the RTMs is the description of the subsurface (Figure 7), which enables the testing of the related processes and a deeper our knowledge on these subsurfaces. This is possible thanks to the comparison between the computational results and the data obtained from real-world measurement (Maher and Mayer, 2019a). To create an RTM from a conceptual world, the interacting geochemical processes that are assumed to be at work must be described quantitatively. It is also essential to define the initial and boundary conditions. For example, mineral distributions, their surface areas and hydraulic conductivity, could be included in the initial conditions (Maher and Mayer, 2019a).

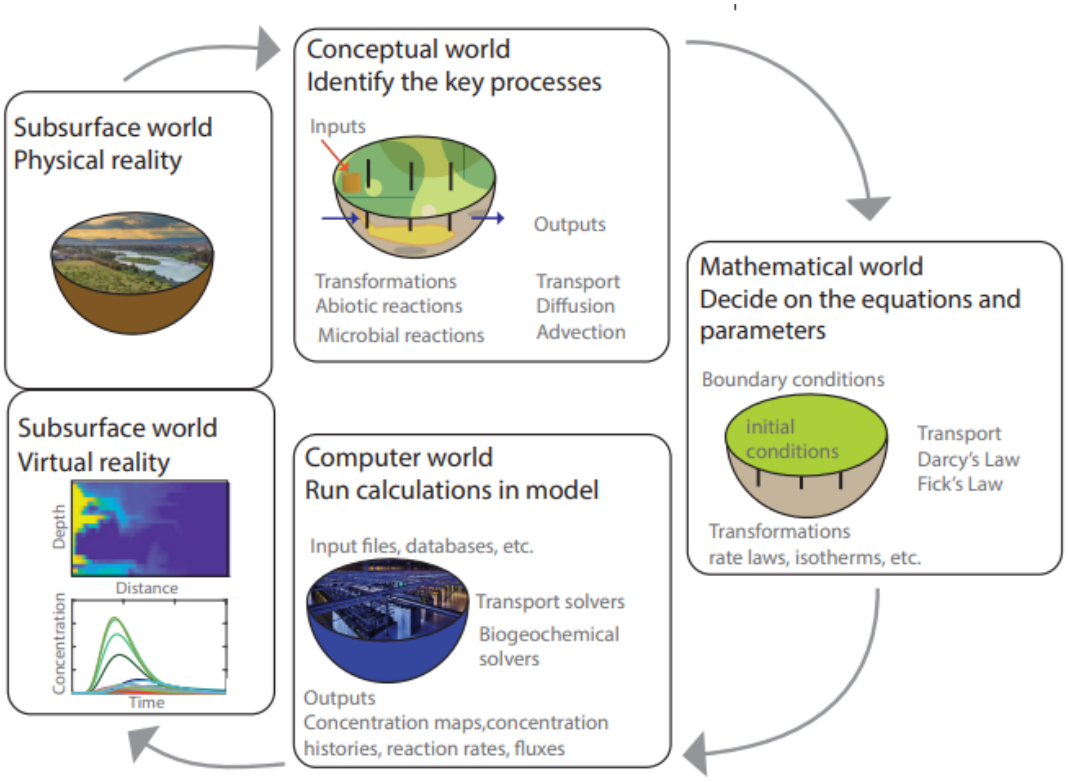

Figure 7. Iterative process of model building. It starts with the subsurface being transformed into a conceptual model. Then, this model is converted into mathematical formulations, which the computer model will read. The results obtained by the computer model and the data obtained from the physical world will be compared iteratively and will drive to new conceptual models (Maher and Mayer, 2019a).

2.3.2. General approach (thermodynamics and kinetics)

A wide range of minerals with very different dissolution/precipitation kinetics and thermodynamics properties are found in the Earth's subsurface. Aqueous solutions, gases and microorganisms interact with the surface of these minerals. To simulate the subsurface and to quantify the dynamics of systems, mass balance equations are used (Maher and Mayer, 2019b). RTMs enable computers to trace the evolution of several geochemical species in solution and in solid phase, by solving partial differential equations that couple flow and transport, within a complete geochemical kinetic and thermodynamic framework (Steefel et al., 2015).

RTMs divide the studied media into several cells (Figure 8) and each cell is considered as a "well-mixed flow reactor" (WMFR). An aqueous solution with reactant and products flows through each cell. To determine what fluxes of aqueous solution and elements flow into and out of the cells, a mass balance description is required. Generally, Darcy's law is used to describe water flows in aquifers. To completely describe the mass fluxes, dispersivity and/or diffusion of the dissolved species needs to be defined (Maher and Mayer, 2019b).

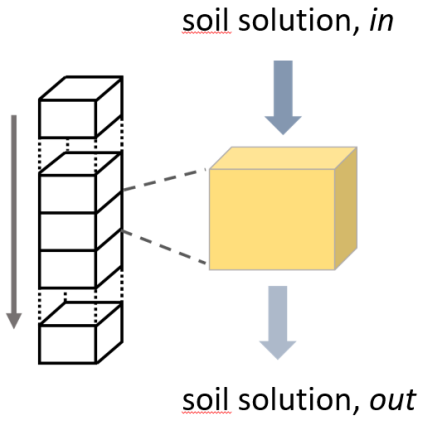

Figure 8. Conceptualisation of reactive transport. Each cell is considered as a well-mixed flow reactor, and the soil solution that gets in reacts and gets out with another composition.

Reactions are governed by thermodynamics and kinetics. The stoichiometric relations of the reactants and products are subject to thermodynamic constraints. Many different databases are available, and contain the reactions in which the reactants and products are involved, as well as the equilibrium constants. The use of these databases and geochemical speciation calculations enable to ascertain species distribution in aqueous solution (Maher and Mayer, 2019b; Mayer et al., 2002). In addition to the thermodynamics constraints, the reaction rate (i.e. the kinetics) also often limits reactions. In order to correctly describe reaction evolution and geochemical advancement, varied rate expressions and associated rate coefficients must be integrated in the reactive transport model. The majority of the kinetic data originates from experimental studies (Maher and Mayer, 2019b).

The reactions commonly included into the reaction network are (1) mineral dissolution-precipitation reactions, (2) microbially mediated oxidation-reduction reactions, (3) surface

complexation reactions, (4) ion exchange reactions, (5) homogeneous reactions within the aqueous phase and (6) gas-aqueous phase exchange. The first two types of reactions are often kinetically limited, while the four others are more frequently described as equilibrium processes (Mayer et al., 2002; Steefel et al., 2015).

3. Methods: Reactive Transport Modelling

Based on the literature review regarding the capabilities of the RTM for geochemical modelling, we select RTM for this study of the páramos. The modelling study was performed using CrunchFlow, a software package[3] for simulating multicomponent reactive transport modelling developed in the 1990s by Steefel et al. (2015). This tool is chosen because it has successfully been used in the past to model water-rock interactions and chemical weathering. Crunchflow has been applied to many problems in Earth and environmental sciences (Steefel et al., 2015) including carbon sequestration (Zhang et al., 2015), chemical weathering (Perez-Fodich and Derry, 2019) and reactive contaminant transport (Wanner et al., 2012).

The modelling approach bears a close resemblance to that described in the work of Perez-Fodich and Derry (2019), who studied the chemical weathering of a basaltic rock (lava flow) in Hawaii. Here we consider a one-dimension 1-m long porous media column (i.e. an ash deposit) with a dacitic composition. The column reacts with rainwater of known composition in an advection-dominated transport regime.

The model is created iteratively, comparing successively with more measured data (Table 1):

(1) M1 - a basic model at equilibrium with atmospheric CO_2 concentration and using three degrees of soil water saturation;
(2) M2 - the basic model in which CO_2 concentration is increased 10 and 100 times to represent the effect of soil respiration;
(3) M3 - the same model but in which low molecular weight organic acids (LMWOA) are added to the infiltrating solution at concentrations roughly corresponding to those measured in the field for soils under tussock-forming grasses (TU) and cushion-like plants (CU).

Computations are performed up to 5 kyr and when possible, the simulation results are compared to measurements from the field (i.e. a soil of 0.8 kyr in age). We then tested three different-from-today water infiltration rates (F1, F2, F3) in order to evaluate the potential effect of a climate change-induced alteration of rainfall in the Andes (Table 2).

[3] https://www.netl.doe.gov/sites/default/files/netl-file/CrunchFlow-Manual.pdf

Table 1. Summary of the modified parameters for the creation of the model.

	Model M1	Model M2a	Model M2b	Model M3TU	Model M3CU
Infiltrating aqueous solution composition	Rainfall (Table 6)	Rainfall (Table 6)		Rainfall (Table 6)	
CO_2 concentration (ppmv) – constant flux	300	3 000	30 000	30 000	
pH	5.9 (measured)	5.1 (Phreeqc)	4.6 (Phreeqc)	4.4 (Crunchflow)	3.3 (Crunchflow)
Organic acids (mol/L)	No	No		TU : 3.44 10^{-5}	CU : 5.25 10^{-4}
Soil water saturation (%)	30 – 50 – 70	50		50	
Infiltrating water flow (m/yr)	0.4	0.4		0.4	

Table 2. Summary of the modified parameters to study the impact of changing precipitation patterns.

	Model F1	Model F2	Model F3
Infiltrating aqueous solution composition	Rainfall (Table 6)		
CO_2 concentration (ppmv) – constant flux	30 000		
pH	4.4 under TU and 3.3 under CU		
Organic acids	TU & CU		
Soil water saturation (%)	50		
Infiltrating water flow (m/yr)	0.2	0.6	0.8

3.1. Model parameters

3.1.1. Mineralogy

Primary mineralogy

The mineral assemblage of the Antisana dacitic ash representing the parent material (i.e. Quilotoa dacitic ash deposit) that will undergo chemical weathering is comprised of plagioclase (24.1 wt%), amphibole (12.6 wt%), biotite (8.9 wt%), iron oxides (2.1 wt%) and rhyolitic volcanic glass (52.3 wt%) (Rosi et al., 2004). Due to their low proportions compared to the other solid phases, and in order to simplify the model, iron oxides were not considered in the model. The corresponding chemical formulas of the other solid phases are calculated from Rosi et al. (2004) and are given in Table 3. Unfortunately, the thermodynamic and kinetic details available in various databases do not necessary match the compositions of the plagioclases, amphiboles and volcanic glass reported by Rosi et al. (2004). A mechanical mixture of two minerals is used to represent the amphiboles (riebeckite and pargasite) and the biotite (phlogopite and annite). For representing the plagioclases, two choices are possible: a mechanical mixture of anorthite and albite or a solid solution with an average composition of 29 % anorthite and 71 % of albite, $PlagAn_{29}Ab_{71}$ (Stefánsson, 2001). We use here the solid solution because it is probably closer to reality than a mechanical mixture of two minerals. The corresponding thermodynamics and kinetics constants are added to the database in Crunchflow. Regarding the volcanic glass, as its thermodynamic and kinetic values are known, it is added to the database with the calculated chemical formula normalised to one Si atom.

Table 3. Calculated formula of the minerals present in the Andean páramo parent material (800-year-B.P. Quilotoa volcano's ash deposits) with the corresponding minerals used to represent them in the model (theoretical formulas)

Mineral	Calculated formulas	Theoretical formulas
Plagioclase	$Si_{2.01}AlFe(II)_{0.01}Ca_{0.23}Na_{0.49}K_{0.01}$	Anorthite: $Ca(Al_2Si_2)O_8$ & Albite: $NaAlSi_3O_8$ OR $PlagAn_{29}Ab_{71}$: $0.4(Ca(Al_2Si_2)O_8) + 0.6(NaAlSi_3O_8)$
Amphibole	$Na_{0.34}Ca_{1.62}Mg_{3.6}Si_{7.6}Al_{1.21}Fe_{1.57}K_{0.04}$	Riebeckite: $Na_2(Fe_3Fe_2)Si_8O_{22}(OH)_2$ & Pargasite: $Na(Ca_2Mg_4Al)(Al_2Si_6)O_{22}(OH)_2$
Biotite	$K_{0.67}Fe_{0.81}AlSi_{2.31}Mg_{1.35}Ca_{0.006}Na_{0.06}$	Phlogopite: $KMg_3(AlSi_3)O_{10}(OH)_2$ & Annite: $KFe_3(AlSi_3)O_{10}(OH)_2$
Volcanic glass	$SiAl_{0.23}Fe(II)_{0.01Mg0.01}Ca_{0.02}Na_{0.11}K_{0.05}O_{2.47}$	

Secondary mineralogy

In the model, two aluminosilicates – allophanes and halloysite –, amorphous silica and gibbsite are allowed to precipitate as secondary minerals (Table 4). The presence of allophanes and

halloysite has been reported in the volcanic ash soils of the Andean valley of northern Ecuador (Zehetner et al., 2003). Amorphous silica and gibbsite are also known to precipitate in volcanic soils (Delmelle et al., 2015). The precipitation of iron-containing secondary minerals (e.g. goethite) is not considered since the content of iron in the parent material is very low (100 times less Fe^{2+} than Si).

Table 4. Secondary minerals that are included into the model and their corresponding chemical formula.

Minerals	Chemical formula
Allophane	$Al_2O_3(SiO_2)_{1.22}(H_2O)_{2.5}$
Halloysite	$Al_2Si_2O_5(OH)_4$
Amorphous silica	$SiO_{2(am)}$
Gibbsite	$Al(OH)_3$

3.1.2. Thermodynamic properties

To be applied successfully, RTMs must use consistent thermodynamic data for the selected minerals. This is a major difficulty as there are many thermodynamic data compilations and it is often difficult to ascertain the original source of the data (Wolery and Jové Colón, 2017). In this study, LLNL is used as the main database, which is based on the EQ3/6 geochemical modelling package and contains thermodynamic equilibrium constants for aqueous, gas and mineral species (Wolery, 1992). The solubility constants (log K) values used here and their sources are listed in Table 5.

For volcanic glass, the solubility constant is calculated using Equation 1, which considers the glass to be a mixture of various oxides (Paul, 1977):

$$log(K)_{glass} = \sum_i \log(K_i) + \sum_i x_i \, log \, x_i \qquad (1)$$

Where x_i and K_i are the molar fraction and the solubility product of the glass constituting oxides. The log K_i values and the dissolution reactions used to calculate the log K of the glass at 25 °C are shown in Table A. 1.

3.1.3. Kinetics of dissolution - precipitation reactions

For calculating the dissolution and precipitation of crystalline and amorphous solids, Crunchflow uses rate laws that are based on the Transition State Theory (TST) detailed by Lasaga (1984). The expression of the rate law takes the form of Equation 2 and 3. The TST links the kinetic rates of geochemical processes and the thermodynamic driving force (Yang and Steefel, 2008).

$$r = A_m k_m \, exp\left[\frac{-E_a}{RT}\right] \Pi a_i^n [1 - exp(m_2 g)] \qquad (2)$$

$$g \equiv \frac{\Delta G}{RT} = ln\left[\frac{Q}{K_{eq}}\right] \quad (3)$$

where r is the reaction rate (mol m^{-2} s^{-1}), A_m is the mineral surface area (m^2 m^{-3} porous media), k_m is the rate constant of the reaction (mol m^{-2} s^{-1}), E_a is the activation energy (kcal $mole^{-1}$), Q is the ion activity product for mineral-water reaction, K_{eq} is the corresponding equilibrium constant, and Πa_i^n is a product representing the inhibition or catalysis of the reaction by various ions in solution raised to the power *n* (Steefel, 2009). ΔG is Gibbs free energy of the reaction, R is the molar gas constant and T is the temperature (K). g is the rate dependence on reaction affinity (explained later in this section) and m_2 is the so-called Temkin average stoichiometric number (Lasaga, 1984).

The volcanic glass rate law r_{volca} is adapted in Crunchflow based on the study of Declercq et al. (2013) which accounts for the inhibitory effect of free Al^{3+} and the promoting effect of H^+ activity on the dissolution of rhyolitic glass (Equation 4).

$$r_{volca} = A_m k_m \, exp\left[\frac{-E_a}{RT}\right] \frac{a_{H^+}^{0.27}}{a_{Al^{3+}}^{0.09}} [1 - exp(m_2 g)] \quad (4)$$

Where $a_{H^+}^{n_1}$ and $a_{Al^{3+}}^{n_2}$ are H^+ and Al^{3+} activities.

Chemical affinity is responsible for the glass dissolution kinetics slowing down with time. When the glass dissolves, it releases some chemical elements in solution that can become saturated with respect to silica. Under saturated conditions, silica may precipitate into a gel, which is an amorphous layer of a solid phase that forms on the surface of the glass (Cailleteau et al., 2008). Several studies suggest $SiO_{2(am)}$ to be the gel forming on the glass (Feng, 1993; Ma et al., 2017; Wolff-Boenisch et al., 2004). The silica gel constitutes a diffusion barrier and thus slows down dissolution of the glass. It seems that this chemical affinity phenomenon occurs with silicate minerals in general (Cailleteau et al., 2008).

Two difficulties arise regarding the definition of the affinity term. Firstly, the affinity *g* should be based on the equilibrium constant for the dissolution reaction of amorphous silica (K_{SiO2}) at the dissolving glass surface (Gin et al., 2016), yet Crunchflow only allows it to be based on the equilibrium constant of the solid phase dissolving, i.e. the glass. Secondly, no value of the Temkin coefficient m_2 (in Equation 4) for volcanic glass could be found in the scientific literature. Therefore, we use m_2 = 1, which has been suggested to us by Prof. J. Schott (University of Toulouse, GET) on the basis of the stoichiometry of the glass dissolution reaction, i.e. one mole of volcanic glass dissolved leads to the formation of one mole of $SiO_{2(am)}$. In theory, the effect of the affinity term on the dissolution rate of a mineral becomes significant when the solution approaches saturation with respect to the secondary solid phase thought to impede dissolution (Ma et al., 2017).

The kinetic constants of all minerals, listed in Table 5, mainly originate from published values in Palandri and Kharaka (2004). These authors have tabulated a wide range of kinetic values for andesine. Here we use the dissolution rate corresponding to a mineral with composition $PlagAn_{29}Ab_{71}$. For pargasite, the same dissolution rate as for riebeckite is used. Regarding the rhyolitic glass, its dissolution rate is calculated based on Declercq et al. (2013). Precipitation kinetics for allophanes has not been reported in the literature and we assume that it can be represented by the rate laws documented for $SiO_{2(am)}$. A similar approach was adopted by Perez-Fodich and Derry (2019).

The specific surface areas (SSA) of the different solid phases are not known. Therefore, similar to Perez-Fodich and Derry (2019)'s approach, we use here typical values (SSA between 0.1 m^2/g to 1 m^2/g for primary solid phases, and SSA ranging up to 10 m^2/g for secondary solid phases). As we will witness that the use in the simulations of documented secondary mineral SSA values results in numerical instabilities, the SSAs are lowered by several orders of magnitude. This can be offset by increasing the rate of precipitation of secondary minerals because modifying the SSA has the same effect as modifying the rate constant of dissolution-precipitation, as rate laws depend linearly on both terms (Equation 2). Treating the SSA as the fitting factor instead of the rate is frequently done in reactive transport modelling (Heidari et al., 2017; Moore et al., 2012; Navarre-Sitchler et al., 2011). Moreover, it is commonly observed that laboratory rates largely exceed the ones observed in the field (Dontsova et al., 2009; Moore et al., 2012; White et al., 1996). In theory, the ratio of allophanes' SSA to glass' SSA could be > 500 and thus, we increase the allophanes rate constant (log k) in the model by a factor of 50. The log k of halloysite rate is also increased five times. Normally, the log k of gibbsite should also be increased as its SSA is above 1, but we will identify a mineral precipitation overestimation and thus its initial log k is kept.

Table 5. Dissolution reaction, initial abundance (in %v), SSA, thermodynamic constants and dissolution-precipitation kinetic constants of the minerals included in the model.

Mineral	Dissolution reaction stoichiometry	Vol (%)	SSA ($m^2\ g^{-1}$)	log $K_{m,eq}$ (25 °C)	log k_m (mol $m^3\ s^{-1}$)
$PlagAn_{29}Ab_{71}$	$0.4(Ca(Al_2Si_2)O_8) + 0.6(NaAlSi_3O_8) + 5.6H^+ \rightarrow 0.6Na^+ + 0.4Ca^{2+} + 1.4Al^{3+} + 2.6SiO_2 + 2.8H_2O$	8.2	0.1	-20.11[4]	-12.70[5]
Riebeckite	$Na_2(Fe_3Fe_2)Si_9O_{22}(OH)_2 + 14H^+ \rightarrow 3Fe^{2+} + 2Fe^{3+} + 2Na^+ + 8SiO2 + 8H_2O$	1.7	0.1	11.62[6]	-12.20[7]
Pargasite	$Na(Ca_2Mg_4Al)(Al_2Si_6)O_{22}(OH)2 + 22H^+ \rightarrow 3Al^{3+} + 2Ca^{2+} + 4Mg^{2+} + Na^+ + 22H_2O$	1.9	0.1	97.836[8]	-12.20[5]
Annite	$KFe_3(AlSi_3)O_{10}(OH)_2 + 10H^+ \rightarrow K^+ + 3Fe^{2+} + 3(SiO_2) + 6H_2O$	1.2	0.1	29.47[9]	-11.63[10]
Phlogopite	$KMg_3(AlSi_3)O_{10}(OH)_2 + 10H^+ \rightarrow K^+ + 3Mg^{2+} + 3(SiO_2) + 6H_2O$	1.5	0.1	37.44[9]	-12.40[5]
Volcanic glass	$SiAl_{0.23}Fe(II)_{0.01}Mg_{0.01}Ca_{0.02}Na_{0.11}K_{0.05}O_{2.47} + 0.934H^+ \rightarrow SiO_2 + 0.233Al^{3+} + 0.01 Fe^{2+} + 0.012Mg^{2+} + 0.019Ca^{2+} + 0.107Na^+ + 0.046K^+ + 2.468H_2O$	26.8	0.1	4.53[11]	-11.25[12]
Allophane	$Al_2O_3(SiO_2)_{1.22}(H_2O)_{2.5} + 6H^+ \rightarrow 2Al^{3+} + 1.22SiO_{2(aq)} + 5H_2O$	-	1	10.96[13]	-12.23[5]
Halloysite	$Al_2Si_2O_5(OH)_4 + 6H+ \rightarrow 2Al^{3+} + 2SiO_2 + 5H_2O$	-	1	10.32[6]	-12.89[14]
$SiO_{2(am)}$	$SiO_{2(am)} \rightarrow SiO_{2(aq)}$	-	1	-2.70[8]	-12.23[5]
Gibbsite	$Al(OH)_3 + 3H^+ \rightarrow Al^{3+} + 3H_2O$	-	1	7.76[9]	-11.50[5]

[4] Adjusted from (Stefánsson, 2001)
[5] (Palandri and Kharaka, 2004)
[6] Adjusted from Thermoddem (Blanc et al., 2012)
[7] Sverdrup 1990 in (Palandri and Kharaka, 2004)
[8] SUPRCRTBL (Zimmer et al., 2016)
[9] EQ3/6 (Wolery, 1992)
[10] Thermoddem (Blanc et al., 2012)
[11] Calculated from (Paul, 1977)
[12] Calculated from (Aradóttir et al., 2012)
[13] (Stefánsson and Gíslason, 2001)
[14] Default value of Crunchflow

3.1.4. Aqueous chemistry

For all the simulations (M1, M2 and M3), the same infiltrating rainwater composition and flow are used, but the CO_2 concentration and organic acid concentration varied (Table 1). Table 6 shows the chemical composition of the infiltrating rainwater. The CO_2 concentration in the rainfall water is initially fixed by considering equilibrium with the partial pressure of CO_2 in the atmosphere, i.e. 300 ppmv. Then, in order to account for the rise in CO_2 concentration due to soil respiration (microbial decomposition of OM), the model is run with a CO_2 concentration increased 10 (3000 ppmv) and 100 (30 000 ppmv) times. Molecular O_2 in the rainwater is in equilibrium with the partial pressure of O_2 in the atmosphere (i.e. 20 %). Regarding the initial conditions of the soil profile, the rainwater composition is used but the pH is set to 7.

Table 6. Rainfall chemistry for the Antisana region. It is used as the boundary condition of the model M1. The pH value of the solution is calculated with Phreeqc.

Species	Concentration (mol L^{-1})
pH	5.62
Ca^{2+}	1.7×10^{-5}
Mg^{2+}	4.6×10^{-6}
Fe^{2+}	6.3×10^{-8}
Fe^{3+}	6.3×10^{-8}
Na^{+}	4.9×10^{-6}
K^{+}	1.1×10^{-5}
Al^{3+}	1.0×10^{-8}
$SiO_{2(aq)}$	3.8×10^{-6}
Cl^{-}	2.0×10^{-6}
NO_3^{-}	2.3×10^{-5}
SO_4^{2-}	3.2×10^{-6}

3.1.5. Organic ligands

Low molecular weight organic acids (LMWOA) need to be considered in the model since they easily bind to mineral surfaces and are important dissolving agents. Moreover, the mobility of metal cations in solution is increased in presence of LMWOA as they can complex together. LMWOA are produced by the soil biota and enter the soil mainly through the microbial decomposition of OM and rhizodeposition (Renella et al., 2004).

Oxalic acid is included as LMWOA in our simulations as its ability to complex with Al and Fe is well documented (van Hees and Lundström, 2000). Another reason for the use of this LMWOA is that we have access to its kinetic and thermodynamic data (Morrey et al., 1985; Perez-Fodich and Derry, 2019). In the present work, only Al and Fe(II) are allowed to complex with oxalic acid. The thermodynamic data for these complexation reactions are borrowed from the Minteq

database (Morrey et al., 1985), as recommended by Perez-Fodich and Derry (2019). The corresponding values, listed in Table A. 2, were added to the model's database.

Two concentrations of oxalic acid are tested to represent the tussock grasses and cushion plants that cover the páramo soil. Under tussock grasses a measured dissolved organic carbon (DOC) concentration value of 3.44 10^{-5} mol/L is used, whereas for soil under cushion plants 5.25 10^{-4} mol/L is included in the model. The decomposability of the oxalic acid is voluntarily omitted from the model because adding it in an intermediate test did not give significantly different results and it is desired to keep the model as simple as possible.

3.2. Model formulation

As already stated above, the simulations are geometrically one dimensional and are built on a 1 m fresh dacite ash column. This column is divided into 50 cells of 2 cm each and reacts with an aqueous solution of infiltrating rainwater composition and gases. The thickness of the Quilotoa ash deposit is approximately 30 cm. However, preliminary simulation tests with 30 cm gave numerical errors and thereby to avoid them, a thicker dacite ash column of 1 m is used in the model runs. The solution is transported by advection, whereas the gases by diffusion.

Regarding the time dimension, the model is run to simulate chemical weathering over 0.1 kyr (computational test point only), 0.8 kyr, 2 kyr and 5 kyr. The Antisana páramo developed on soils formed from the ash deposits emplaced by the eruption of Quilotoa volcano, 800 year-BP. The weathering soil profile obtained from the 0.8 kyr simulation should correspond to the present-day soil conditions. Thus, the simulation results are compared to the solution pH and chemical element concentrations measured in the field in recent years. This comparison allows us to adjust iteratively the model parameters in order to produce a set of results that match reasonably well the field observations. The simulation durations of 2 and 5 kyr correspond to the future and allow to depict the difference in the soil chemistry evolution; for example, when rainfall inputs are increased or decreased in relation to climate change.

The base of the soil profile is modelled by a flux boundary condition, whereas the top of the profile in contact with the atmosphere is modelled by a Dirichlet boundary condition. The temperature of the model is set to 13 °C which is the mean annual temperature in the studied area.

3.2.1. Transport

The solution of rainwater composition infiltration into the soil is vertical and modelled by 1-D Darcy flow. The rainwater infiltration fluxes are estimated by a mass balance between precipitation and evapotranspiration. In the studied area, mean annual precipitations are ~0.700 m/yr and evapotranspiration of ~0.300 m/yr (Paéz et al., 2021, in preparation). The calculated infiltration flux is ~0.4 m/yr. Given that the soil moisture measured in the Antisana soil is in the range of 30 to 70 % (M. Calispa, personal communications), simulations with soil

water saturation at 30, 50 and 70 % are run. The initial porosity of the profile is set to 50 %. This value corresponds to the typical porosity of a volcanic ash deposit (Biass et al., 2016).

3.2.2. Modified precipitation quantities

It is commonly known that weathering depends on climate (temperature and precipitation patterns) (Gislason et al., 2009). With the ongoing climate change, IPCC (2014) predicts an increase in temperature and precipitation. Nevertheless, these projections are highly uncertain. In this paper, increases by 1.5 and 2 times of the current precipitations are tested. A simulation with half the amount of the current infiltration quantity is also run to evaluate the potential impacts of a reduced rainfall or higher evapotranspiration linked to higher temperatures. The F models are slightly more complicated, as the current water flow rate (0.4 m/yr) is used for the first 0.8 kyr and then other rates are subsequently used.

3.3. Mass-transfer profiles calculation

Mass transfer coefficients (Equation 5) allow to calculate the mass gains or losses of an element due to weathering relatively to the mass of the element in the parent material (Anderson et al., 2002).

$$\tau_{j,w} = \frac{C_{j,w}C_{i,p}}{C_{j,p}C_{i,w}} - 1 \quad (5)$$

Where $\tau_{j,w}$ is the mass-transfer coefficient for the element j, $C_{j,w}$ and $C_{j,p}$ are the concentrations of j in the weathered and parent material respectively. $C_{Ti,w}$ and $C_{Ti,p}$ are the concentrations of an immobile component in the weathered and parent material, respectively. Titanium has been chosen here as the immobile element as its low mobility in soils is well-documented (Molina et al., 2019). When the $\tau_{j,w}$ value is positive, it signifies that there is an enrichment in the j element, while when it is negative, it indicates a loss.

It is important to bear in mind that the τ values are not known for our study site. Antisana is situated in an active volcanic zone. Thus, a nearby eruption could have added ash with different concentrations in immobile elements than those in the Quilotoa ash. The τ estimates are therefore used to verify the consistency of our results; they cannot be compared with field-derived values.

4. Results

This section presents the main results of the successive M1, M2, M3 (Table 1) and F1, F2 and F3 models (Table 2). We detail the computed time evolutions of the soil solution pH and dissolved free Al^{3+}, aqueous silica ($SiO_{2(aq)}$), sodium (Na^{+}), potassium (K^{+}), calcium (Ca^{2+}) and magnesium (Mg^{2+}) concentrations as well as the changes in the volume percentages of the key primary (plagioclases and volcanic glass) and secondary (allophanes, gibbsite, halloysite and $SiO_{2(am)}$) solid phase. The reason for selecting Na^{+}, K^{+}, Ca^{2+} and Mg^{2+} indicators is because they are essential nutriments for plants (Silber and Bar-Tal, 2008).

4.1. Base simulation (M1)

The soil solution pH increases with depth (Figure 9a). Through time, the pH decreases in the weathering profile but stays basic (pH > 7) across most of it. At 0.8 kyr, the pH is ∼7 at the surface of the profile and is buffered at ∼9 at 1 m. The M1 model overestimates the pH value by 2 units at 20 cm. After 2 kyr of weathering, the first 10 cm of the weathering profile reaches slightly acidic pH values, i.e. 6.5 < pH < 7.

The solution in the first 10 cm of the weathering profile has a low concentration of $SiO_{2(aq)}$ (< 10^{-3} mol/L) at all time (Figure 9b). In the 0.8 kyr simulation, the $SiO_{2(aq)}$ concentration increases with depth and reaches ∼3.5 10^{-3} mol/L at 1 m. After 5 kyr of weathering, the $SiO_{2(aq)}$ concentration has decreased and is ∼1 10^{-3} mol/L at 1 m depth. The model predicts an $SiO_{2(aq)}$ concentration that compares relatively well with what has been measured in the soil solution in the field.

The free Al^{3+} concentration in the weathering profile is very low (< 10^{-10} mol/L) at all times and all depths (Figure 9c). With depth (and thus, increasing pH), free Al^{3+} decreases, whereas with time, it increases. At 0.8 kyr, the free Al^{3+} concentration varies from ∼10^{-12} mol/L at the surface of the weathering profile to ∼10^{-19} mol/L at 1 m depth.

Regarding the cations Ca^{2+}, Mg^{2+}, Na^{+} and K^{+}, their concentrations increase with depth in the weathering profile (Figure 9d, e, f, g). The temporal evolutions differ between the cations. At 0.8 kyr, Ca^{2+} concentration increases linearly with depth up to 50 cm and then stabilises at ∼2.5 10^{-4} mol/L (Figure 9d). With time, Ca^{2+} increases more slowly (globally the profile is less concentrated in Ca^{2+}). After 5 kyr of weathering, at 1 m depth, only ∼10^{-4} mol/L of Ca^{2+} is in solution. The predicted concentrations of Ca^{2+} at 0.8 kyr are similar to the measured concentration of Ca^{2+} under CU. Magnesium follows a similar trend to that of Ca^{2+} (Figure 9e). At 0.8 kyr, it increases linearly during the first 70 cm, and then stabilises at ∼1.8 10^{-4} mol/L. The concentration predicted at 0.8 kyr is ∼5 10^{-5} mol/L lower than the field measurements corresponding to the soil solution at 20 cm depth. Sodium and K^{+} concentrations both increase with depth and decrease with time (Figure 9f, g). Potassium shows a linear increase in the whole profile and for all weathering durations. The predicted K^{+} concentration is closer to the

measurements under TU. The measured concentration of K^+ under CU is four times higher than the calculated value. M1's prediction of Na^+ concentration at 0.8 kyr conforms with the measured concentration in the field.

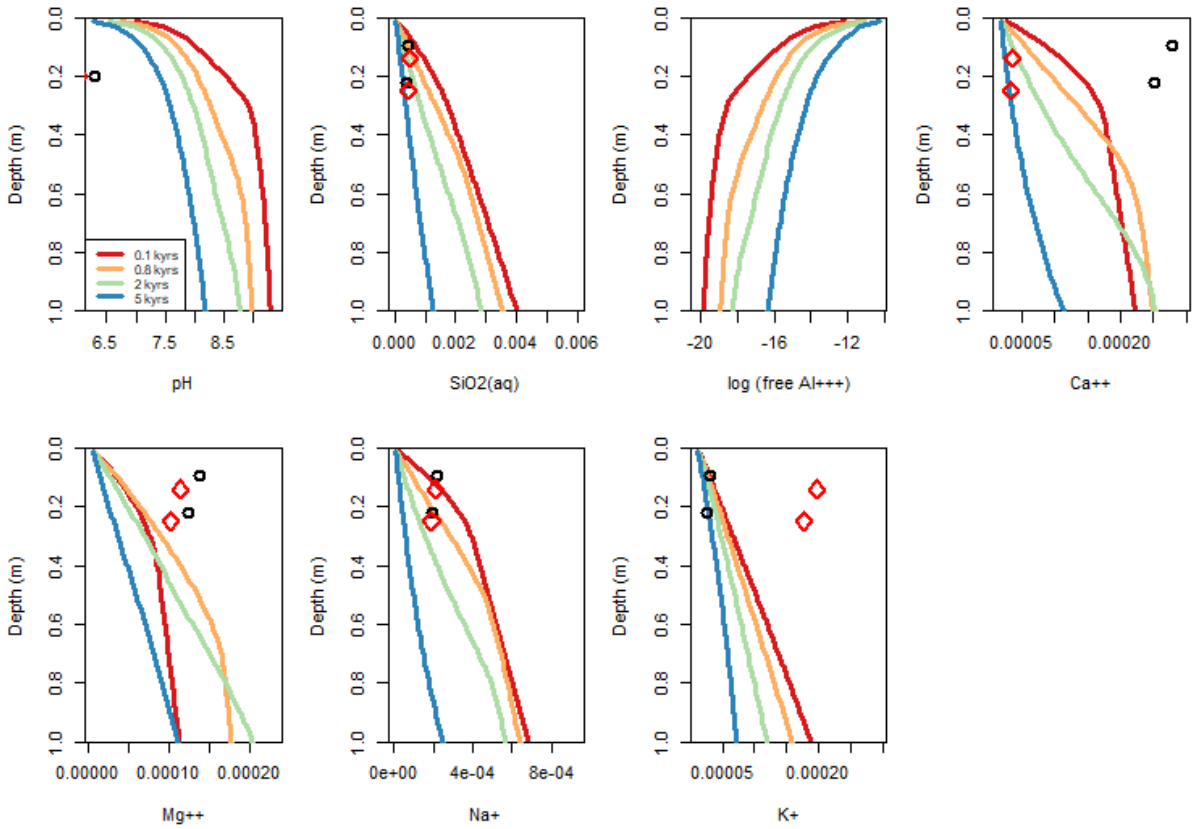

Figure 9. M1 base model prediction of (a) pH, and the concentration in solution of (b) $SiO_{2(aq)}$, (c) free Al^{3+}, (d) Ca^{2+}, (e) Mg^{2+}, (f) Na^+, and (g) K^+. The black circles and the red diamonds correspond to the measured concentration under tussock grasses and cushion plants, respectively.

The volume percentage (%v) of volcanic glass in the weathering profile does not show a weathering front (Figure 10b). Similar to the other primary solid phases (Figure A. 1), its %v decreases with time. After 0.8 and 5 kyr of weathering, the content of volcanic glass is ~22 and ~5 %v, respectively. In contrast to volcanic glass, the plagioclases show a weathering front, which moves downwards with time (Figure 10a). At 0.8 kyr, the weathering profile consists of ~1 %v of plagioclases in the surface and ~8 %v at 1 m depth. The plagioclases disappear completely after 5 kyr of weathering.

During the first 0.8 kyr, ~6 %v of allophanes precipitate in the first 40 cm of the profile (Figure 10c). Between 40 and 60 cm, the %v of allophanes decreases linearly before reaching a steady content (~2 %v) in the rest of the weathering profile. With time, more allophanes precipitate but a dissolution is also observed in the first 5 and 10 cm at 2 and 5 kyr, respectively. The depth at which dissolution occurs also corresponds to the depth at which gibbsite starts to precipitate (~6 and ~8 %v at 2 kyr and 5 kyr, respectively) (Figure 10f). Halloysite and $SiO_{2(am)}$ never precipitate (< 0.1 %v) (Figure 10d, e).

The weathering profile of the other minerals (riebeckite, pargasite, phlogopite and annite) are presented in Figure A. 1.

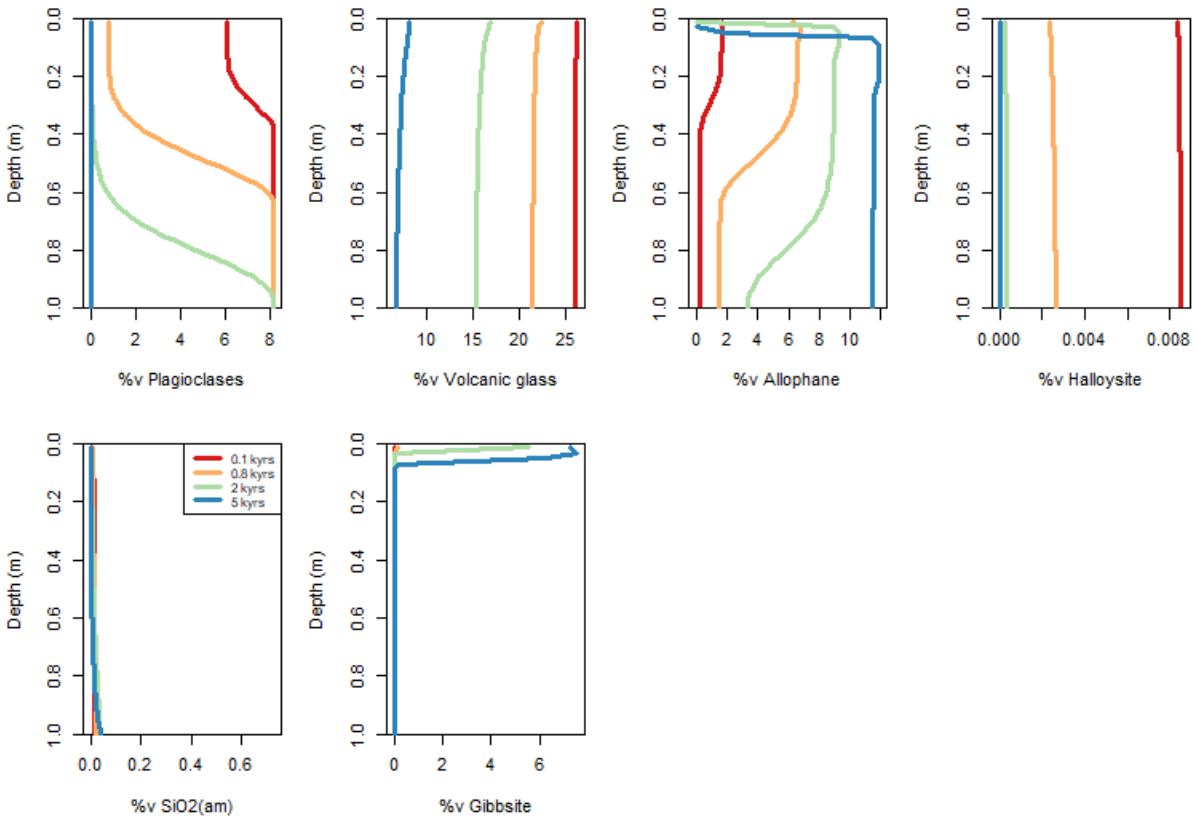

Figure 10. M1 modelled volume percentage of (a) plagioclases, (b) volcanic glass, (c) allophanes, (d) halloysite, (e) $SiO_{2(am)}$, and (f) gibbsite.

Water saturation

Varying soil water saturation may impact some reactions that depend on pH and CO_2 diffusion in the weathering profile. The three levels of saturation tested (30, 50 and 70 %) produce almost identical pH values (< 0.1 pH unit of difference) at 0.8 and 5 kyr (Figure A. 2a). After 0.8 kyr of weathering, the soil solution pH at the bottom of the weathering profile is buffered around 9 for all saturation levels. Regarding the pCO_2, the difference between the three saturation levels is also marginal (< 10^{-4} bars) (Figure A. 2b). At 0.8 kyr, pCO_2 also decreases with increasing saturation level. Given the negligible pH and $SiO_{2(aq)}$, Al^{3+}, Na^{+}, K^{+}, Mg^{2+} and Ca^{2+} profile variations, a water saturation of 50 % will be used in all simulations.

4.2. Increased CO2 as soil respiration (M2)

Similar to the M1 model, the soil solution pH of the M2a and M2b models increases with depth and decreases through time (Figure A. 5a & Figure 11a). For M2a, during the first 0.8 kyr of weathering, the solution remains basic in most of the profile and is buffered at pH ~8. The 5 kyr simulation leads to slightly acidic pH values, i.e. 5.5 < pH < 7, in the weathering profile. The M2a model still overestimates the pH (by one unit) measured for the soil solution collected in

the field. All the simulations of the M2b model result in an acidic soil solution (pH < 7). After 5 kyr, the soil solution has a pH < 6 at all depths. The M2b model predicts a pH ~6.5 at 20 cm at 0.8 kyr, a value which is close to the measured one (i.e. pH = 6.3 and pH = 6.0 under TU and CU, respectively).

The free Al^{3+} concentration is significantly impacted by the increase in CO_2. Compared to the M1 simulation (free Al^{3+} ~10^{-19} mol/L at 1 m depth and 0;8 kyr), it increases by four and seven orders of magnitude in the M2a and M2b models, respectively (Figure A. 5c & Figure 11c). The dissolved $SiO_{2(aq)}$ concentration also increases from ~3.5 10^{-4} mol/L in M1 to ~4.0 10^{-3} mol/L in M2b (Figure 11b).

The concentrations in solution of the other chemical elements decrease with time, but they increase with depth (Figure A. 5 & Figure 11). The depth evolution becomes more linear and the concentration increases are less marked with increasing CO_2 concentration. The differences between M1, M2a and M2b are more pronounced below 40 cm depth. The M2b 0.8 kyr simulation predicts five times less concentration of Ca^{2+}, an increase of ~1.5 times of Na^{+} and K^{+}, and ~2.0 10-^{4} mol/L more Mg^{2+} compared to M1.The 0.8 kyr simulation prediction (M2a and M2b) still correspond to the field measurements at 20 cm depth.

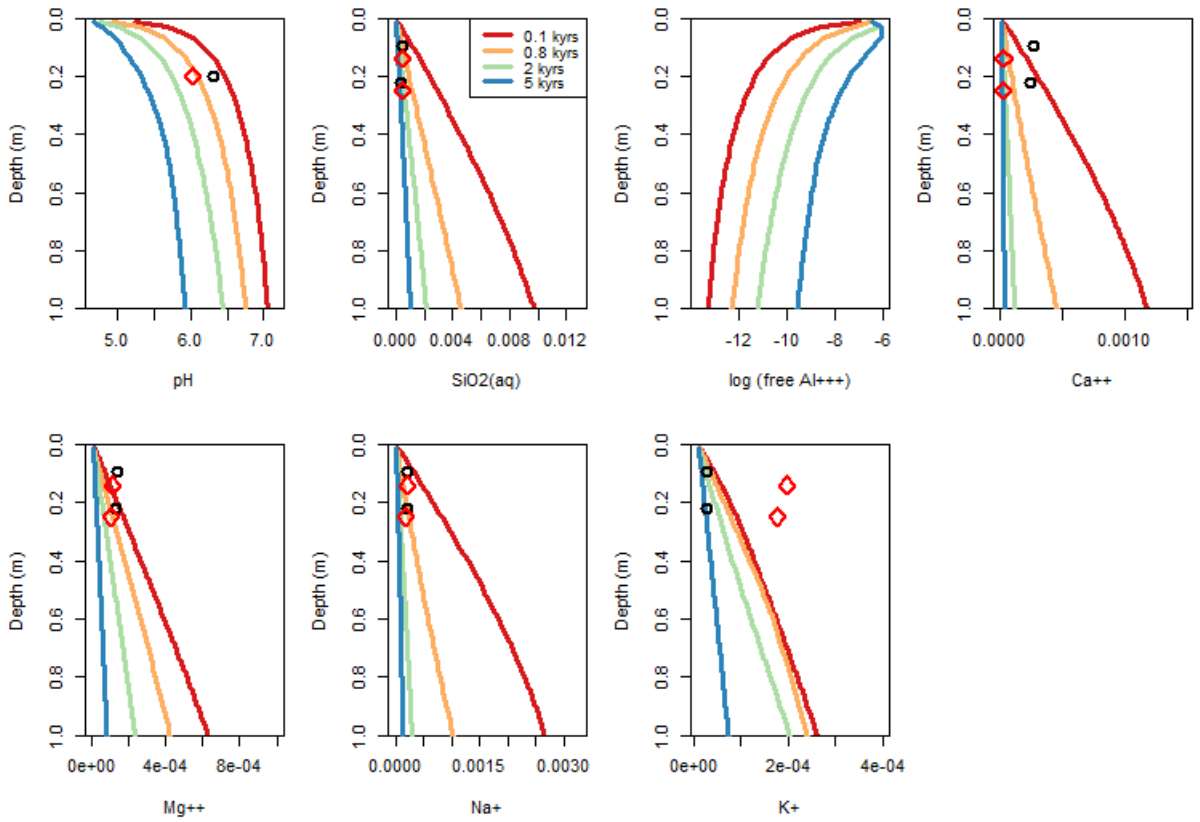

Figure 11. M2b model prediction of (a) pH, and concentrations in solution of (b) $SiO_{2(aq)}$, (c) free Al^{3+}, (d) Ca^{2+}, (e) Mg^{2+}, (f) Na^{+}, and (g) K^{+}. Legend is the same as Figure 9.

With the increase in CO_2 (and lower pH values), the weathering front of the primary solid phases moves downward (Figure 12, Figure A. 6 & Figure A. 9). Eventually, at pCO_2 30 000 ppm, the

precipitation fronts are no longer observed, except for annite. Volcanic glass is the only primary solid phase which is almost not impacted by the increased pCO_2 as it retains the same weathering profile. After 0.8 kyr, the weathering profile in M1, M2a and M2b are comprised of ~21 %v of volcanic glass. The M2b model has ~1 %v of plagioclases at all depths after 0.8 kyr (Figure 12a). Regarding the secondary minerals, a precipitation front is no longer observed for allophanes with the increased CO_2 (Figure A. 6g & Figure 12c). In M2b, the content of allophanes is ~6 %v in the whole profile after 0.8 kyr of weathering. In the 5 kyr simulation, more allophanes (about ~2 %v) precipitate in M2b than in M1. Gibbsite shows an opposite trend (Figure 12 (f)). Like for M1, halloysite and $SiO_{2(am)}$ never precipitate in M2 (Figure 12d, e & Figure A. 6h, i).

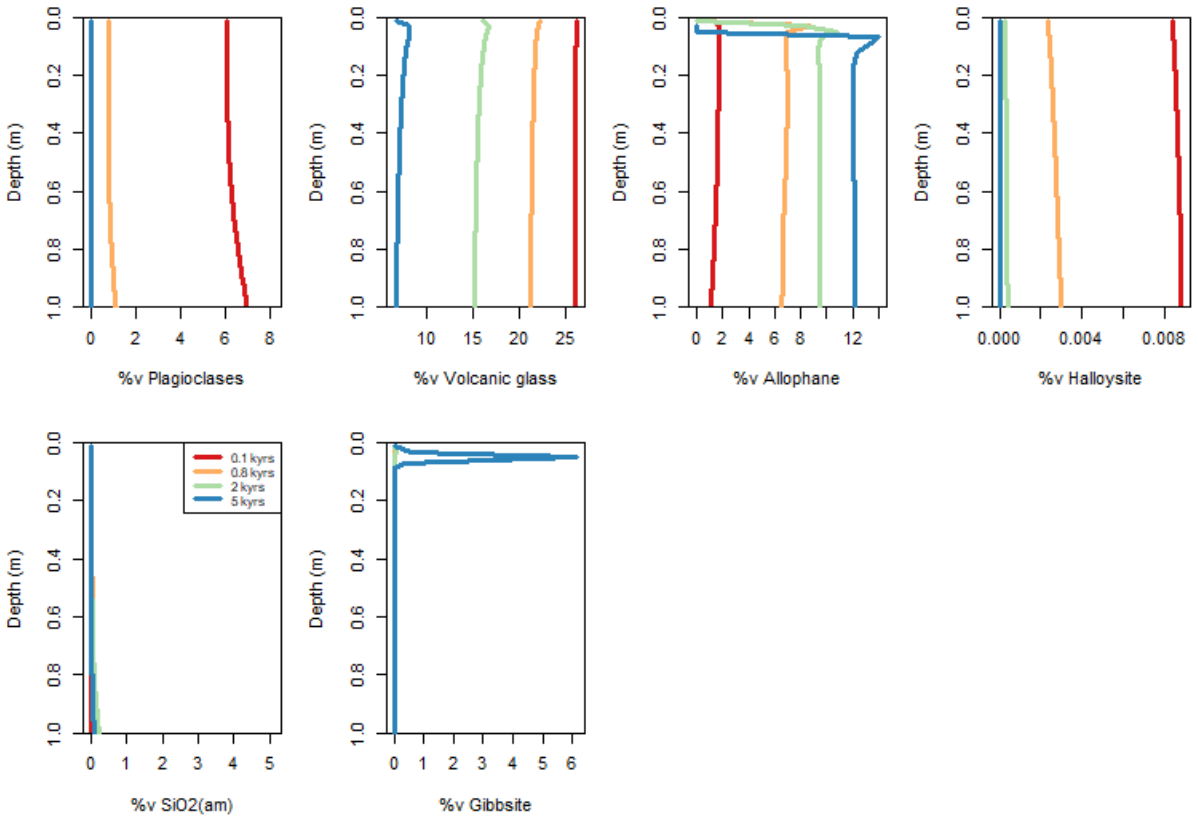

Figure 12. M2b modelled volume percentage of (a) plagioclases, (b) volcanic glass, (c) allophanes, (d) halloysite, (e) $SiO_{2(am)}$, and (f) gibbsite.

The next step of the model creation will be done with the pCO_2 at high level (M3b, 30 000 ppmv), given that it predicts better the pH of the soil solution. This choice can be considered arbitrary as measurements of the soil respiration are unavailable. Nevertheless, it should not matter so much as in the next simulations organic acids will be added and will decrease the soil solution pH.

4.3. Organic acids incorporation (M3)

4.3.1. M3TU model

The M3 model under TU predicts a pH and concentration of $SiO_{2(aq)}$, Ca^{2+}, Mg^{2+}, Na^{+} and K^{+} in solution almost identical to those obtained with the M2b model (Figure 13). The soil solution pH is slightly more acidic (~0.1 unit) (Figure 13a). The M3TU model estimates a soil solution pH of 6 at 20 cm depth after 0.8 kyr, which compares well with the field measurement. Free Al^{3+} concentration increases linearly until a certain depth and then decreases (Figure 13c). After 0.8 kyr, the concentration increases from 10^{-10} to $10^{-8.5}$ mol/L in the first 8 cm. It then decreases down to 10^{-12} mol/L. At 5 kyr, the maximum concentration of Al^{3+} is reached at 15 cm depth, and it is 10 times lower than the maximum concentration obtained in M2b.

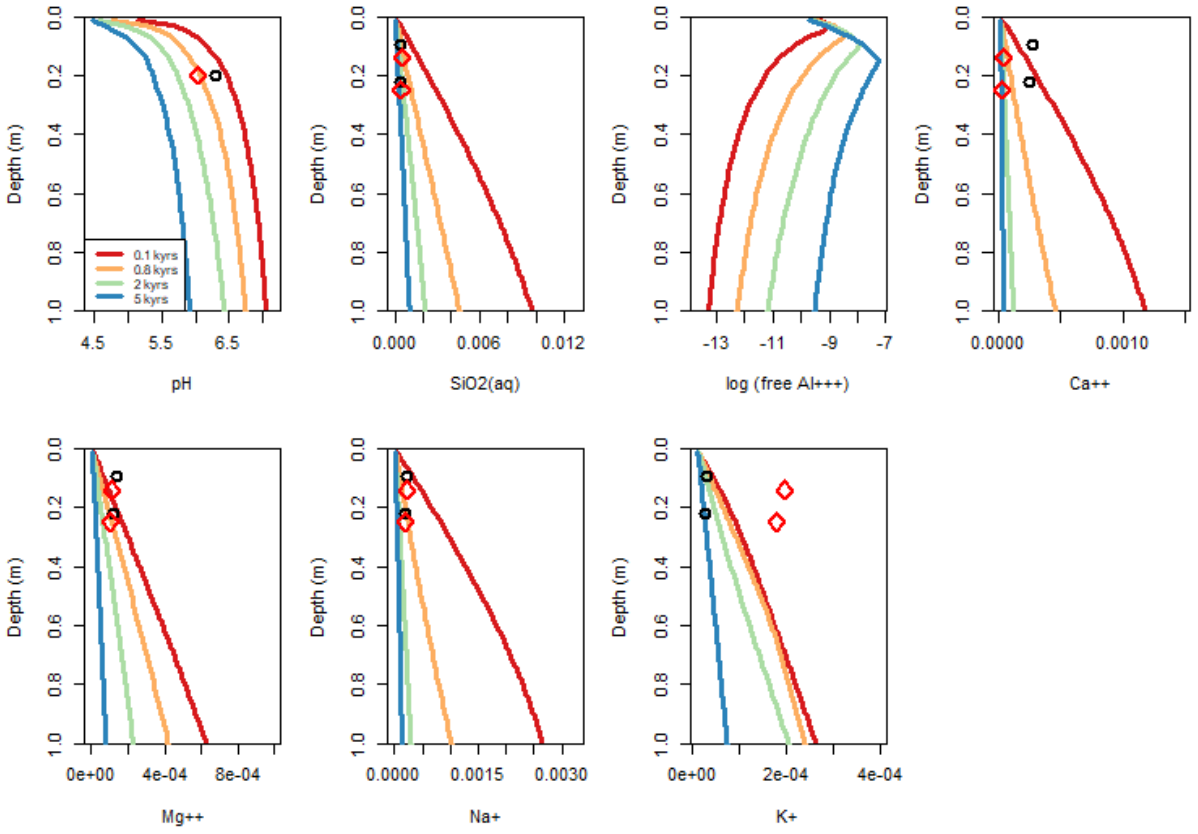

Figure 13. M3TU model prediction of (a) pH, and concentrations in solution of (b) $SiO_{2(aq)}$, (c) free Al^{3+}, (d) Ca^{2+}, (e) Mg^{2+}, (f) Na^{+}, and (g) K^{+}. Legend is the same as Figure 9.

The contents in plagioclases, riebeckite, pargasite, phlogopite, annite, halloysite and $SiO_{2(am)}$ are the same as the M2b model (Figure 14 & Figure A. 11). A weathering front of volcanic glass begins to appear in the first 10 cm of the profile in the M3TU model (Figure 14b). After 0.8 and 5 kyr, the surface of the profile contains ~18 and ~1 %v of volcanic glass, respectively, whereas at 1 m depth the volcanic glass content is 21 and 6 %v, respectively. The allophanes never precipitate in the first 5 cm of the weathering profile (Figure 14c). With time, the allophanes that precipitated at shallower depths first dissolve but then reprecipitate deeper in the profile.

After 0.8 kyr, the allophanes precipitate at 8 cm depth and goes up to 9 %v. At 1 m, the content of allophanes is ~6 %v, similar to what the M2b model's prediction. The M3TU model never predicts gibbsite saturation (< 0.01 %v) (Figure 14f).

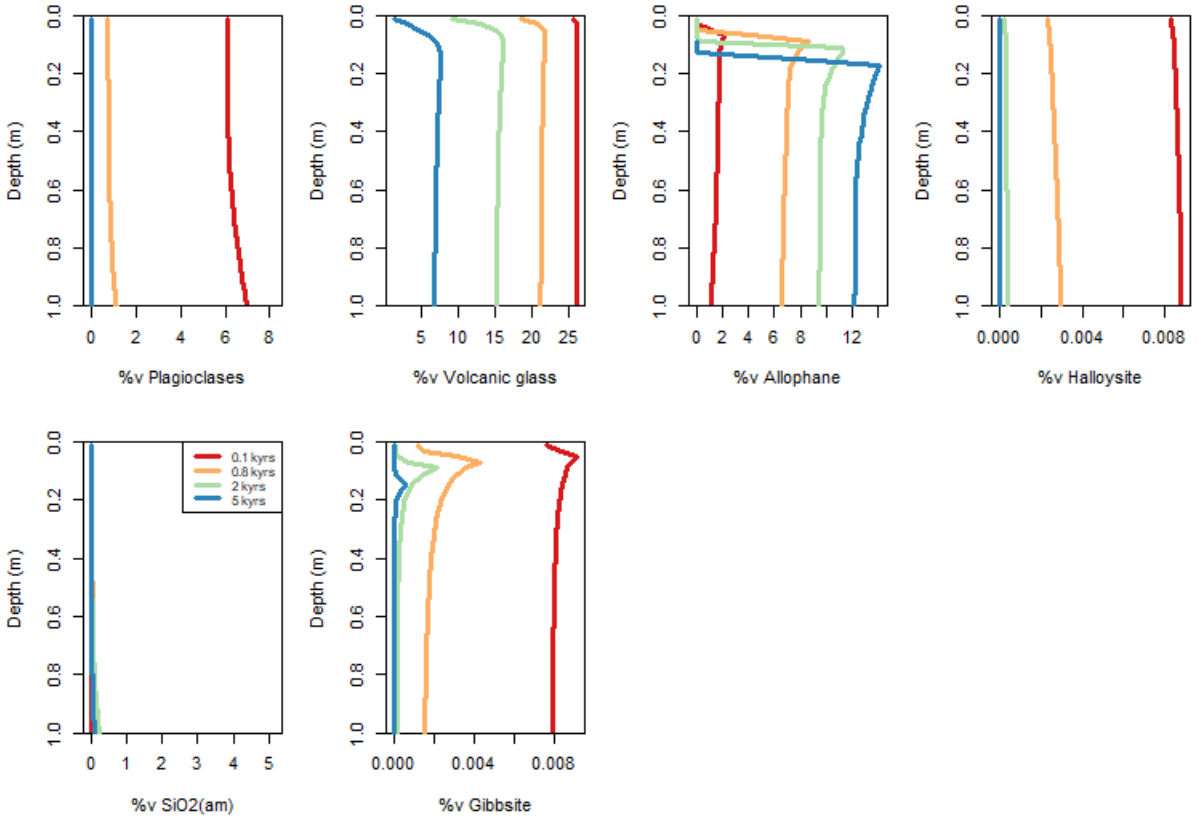

Figure 14. M3TU modelled %v of (a) plagioclases, (b) volcanic glass, (c) allophanes, (d) halloysite, (e) $SiO_{2(am)}$, and (f) gibbsite.

4.3.2. M3CU model

The M3CU model underestimates by 0.5 unit the soil solution pH measured in the soil (at 20 cm depth) under cushion plant vegetation (Figure 15a). After 0.8 kyr, the first 15 cm of the weathering profile solution has a pH < 5, and the bottom of the profile is buffered at ~6.5. After 5 kyr, the half top of the profile has a pH < 5. The concentrations of $SiO_{2(aq)}$, Ca^{2+}, Mg^{2+}, Na^{+} and K^{+} are similar to those obtained in M2b and M3TU (Figure 15). During the first 0.1 kyr of weathering, the free Al^{3+} concentration is also similar to the M3TU model's prediction (Figure 15c). However, the M3TU and M3TCU results start to diverge with increasing weathering duration. The free Al^{3+} concentration at 20 cm depth after 5 kyr predicted by the M3CU model is ~30 % higher than that shown in the M3TU model. After 5 kyr, free Al^{3+} is predicted to increase from 10^{-10} to 10^{-7} mol/L in the first half of the weathering profile, whereas in the second half it decreases linearly to $10^{-8.5}$ mol/L.

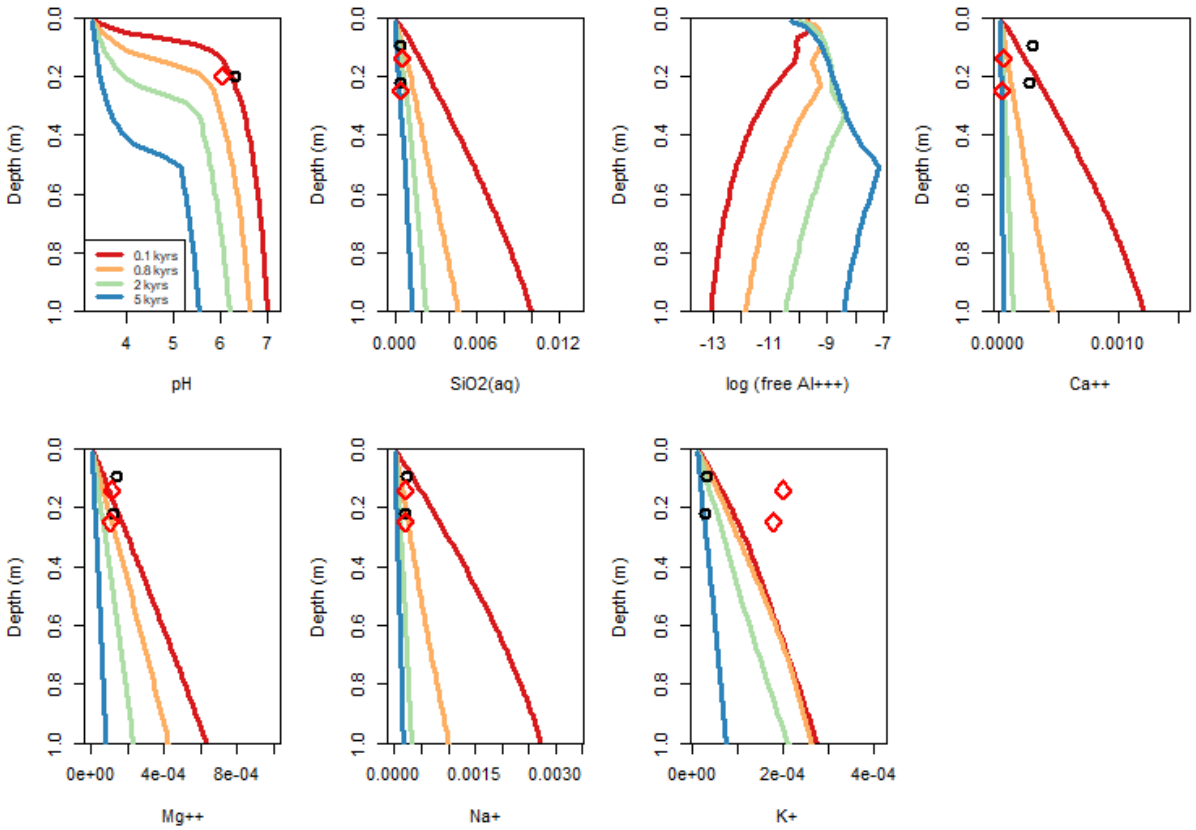

Figure 15. M3CU model prediction of (a) pH, and concentrations in solution of (b) $SiO_{2(aq)}$, (c) free Al^{3+}, (d) Ca^{2+}, (e) Mg^{2+}, (f) Na^{+}, and (g) K^{+}. Legend is the same as Figure 9.

The plagioclases, pargasite, phlogopite and annite, halloysite, $SiO_{2(am)}$ and gibbsite contents are similar to the M3CU model (Figure 16 & Figure A. 13). The volcanic glass weathering profile is more pronounced than that obtained in the M3TU simulation (Figure 16b). After 0.8 kyr of weathering, there are ~10 %v of volcanic glass in the profile surface, compared to ~18 %v in M3TU. After 5 kyr of weathering, the top 20 cm of the profile is devoid of volcanic glass.

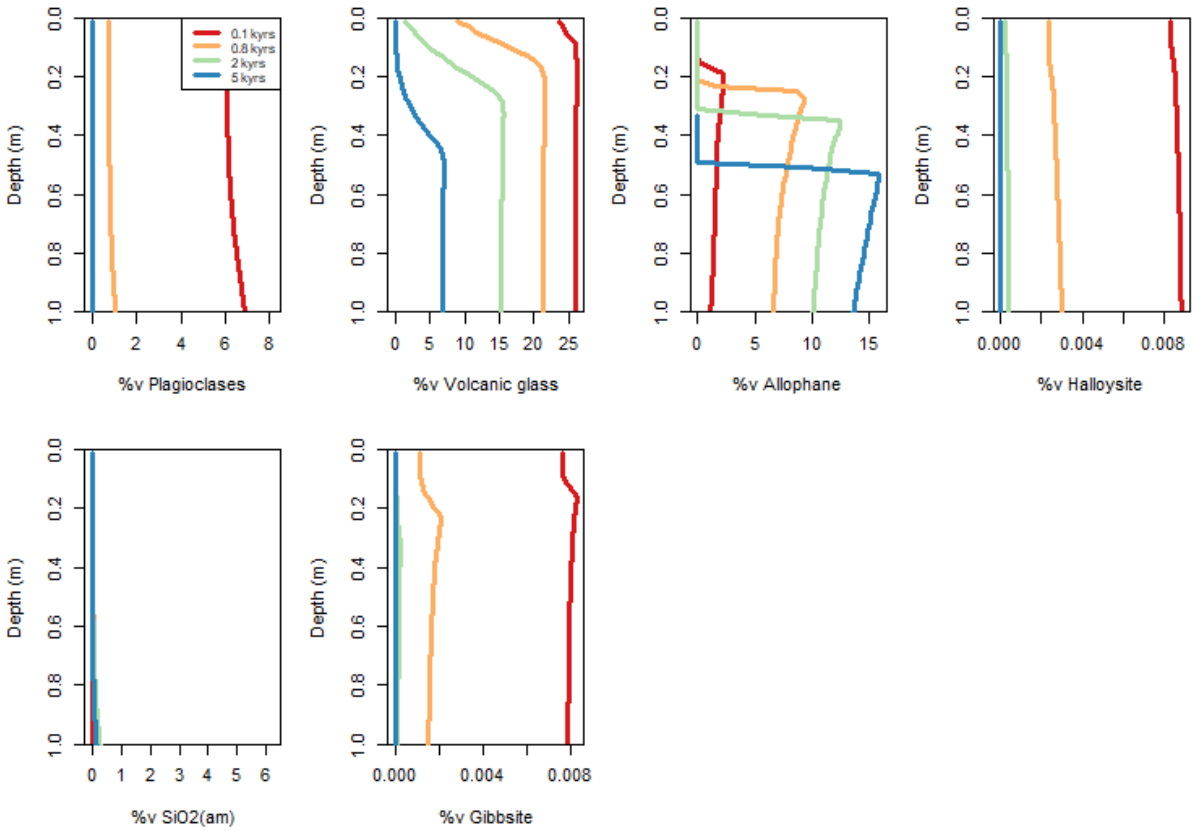

Figure 16. M3CU modelled %v of (a) plagioclases, (b) volcanic glass, (c) allophanes, (d) halloysite, (e) $SiO_{2(am)}$, and (f) gibbsite.

4.4. Modified infiltrating rainwater flow under TU

4.4.1. F1TU model

When the rainwater infiltration flow is decreased to 0.2 m/yr, the pH variation with time is lower (Figure 17a). After 5 kyr of weathering, a pH of ~6.3 is predicted at 1 m depth with the model F1TU whereas the model M3TU predicts a pH of ~6. After 5 kyr, no $SiO_{2(aq)}$, Ca^{2+}, Mg^{2+} and Na^{+} are present in the first 20 cm of the profile (Figure 17).

After 2 and 5 kyr of weathering, the Ca^{2+} concentration is the same in both the F1TU and M3TU simulations. $SiO_{2(aq)}$ and Na^{+} concentrations at 1 m depth are higher in F1TU than in M3TU, both in the 2 and 5 kyr simulations. Aqueous silica concentration at 1 m depth in F1TU is about the double of that obtained in M3TU. After 2 kyr of weathering, the soil solution at 1 m depth is three times less concentrated in Na^{+}. The maximum free Al^{3+} concentration in the 5 kyr simulation is ~30 % lower in the F1TU model than in M3TU and occurred ~5 cm higher in the profile (Figure 17c). After 5 kyr of weathering, a maximum concentration of $10^{-7.5}$ mol/L is predicted at 15 cm depth. The F1TU model's Mg^{2+} concentration at 1 m depth after 2 kyr of weathering is more than the double of that in the M3TU. After 2 kyr of weathering, the K^{+} concentration at 1 m depth is 2 to 3 times higher in F1TU than in M3TU (Figure 17g). After 5 kyr, the soil solution comprises ~2 10^{-3}, 10^{-11}, 6 10^{-5} mol/L of $SiO_{2(aq)}$, free Al^{3+}, Ca^{2+}, respectively. It also contains 2 10^{-4} mol/L of Mg^{2+}, Na^{+} and K^{+}.

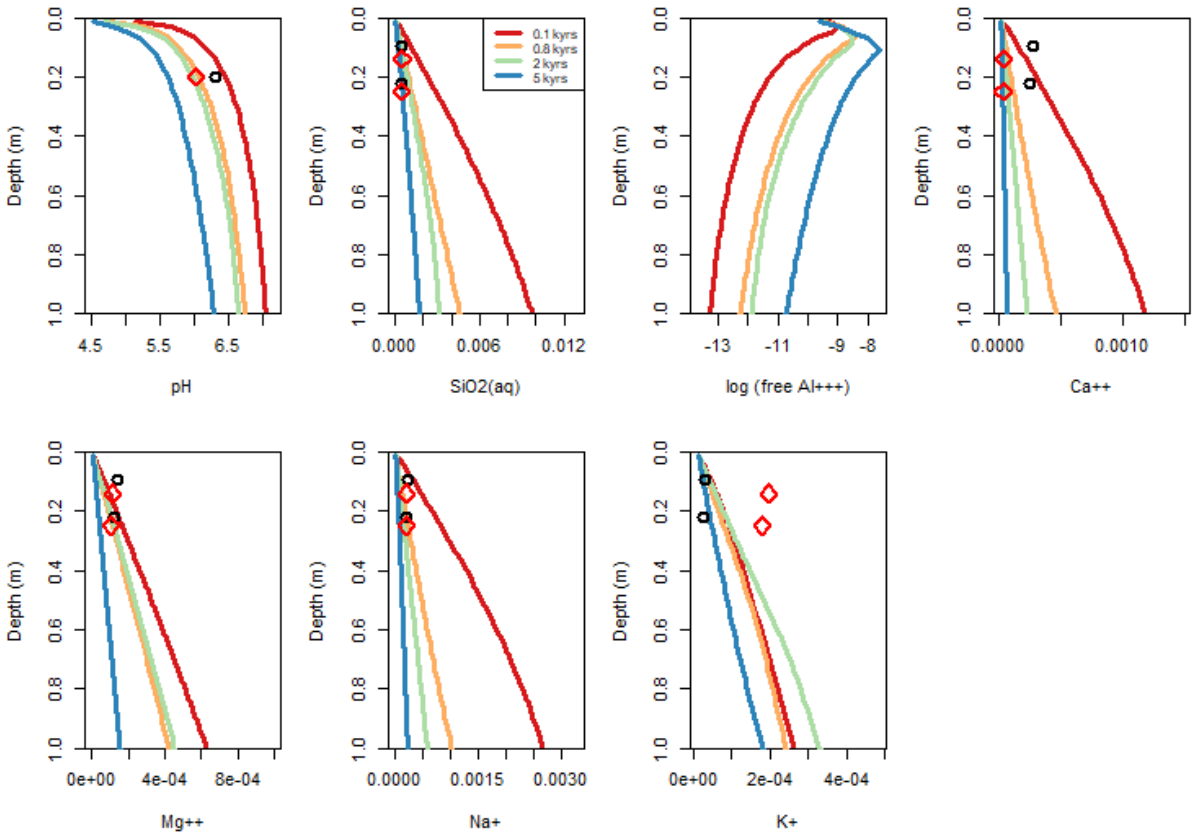

Figure 17. F1TU model prediction of (a) pH, and concentrations in solution of (b) $SiO_{2(aq)}$, (c) free Al^{3+}, (d) Ca^{2+}, (e) Mg^{2+}, (f) Na^{+}, and (g) K^{+}. Legend is the same as Figure 9.

Plagioclases, pargasite, phlogopite and volcanic glass contents are the same as those deduced in M3TU (Figure 18a & Figure A. 15b, c). The riebeckite and annite weathering fronts are moving upwards with the lower rainwater infiltration flow (Figure A. 15a, d). After 5 kyr, the first 5 cm of the weathering profile contains < 5 %v of volcanic glass, whereas the bottom contains ~7 %v (Figure 18b). The allophanes precipitate ~5 cm higher in the profile in F1TU compared to M3TU (Figure 18c). After 5 kyr of weathering, the allophanes content is ~15 %v at ~15 cm depth and 12-13 %v at the bottom of the profile. Halloysite and gibbsite never precipitate (Figure 18d,f). Between 0.8 and 1 m depth, a low amount of $SiO_{2(am)}$ precipitates (~1 %v) (Figure 18e).

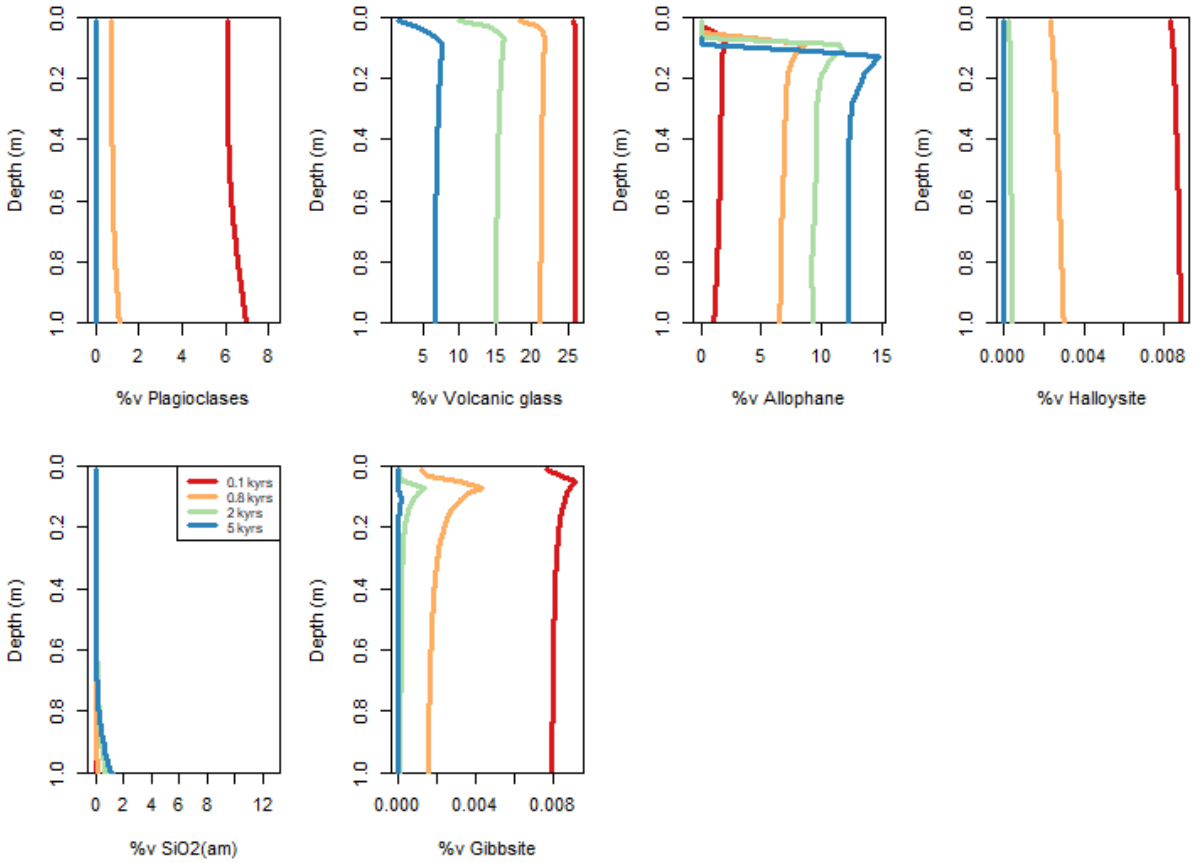

Figure 18. F1TU modelled %v of (a) plagioclases, (b) volcanic glass, (c) allophanes, (d) halloysite, (e) $SiO_{2(am)}$, and (f) gibbsite.

4.4.2. F2TU model

The model F2TU results in slightly more acidic pH than the model M3TU (Figure 19a). After 2 and 5 kyr of weathering, the soil solution pH at 1 m depth, is ~0.2 units lower than in the M3TU model. After 5 kyr, F2TU predicts a soil solution pH of 4.5 and 5.8 at the surface of the profile and at 1 m depth, respectively.

The concentration in Ca^{2+} after 2 kyr and 5 kyr of weathering in the F2TU model (Figure 19d) is the same as in the M3TU model. The concentrations of the $SiO_{2(aq)}$, Mg^{2+}, Na^{+} and K^{+} concentrations are all lower in the F2TU simulation (Figure 19) than in the M3TU simulations. The difference of concentrations in these elements at 1 m depth after 2 kyr of weathering are all < 10^{-4} mol/L. After 5 kyr of weathering, the soil solution will be free of Ca^{2+} and Na^{+} according to the F2TU model. Aqueous silica and Mg^{2+} will still be present in the lower half of the profile in very low concentration (< 7 10^{-4} and < 6 10^{-5} mol/L, respectively). Potassium will be present in most of the profile. After 5 kyr of weathering, the K^{+} concentration at the bottom of the profile is ~5 10^{-5} mol/L. The higher infiltration flow rate results in ~30 % higher concentration of free Al^{3+} at the bottom of the profile for the F2TU model (Figure 19c) compared to M3TU. The 5 kyr simulation predicts an increase of 10^{-10} to 10^{-7} mol/L in the first 20 cm of the profile. This increase is followed by a linear decrease to 10^{-9} mol/L.

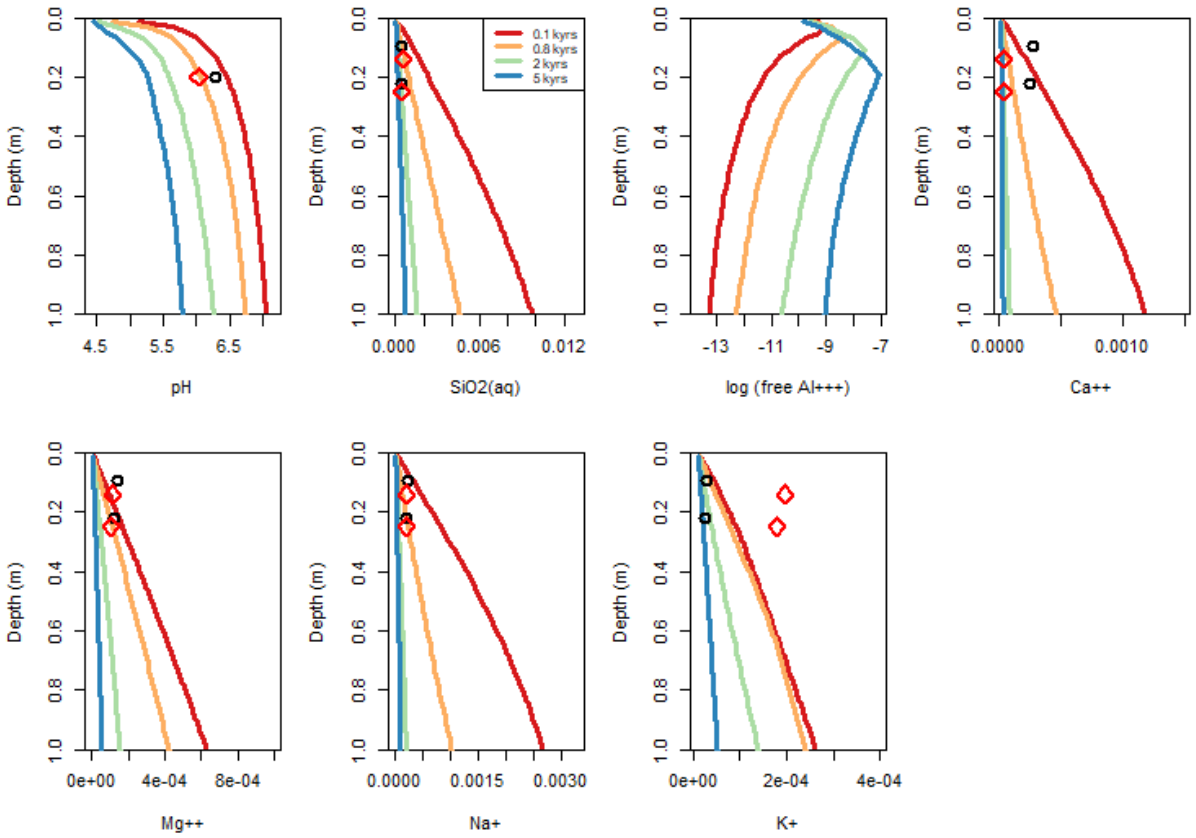

Figure 19. F2TU model prediction of (a) pH, and concentrations in solution of (b) $SiO_{2(aq)}$, (c) free Al^{3+}, (d) Ca^{2+}, (e) Mg^{2+}, (f) Na^{+}, and (g) K^{+}. Legend is the same as Figure 9.

Plagioclases, pargasite, phlogopite and volcanic glass have the same weathering profiles as those obtained in M3TU (Figure 20a,b & Figure A. 19b, c). Riebeckite's weathering profile is moved downwards in F2TU (Figure A. 19a). In M3TU, after 5 kyr, riebeckite does not dissolve below 60 cm, whereas in F2TU the mineral continues to dissolve until 80 cm of depth. After 5 kyr of weathering, the volcanic glass content increases linearly in the first 15 cm of depth, and then stabilises at ~7 %v. Halloysite, $SiO_{2(am)}$ and gibbsite never precipitate (Figure 20d,e,f). Allophanes start to precipitate at lower depths than in M3TU (Figure 20c). After 5 kyr, they start to precipitate at ~20 cm compared to ~15 cm in M3TU. After 5 kyr, the profile contains 14 %v of allophanes at 20 cm and 12 %v at the 1 m depth.

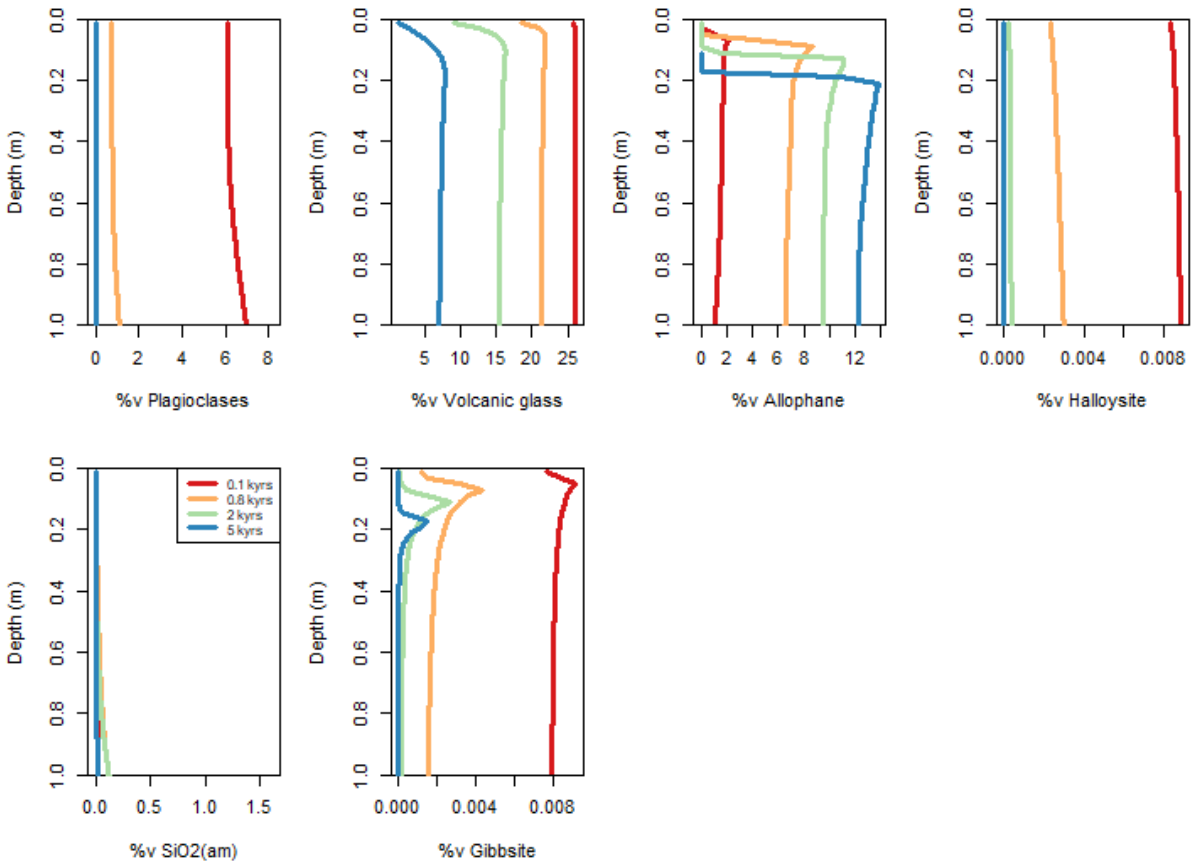

Figure 20. F2TU modelled %v of (a) plagioclases, (b) volcanic glass, (c) allophanes, (d) halloysite, (e) $SiO_{2(am)}$, and (f) gibbsite

4.4.3. F3TU model

The F2TU and F3TU models produce similar profiles of the $SiO_{2(aq)}$, Ca^{2+}, Mg^{2+}, Na^{+} and K^{+} concentrations (Figure 21). In the 2 and 5 kyr simulations of F3TU, free Al^{3+} concentration decreases after 15 and 22 cm, respectively, whereas in F2TU it does after 12 and 20 cm, respectively (Figure 21c). The maximum concentration of free Al^{3+} is almost 1.5 times higher in F3TU compared to that obtained in F2TU. At 1 m depth, free Al^{3+} concentration is $\sim 10^{-9}$ mol/L both in F3TU and F2TU.

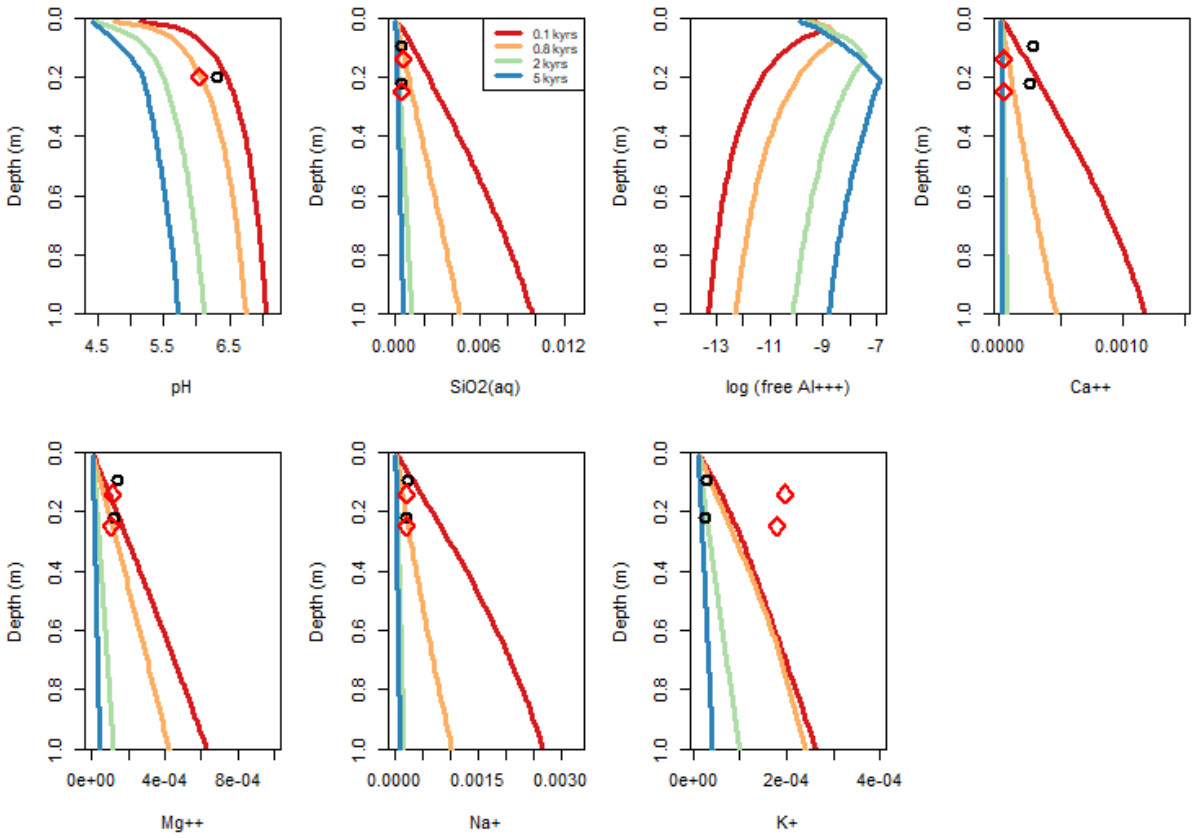

Figure 21. F3TU model prediction of (a) pH, and concentrations in solution of (b) $SiO_{2(aq)}$, (c) free Al^{3+}, (d) Ca^{2+}, (e) Mg^{2+}, (f) Na^{+}, and (g) K^{+}. Legend is the same as Figure 9.

The F2TU and F3TU models produce the same weathering profiles of plagioclases, pargasite, phlogopite, annite and volcanic glass (Figure 22a, b & Figure A. 27). Riebeckite dissolves all the way down in the profile in F3TU (Figure A. 27a). In F3TU, the riebeckite weathering front is lower than in F2TU. After 5 kyr of weathering, riebeckite dissolves at all depths in F3TU, whereas it does not below 80 cm in F2TU. The allophanes precipitate at a deeper depth (when the free Al^{3+} concentration starts to decrease) (Figure 22c) in comparison to F2TU. Similar to F2TU, halloysite, $SiO_{2(am)}$ and gibbsite never precipitate (Figure 22d, e, f).

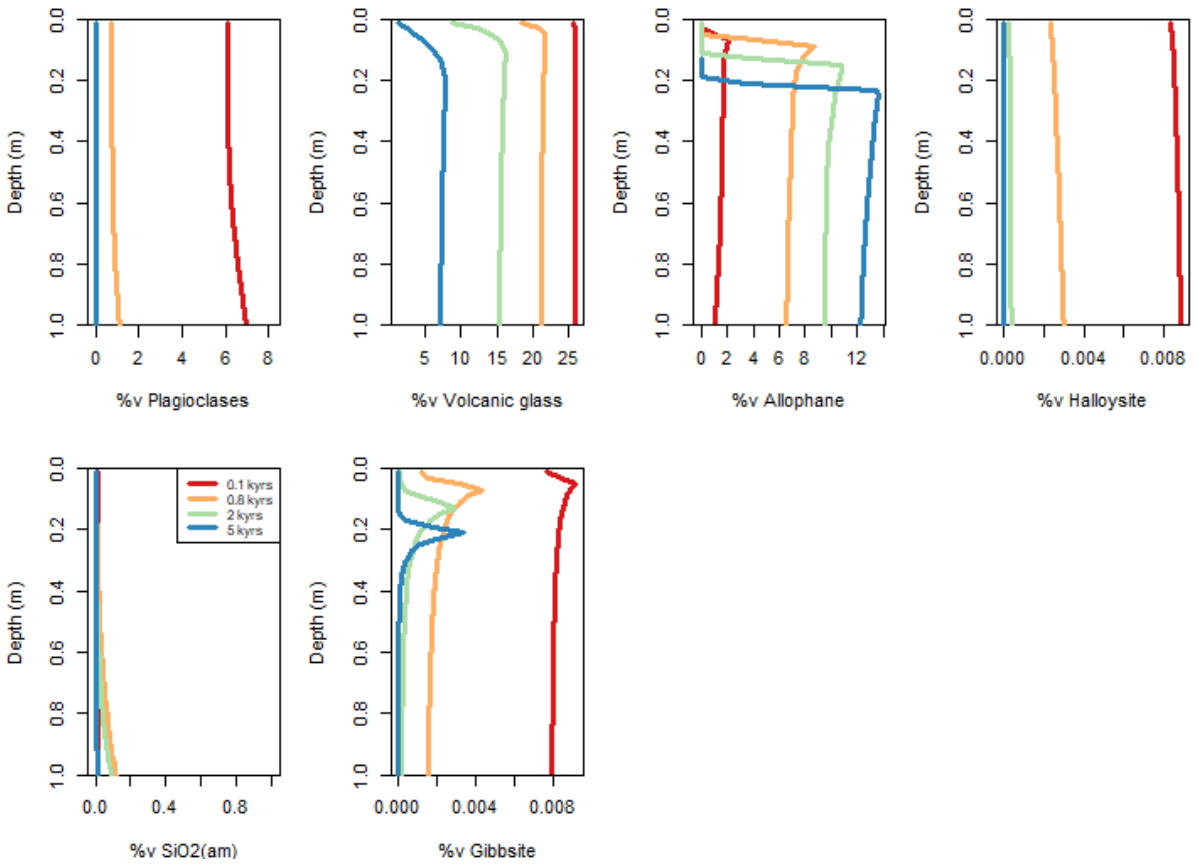

Figure 22. F3TU modelled %v of (a) plagioclases, (b) volcanic glass, (c) allophanes, (d) halloysite, (e) $SiO_{2(am)}$, and (f) gibbsite.

4.5. Modified infiltrating rainwater flow under CU

4.5.1. F1CU model

During the first 25 cm and below 50 cm, the soil solution pH increases by a 0.5 unit when the rainwater flow is decreased from 0.4 to 0.6 m/yr (Figure 23a). Between these two depths, F1CU gives a pH up to 1.5 times higher than M3CU. The soil solution pH values obtained after 0.2 kyr of weathering are similar to those predicted for the 0.8 kyr simulation. After 5 kyr of weathering, the soil solution pH is < 5 in the first 35 cm of the profile and at ~6 at 1 m depth.

Aqueous silica, Ca^{2+}, Mg^{2+}, Na^{+} and K^{+} concentration increases with depth (Figure 23). Their concentrations after 2 and 5 kyr are higher compared to those obtained in M3CU. With time, the $SiO_{2(aq)}$, Ca^{2+} and Na^{+} concentrations decrease in the weathering profile. The F1CU model's $SiO_{2(aq)}$ concentration at the bottom of the profile is higher by ~5 10^{-4} mol/L compared to M3CU. After 2 and 5 kyr of weathering, the Na^{+} concentration is respectively, ~3 10^{-4} and ~1 10^{-4} mol/L higher than the values produced in M3CU. After 2 kyr of weathering, Ca^{2+} concentration is ~3 10^{-4} mol/L higher than in M3 CU, whereas after 5 kyr, the concentrations are similar in both models. The Mg^{2+} concentration in the 0.2 kyr simulation is similar to that generated after 0.8 kyr of weathering. After 5 kyr, the Mg^{2+} concentration is ~10^{-4} mol/L higher than in M3CU. The K^{+} concentration in the 2 kyr simulation is higher than the concentration in the 0.1 and 0.8 kyr simulations and is 1.5-2 times higher than in M3CU. After 5 kyr of weathering, K^{+}

concentration is ~10^{-4} mol/L higher than in M3CU. Similar to the results obtained in M3CU, the free Al^{3+} concentration decreases with depth and increases with time (Figure 23c). Both in the 2 and 5 kyr simulations, free Al^{3+} concentration is lower by an order of magnitude than in M3CU.

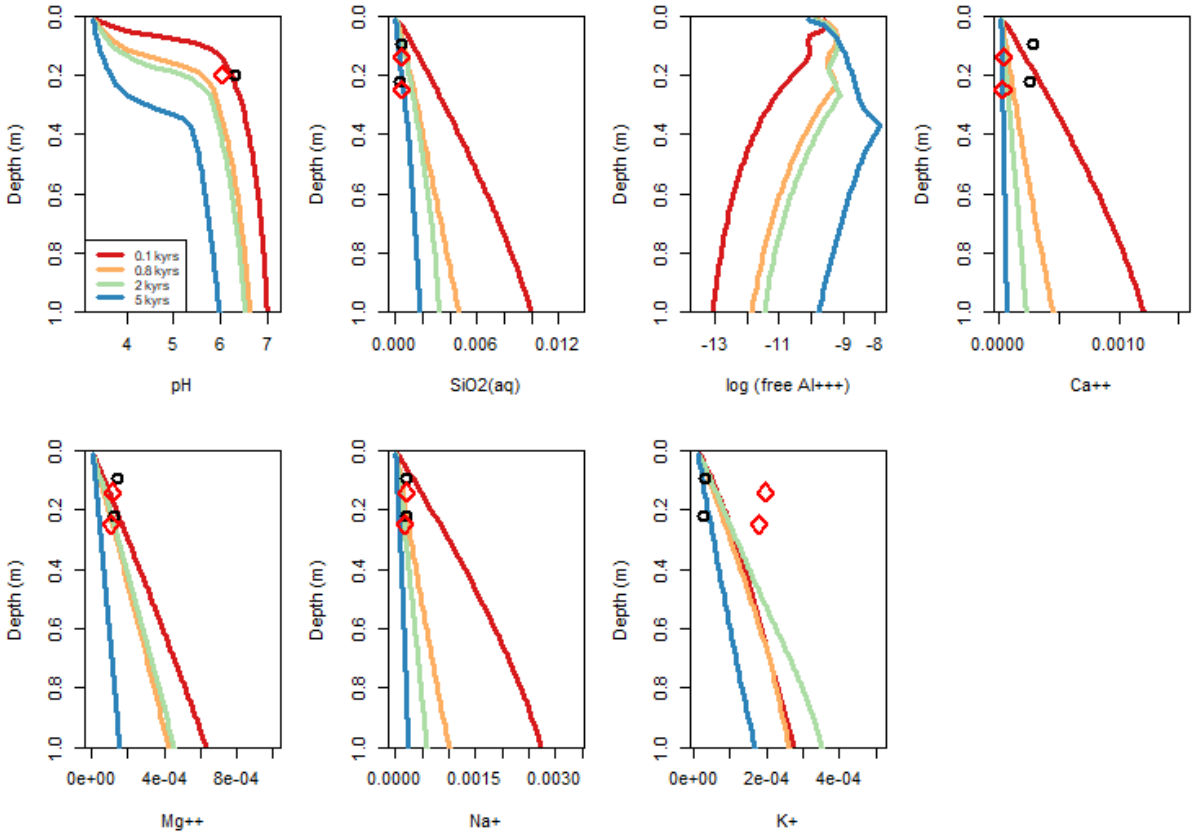

Figure 23. F1CU model prediction of (a) pH, and concentrations in solution of (b) $SiO_{2(aq)}$, (c) free Al^{3+}, (d) Ca^{2+}, (e) Mg^{2+}, (f) Na^{+}, and (g) K^{+}. Legend is the same as Figure 9.

The weathering profile's contents in plagioclases, pargasite and phlogopite are the same as those obtained in the M3CU model (Figure 24a & Figure A. 17b, c). Riebeckite, annite and volcanic glass weathering fronts move upward when the flow is lowered to 0.2 m/yr (Figure 24b & Figure A. 17a, d). In the 5 kyr simulation, riebeckite only dissolves during the first 55 cm in F1CU, whereas it dissolves at all depths in M3CU. After 2 kyr of weathering, annite content at 1 m depth is 1.2 and 0.3 %v in F1CU and M3CU, respectively. After 2 kyr of weathering, volcanic glass content is 15 %v below 20 and 25 cm, in F1CU and M3CU, respectively. The allophanes precipitation front moves upward when the water flow has decreased (Figure 24c). After 5 kyr of weathering, their precipitation starts at ~35 cm depth and reaches ~17 %v. After 5 kyr of weathering, $SiO_{2(am)}$ precipitates up to 2 %v between 0.8 and 1 m, whereas it never precipitates in M3CU (Figure 24e). Similar to M3CU, halloysite and gibbsite never precipitate (Figure 24d, f).

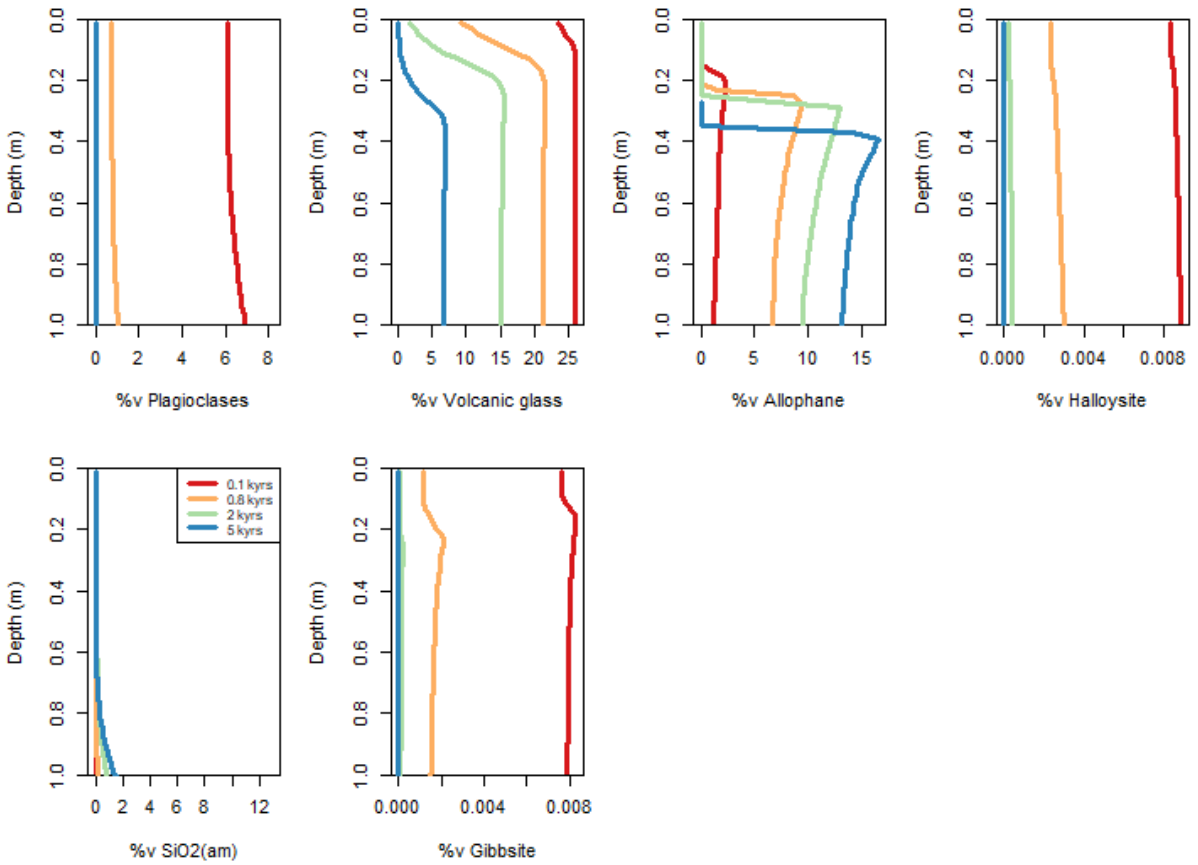

Figure 24. F1CU modelled %v of (a) plagioclases, (b) volcanic glass, (c) allophanes, (d) halloysite, (e) $SiO_{2(am)}$, and (f) gibbsite.

4.5.2. F2CU model

The soil solution pH becomes more acid with rainwater flow increased from 0.4 to 0.6 m/yr (Figure 25a). In the 5 kyr simulation, between 50 and 60 cm depth, the pH is up to 1.5 units lower in F2CU than in M3CU. Above 50 cm and below 60 cm, the differences of pH between F2CU and M3CU is little (F2CU has a pH lower by ~0.2 units). Aqueous silica, Ca^{2+}, Mg^{2+} and Na^{+} concentrations are slightly lower (1-2 10^{-4} mol/L) compared to M3CU (Figure 25). The 2 kyr simulation K^{+} concentration is lower by ~5 10^{-4} mol/L compared to M3CU (Figure 25g). The free Al^{3+} concentration predicted at 2 and 5 kyr are higher by ~30 % at 1m depth in F2CU than in M3CU (Figure 25c). The maximum free Al^{3+} concentration (10^{-7} mol/L) is reached at 65 and 50 cm in F2CU and F3CU, respectively.

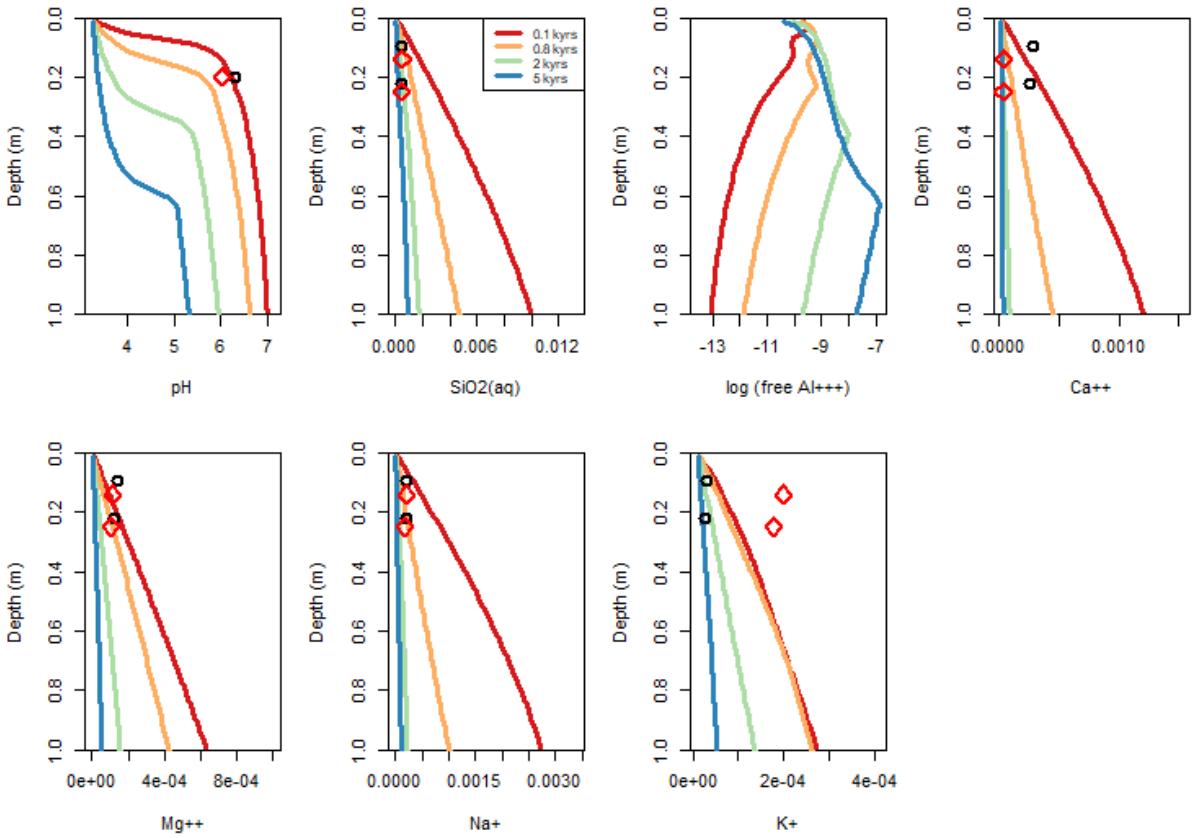

Figure 25. F2CU model prediction of (a) pH, and concentrations in solution of (b) $SiO_{2(aq)}$, (c) free Al^{3+}, (d) Ca^{2+}, (e) Mg^{2+}, (f) Na^{+}, and (g) K^{+}. Legend is the same as Figure 9.

The plagioclases, pargasite and phlogopite contents are not influenced by the increased water flow (Figure 26a & Figure A. 23b, c). Riebeckite and volcanic glass weathering profiles move downwards (Figure 26b & Figure A. 23a). After 5 kyr of weathering, riebeckite content is 1.7 and 0.5 %v at 1 m depth in M3CU and F2CU, respectively. In the 5 kyr simulation, volcanic glass content stabilises at 6-7 %v below 45 and 60 cm in M3CU and F2CU, respectively. With the increased water flow, the allophanes only precipitate from 60 cm depth compared to 50 cm with M3CU (Figure 26c). Halloysite, $SiO_{2(am)}$ and gibbsite never precipitate in M3CU and F2CU (Figure 26d, e, f).

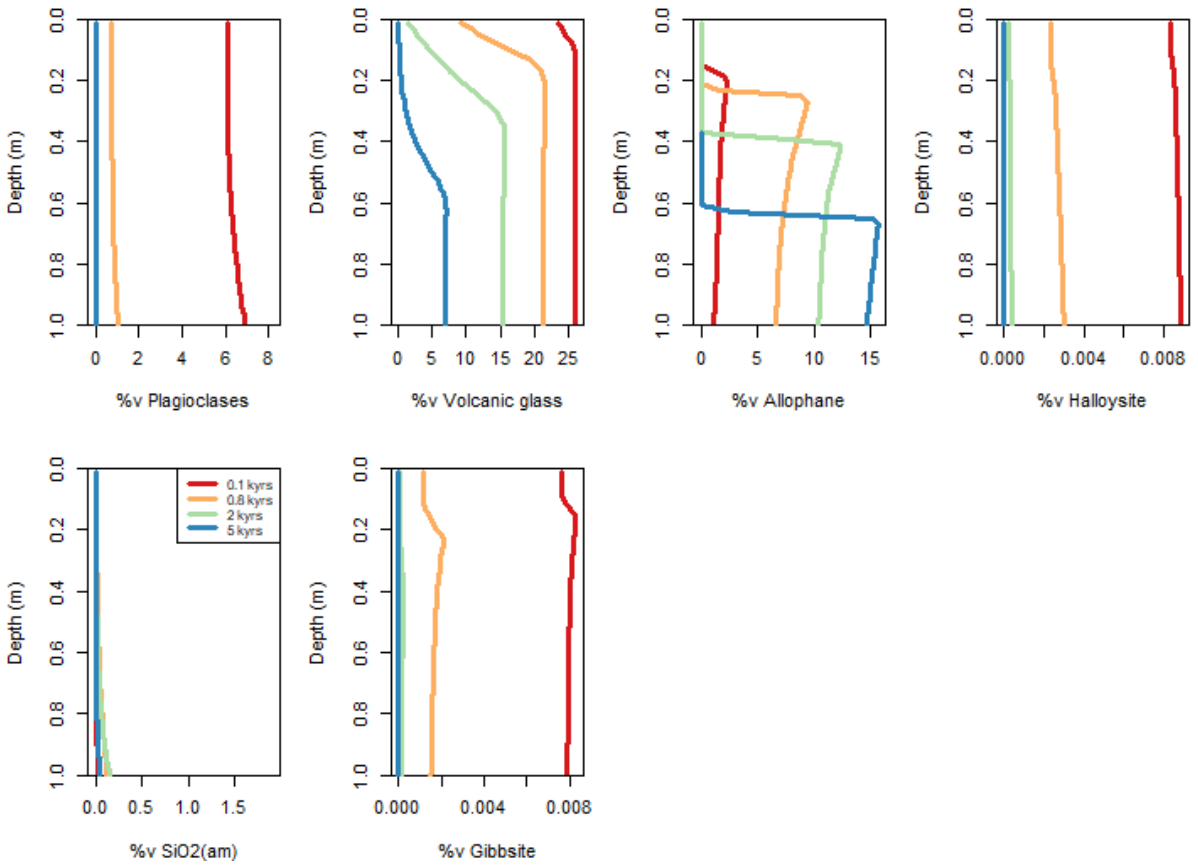

Figure 26. F2CU modelled %v of (a) plagioclases, (b) volcanic glass, (c) allophanes, (d) halloysite, (e) $SiO_{2(am)}$, and (f) gibbsite.

4.5.3. F3CU model

With a rainwater flow of 0.8 m/yr, the pH decreases even more and reaches pH ~5 at the bottom of the profile after 5 kyr of weathering (Figure 27a). The concentrations of $SiO_{2(aq)}$, Ca^{2+}, Mg^{2+}, Na^{+} and K^{+} decrease slightly (~1-2 10^{-4} mol/L) compared to F2CU (Figure 27). Free Al^{3+} concentration is higher in F3CU than in F2CU at 1 m depth (Figure 27c). After 5 kyr of weathering, there are 10 times more free Al^{3+} in solution at 1 m depth than in F2CU.

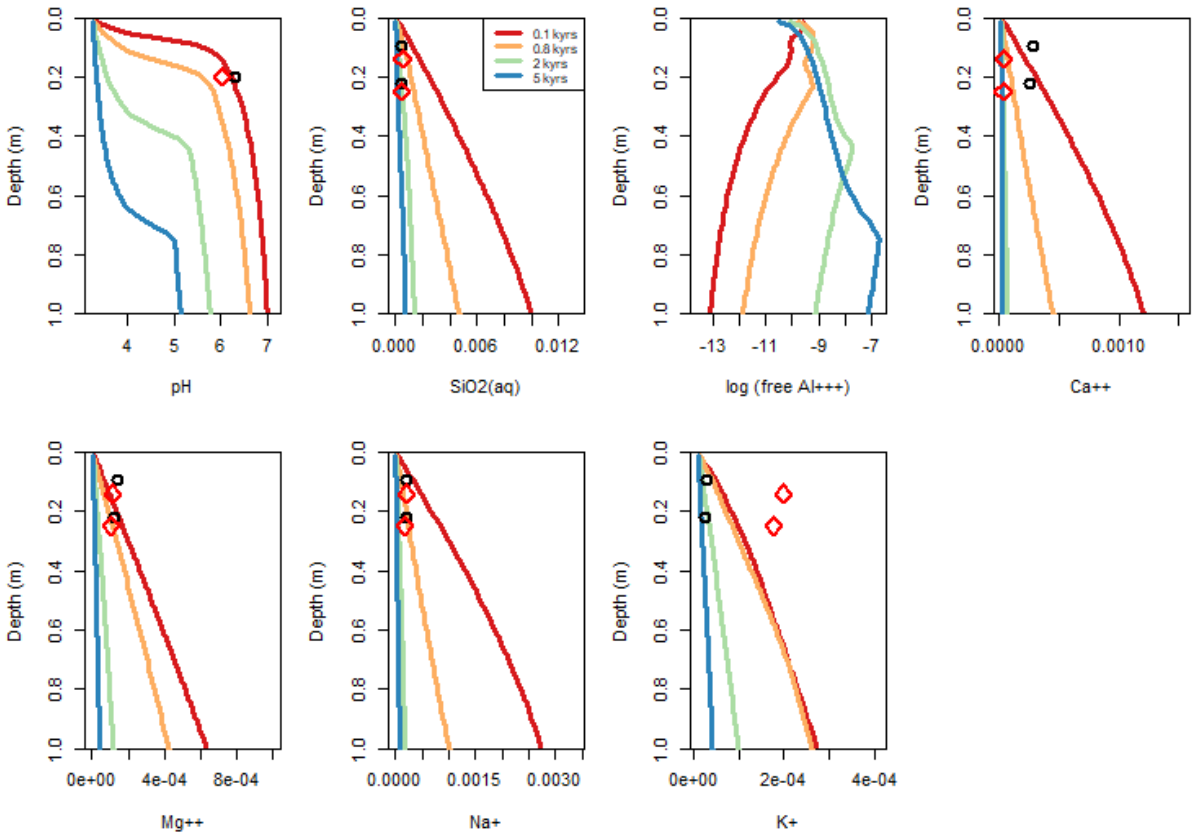

Figure 27. F3CU model prediction of (a) pH, and concentrations in solution of (b) $SiO_{2(aq)}$, (c) free Al^{3+}, (d) Ca^{2+}, (e) Mg^{2+}, (f) Na^{+}, and (g) K^{+}. Legend is the same as Figure 9.

Similar to the F2CU model, the weathering profile contents in plagioclases, pargasite, phlogopite, halloysite, $SiO_{2(am)}$ and gibbsite are not influenced by a higher water flow (Figure 28 & Figure A. 30). Riebeckite and volcanic glass' weathering fronts further move downward (Figure A. 30a & Figure 28b). After 5 kyr of weathering, 0.3 %v of riebeckite is left at the bottom of the profile. In the 5 kyr simulation of F3CU, the volcanic glass content stabilises at 70 cm, whereas it stabilises at 55 cm in F2CU. In that same simulation, the allophanes only precipitate after 75 cm in F3CU, compared to 60 cm with F2CU (Figure 28c).

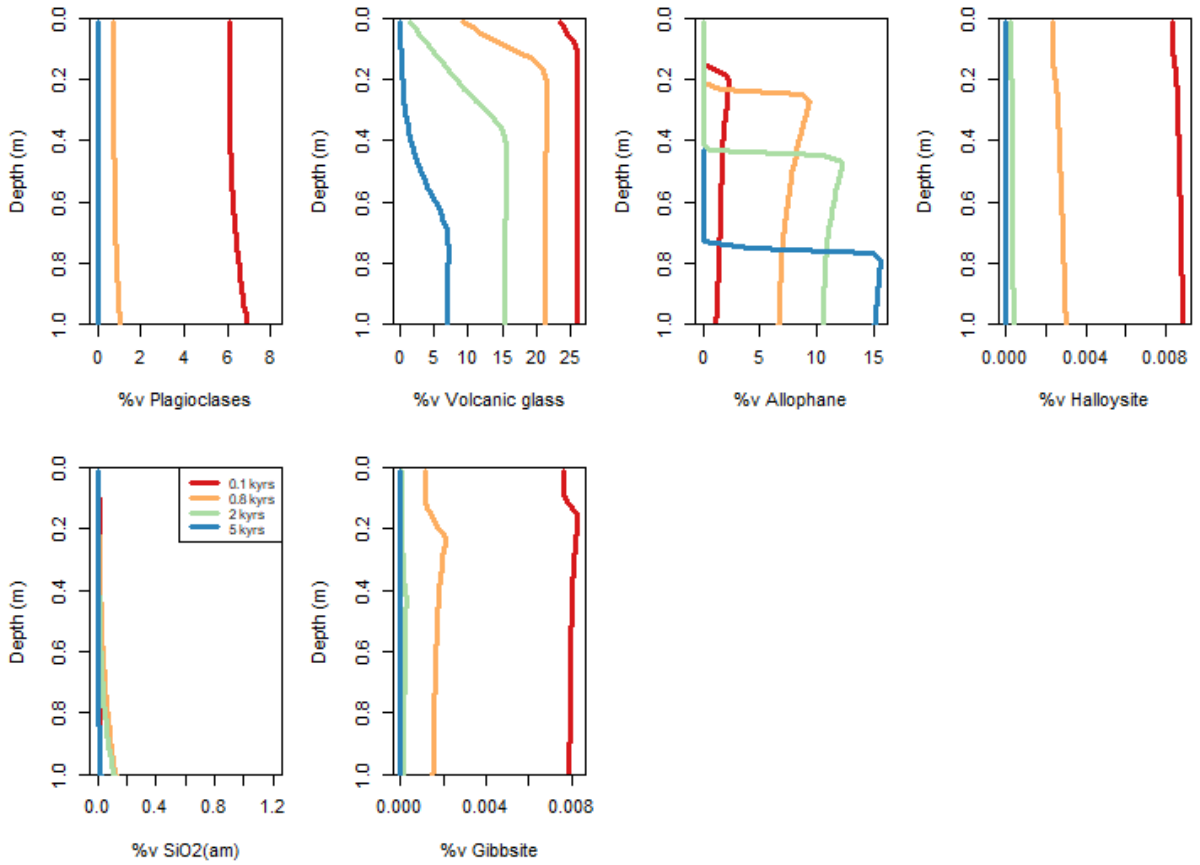

Figure 28. F3CU modelled %v of (a) plagioclases, (b) volcanic glass, (c) allophanes, (d) halloysite, (e) $SiO_{2(am)}$, and (f) gibbsite.

5. Discussion

5.1. Base model (M1)

The M1 simulation predicts that the soil solution maintains basic pH values in most of the weathering profile (Figure 9a). This is due to CO_2 limitation, i.e. weathering is acid-limited. As supported by the positive saturation index (SI) values (Figure 30 & Figure A. 3), the high pH values limit the dissolution of all the primary minerals. Nevertheless, partial dissolution of the primary solid phases allows the release in solution of $SiO_{2(aq)}$, Al^{3+}, Ca^{2+}, Mg^{2+}, Na^{+} and K^{+}. As a result, their concentrations increase with depth (Figure 9). Moreover, these elements are lost ($\tau < 0$) along the weathering profile, except Al^{3+} (Figure 31). Aluminium is the only element which is almost immobile, because allophanes and gibbsite precipitate throughout the soil profile (Figure 10c, f). With time, primary solid phase dissolution continues (Figure 10 & Figure A. 1), leading to greater loss in $SiO_{2(aq)}$, Ca^{2+}, Mg^{2+}, Na^{+} and K^{+}. As weathering proceeds further, the contents of solid phases decrease and less $SiO_{2(aq)}$, Ca^{2+}, Mg^{2+}, Na^{+} and K^{+} are released in solution, and thus lower concentrations of these elements occur with time.

After 2 kyr of weathering, the soil column is more concentrated in Mg^{2+} below 80 cm. This is because pargasite has started to dissolve at this depth, whereas it did not in the shorter weathering simulations. Volcanic glass also contains Mg^{2+} but dissolves in constant manner at all depths. Magnesium is also present in phlogopite, but this latter does not dissolve at these depths. Calcium behaves like Mg^{2+}, except it originates from the dissolution of plagioclases and pargasite.

Free Al^{3+} is the only cation for which the concentration increases with time (Figure 9c). In theory, at pH > 4, Al^{3+} is not soluble and should precipitate. At alkaline pH values, the dominant Al species is $Al(OH)_4^-$ and as the pH decreases and approaches pH 7, the complex becomes less stable and dissolves to form more $Al(OH)_{3(aq)}$ and $Al(OH)_2^+$ (Harris et al., 1996). Indeed, the weathering profile gets 10 times less concentrated in $Al(OH)_4^-$ between 0.1 and 5 kyr at 1 m depth, whereas the concentration of $Al(OH)_{3(aq)}$ and $Al(OH)_2^+$ increases (Figure 29).

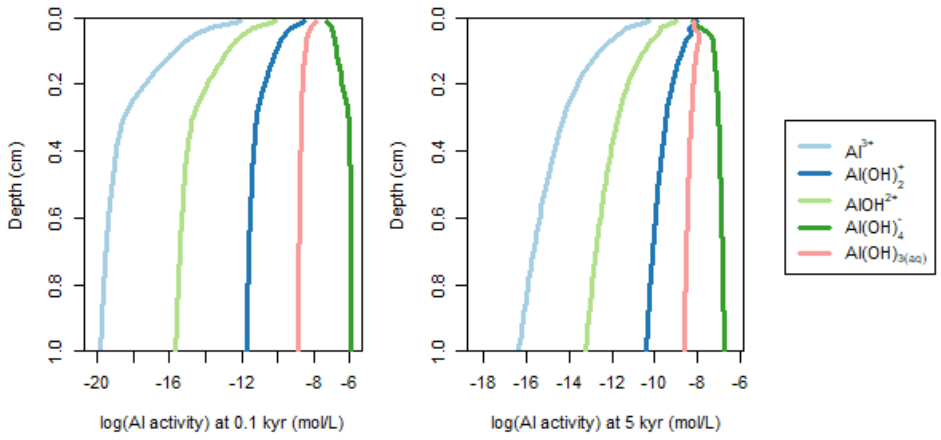

Figure 29. M1 model, free Al^{3+} and hydro-Al complexes concentration evolution at: (a) 0.1 kyr and (b) 5 kyr;

Volcanic glass, which is the predominant primary solid phase in the parent material, does not show a weathering front; it is always undersaturated (SI < 0; Figure 30b) and dissolves at all depths in the profile (Figure 10b). Thus, evolution of the mass-transfer coefficients τ of Ca, Si and Na (Figure 31) mainly follow the weathering front of plagioclases, which are the second most important primary solid phase.

When the concentrations of free Al^{3+} and/or $SiO_{2(aq)}$ in solution are sufficiently high, secondary solids may precipitate. In the weathering scenario M1, allophanes and gibbsite precipitation is predicted (Figure 10c, f). Halloysite is always undersaturated (Figure 30h) and does not precipitate (Figure 10d). Amorphous silica also does not precipitate (Figure 10e) probably due to a SI < 0 (Figure 30i) or a kinetic limitation when compared to allophanes (Figure A. 4i). The latter is the principal secondary solid phase precipitating in the weathering profile. Its formation fixes the concentration of Al^{3+} and $SiO_{2(aq)}$ in solution. During the first 0.8 kyr of weathering, the soil solution is slightly saturated (SI ≈ 10^{-2}-10^{-3}) with allophanes below 10 cm (Figure 30g) in all the simulations. Yet, allophanes do not precipitate below a certain depth (Figure 10c). This is due to kinetic limitations: the precipitation rate of the allophanes is zero (Figure A. 4g). Similar to Ca, Si and Na losses, allophanes precipitation mainly follows the weathering front of plagioclases.

When the soil solution is poorly concentrated in $SiO_{2(aq)}$ and rich in free Al^{3+}, gibbsite can precipitate (Figure 30f). Gibbsite precipitation occurs at the surface of the weathering profile after 2 kyr. In such conditions, the allophanes are undersaturated (Figure 30c) and thus, can start to dissolve at that moment.

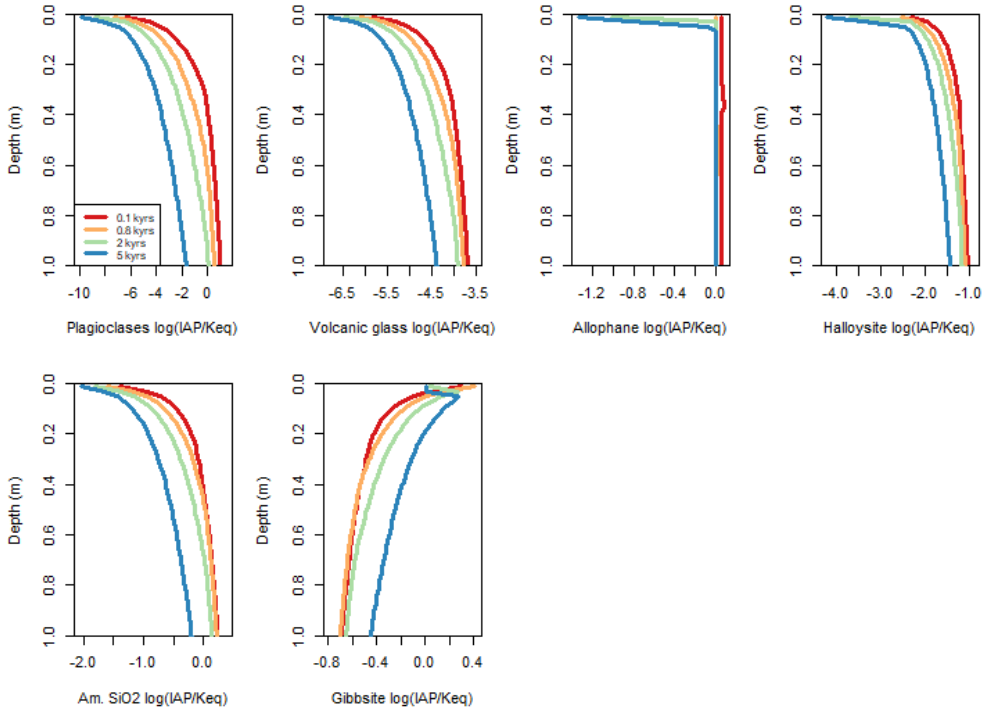

Figure 30. M1 base model's prediction of the saturation indexes (log IAP/Keq) of (a) plagioclases, (b) volcanic glass, (c) allophanes, (d) halloysite, (e) amorphous silica, and (f) gibbsite.

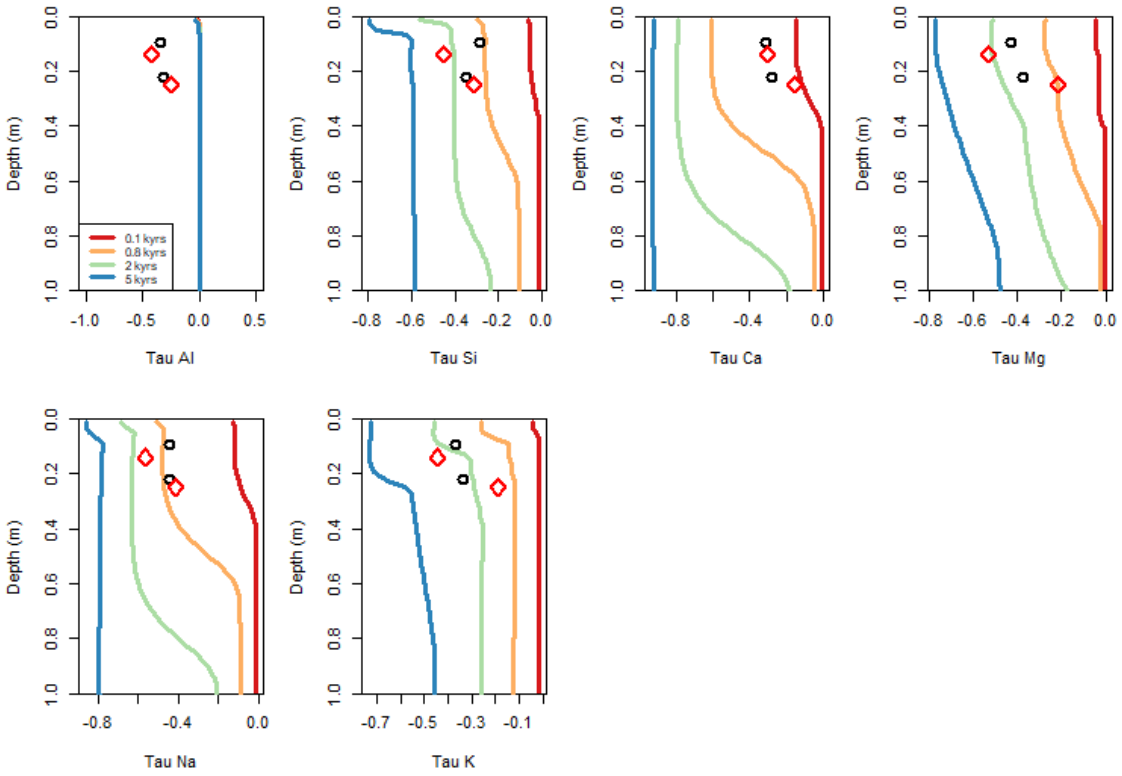

Figure 31. M1 base model's weathering profile predictions. Profiles of: (a) Al, (b) Si, (c) Ca, (d) Mg, (e) Na and (f) K. Same legend as for Figure 9.

5.2. Effect of soil respiration (M2)

The increase in CO_2 concentration by 10 and 100 times decreases the soil solution pH (Figure A. 5a & Figure 11a). The higher pCO_2 results in a greater formation of H_2CO_3 which releases more H^+ in solution when it dissociates into H^+ and HCO_3^-. Thus, it results in a higher soil solution pH. Although the simulated solution pH in M2 is closer to the field measurements (i.e. 6.3 for TU and 6.0 for CU at 20 cm depth) than the M1 prediction (pH = 8), the M2a model 0.8 kyr simulation is still unable to represent it adequately (pH = 7). The M2b produces soil solution pH values (6.1 at 20 cm) that are close to those measured in the field. A lower pH means more H^+ available for weathering, but not necessarily a higher dissolution rate. Indeed, except for volcanic glass, the rate laws of the solid phases are all linear and do not depend on H^+ concentration.

At a higher CO_2 concentration, the weathering fronts of the primary solid phases move downwards and their %v decrease more, both with depth and time (Figure 12, Figure A. 6, Figure A. 9). In the M2b model, annite and riebeckite are the only primary solid phases for which a weathering front still exists (Figure A. 9a, d). The tendency of plagioclases, pargasite, phlogopite and volcanic glass to dissolve all the way down in the weathering profile is reflected in the negative SI values predicted at all depths (Figure 32a, c, Figure A. 10b, c & Figure A. 7). The enhanced dissolution of the ash primary solid phases results in higher concentrations of dissolved Al^{3+}, $SiO_{2(aq)}$, Ca^{2+}, Mg^{2+}, Na^+ and K^+ (Figure 11 & Figure A. 5). However, compared to M1, the $SiO_{2(aq)}$ and cation concentrations decrease more rapidly since the primary solid phases

are consumed faster. This is also reflected in Figure 33 and Figure A. 8 which indicate lower mass-transfer coefficients in Si, Ca, Mg, Na and K, meaning that these elements are depleting more in the weathering profile. The model overestimates the loss in Ca compared to the reference τ_{Ca} by 40 %.

This M2 model predicts a certain mobility of Al in the profile. Indeed, in contrast to M1, a large loss in Al (τ_{Al}) is observed in the top of the weathering profile, immediately followed by a small gain (Figure 33a & Figure A. 8a). After 5 kyr of weathering, M2b predicts a loss of 85 % of Al in the first 5 cm, whereas a gain of 20 % is noticed in the next 4 cm. In the first 5 cm, the soil solution pH is < 5, hence Al^{3+} is soluble and is mobilised across the profile. Allophanes are undersaturated (with an SI value as low as -3.5; Figure 32c) and dissolve, therefore releasing Al^{3+} into solution. The soil allophanes content decreases and no allophanes are left in the first 5 cm of the weathering profile (Figure 12c). Once the pH > 5, Al^{3+} is no longer soluble and precipitates in allophanes. As a result, a spike in allophanes %v occurs at 8 cm depth. Below 8 cm, the $SiO_{2(aq)}$ concentration is very low (<10^{-4} mol/L) and the concentration of Al^{3+} is high enough (Figure 11b,c), which leads to the supersaturation of gibbsite (Figure 32f), which then starts precipitating (Figure 12j). As $SiO_{2(aq)}$ concentration increases in solution, allophanes become supersaturated (Figure 32c) and precipitate, whereas gibbsite dissolves.

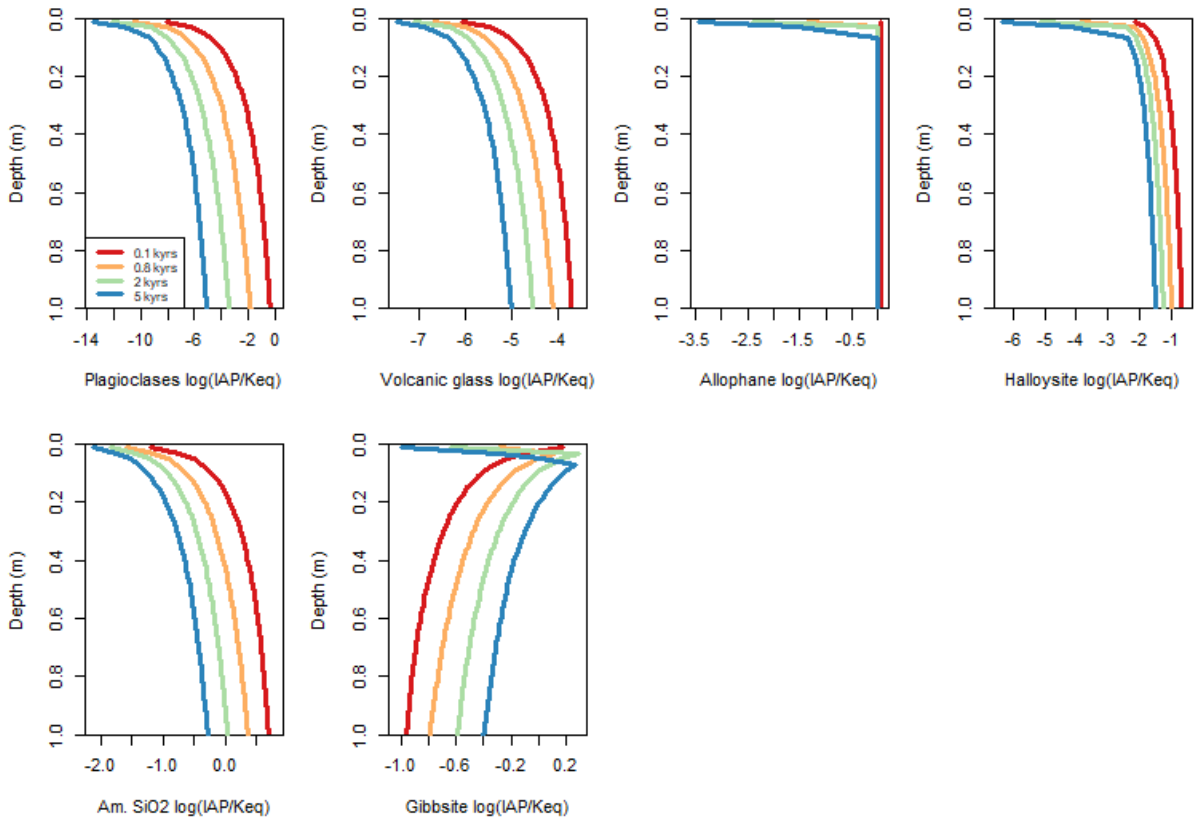

Figure 32. M2b model's prediction of the SI of (a) plagioclases, (b) volcanic glass, (c) allophanes, (d) halloysite, (e) amorphous silica, and (f) gibbsite.

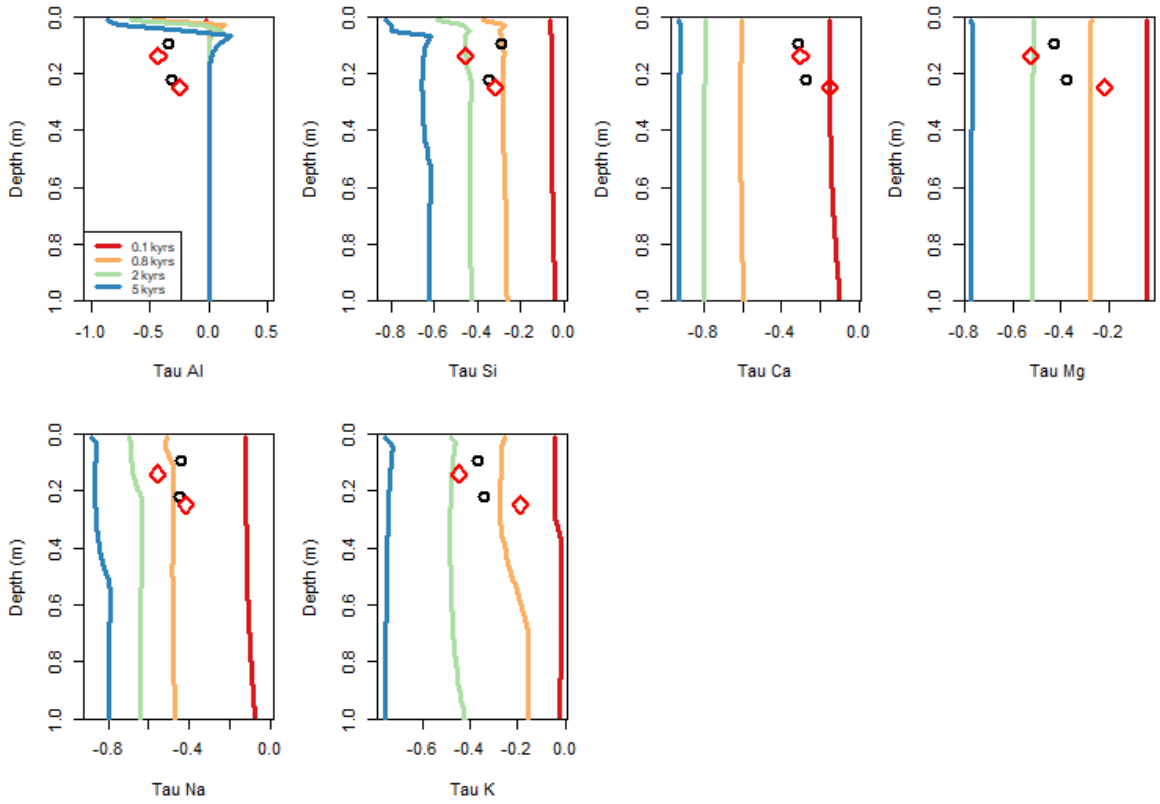

Figure 33. M2b model's mass-transfer coefficients τ predictions. Profiles of: (a) Al, (b) Si, (c) Ca, (d) Mg, (e) Na and (f) K. Same legend as for Figure 9.

5.3. Effects of organic acids in solution (M3)

At pH values < 5, organic acids are the dominant H^+ donor and H_2CO_3 (from dissolution of CO_2 gas) no longer contributes to the solution acidity. Thus, the use of a pCO_2 of 3 000 or 30 000 ppmv does not affect the solution, pH as it is dictated by the presence of dissolved organic acids.

5.3.1. Tussock-like grasses (M3TU)

The addition of oxalic acid to the solution at a concentration similar to that measured in the TU soil does not produce major differences (compared to the results obtained in the M2b model). This is because the pH remains the same as before the inclusion of the organic acid. Plagioclases, riebeckite, phlogopite and annite do not weather more in the presence of oxalic acid (Figure 14a & Figure A. 11). Their contents in the weathering profile and the dissolved $SiO_{2(aq)}$, Ca^{2+}, Mg^{2+}, Na^+ and K^+ concentrations stay the same (Figure 13). The interpretation proposed for explaining the spatial and temporal evolutions of these parameters in the M2b also applies to the M3TU results. The model continues to overestimate by 40 % the weathering profile losses in Ca, compared to the reference τ_{Ca} (Figure 35c). This might be due to additional contribution of Ca by external sources.

The main differences between the M2b and M3TU simulations relate to the concentration of free Al^{3+}, volcanic glass and allophanes contents and mineral saturation indices in the first 20

cm of the weathering profile. When pH is < 5 and organic acids are present, the anti-allophanic effect takes place and allophanes precipitation is inhibited (Delmelle et al., 2015). After 5 kyr of weathering, the soil solution of the first 10 cm of the profile has a pH < 5 (Figure 13a). At that pH, Al is mainly in the form of Al-oxalate, which is confirmed by the higher concentration of Al-oxalate in the profile (> 10^{-6} mol/L) (

Figure A. 12). Under the form of Al-oxalate, Al is soluble and is leached. This is reflected in the negative τ_{Al} value (loss in Al) inferred at this depth (Figure 35a). At this point in time, allophanes are highly undersaturated (Figure 34c) and thus, dissolve. Once the pH is > 5, there is no longer the anti-allophanic effect. The allophanes do not precipitate right away but only below 18 cm depth, as they are still undersaturated (SI < 0). This is because the $SiO_{2(aq)}$ concentration is too low (< 2 10^{-4} mol/L) (Figure 13b). After 5 kyr of weathering, no other secondary minerals precipitate between 10 and 18 cm depth, thus free Al^{3+} are not consumed and their concentration increases. Once the allophanes become supersaturated (SI > 0), they precipitate. This consumes free Al^{3+} and thus decreases free Al^{3+} concentration in solution. At these depths, Al-oxalate concentration also decreases in solution (

Figure A. 12). The precipitation of allophanes is also represented by the accumulation of Al (τ_{Al} > 0) and Si (its τ_{Si} increases) between 20 and 40 cm (Figure 35a&b).

In all the M3TU simulations, the content of volcanic glass in the first 15 cm of the profile is lower than in the rest of the profile (Figure 14b). This relates to the volcanic glass dissolution rate. During the first 2 kyr of weathering, the dissolution rate is enhanced (more negative) in the first 15 cm (Figure 36). According to the previously presented Equation 4, the dissolution rate of rhyolitic glass increases with acidity but decreases with Al^{3+} activity (or concentration). Thus, during the first 2 kyr, the low pH and free Al^{3+} concentration may be responsible for the increased volcanic glass dissolution kinetics. After 5 kyr of weathering, the dissolution rate is still higher (more negative) between the 4 and 15 cm depths compared to the lower part of the profile. However, a slower rate (less negative) is observed in the first 4 cm. We have not been able to infer a clear explanation for this trend; it could be due to numerical uncertainties of the model.

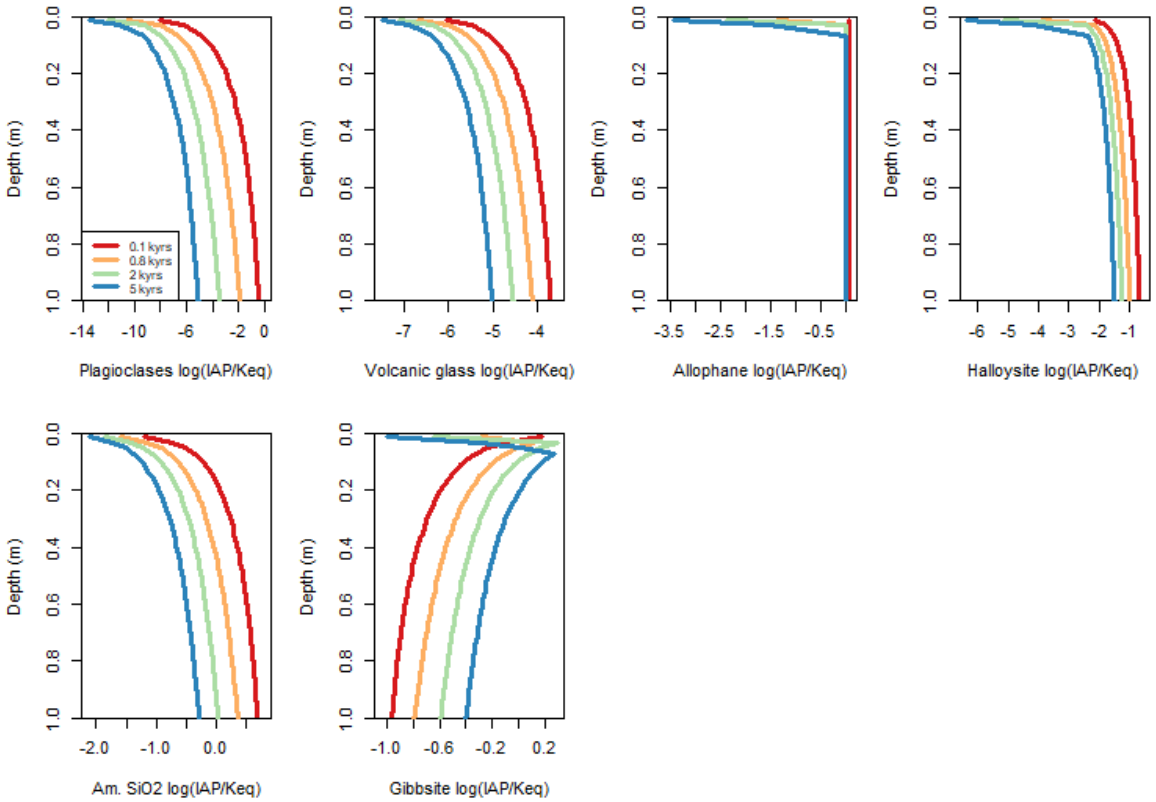

Figure 34. M3TU model's prediction of the SI of (a) plagioclases, (b) volcanic glass, (c) allophanes, (d) halloysite, (e) amorphous silica, and (f) gibbsite.

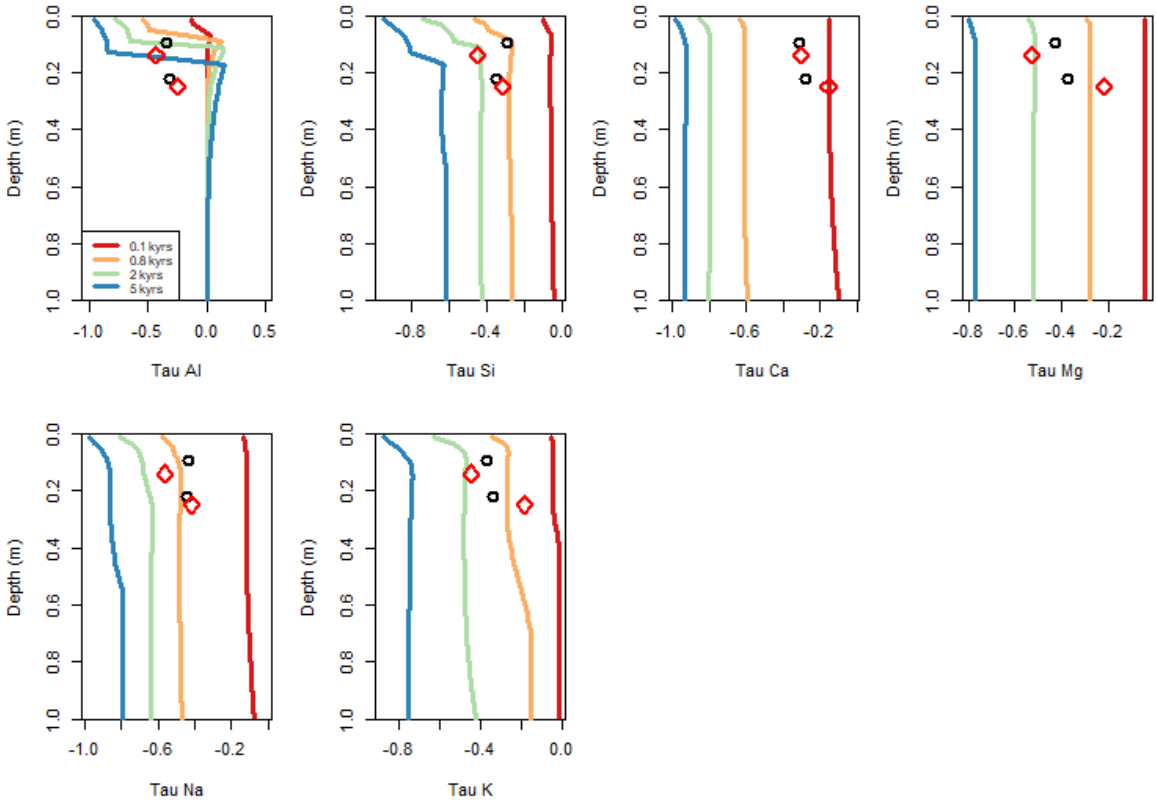

Figure 35. M3TU model's mass-transfer coefficients τ predictions. Profiles of: (a) Al, (b) Si, (c) Ca, (d) Mg, (e) Na and (f) K. Same legend as for Figure 9.

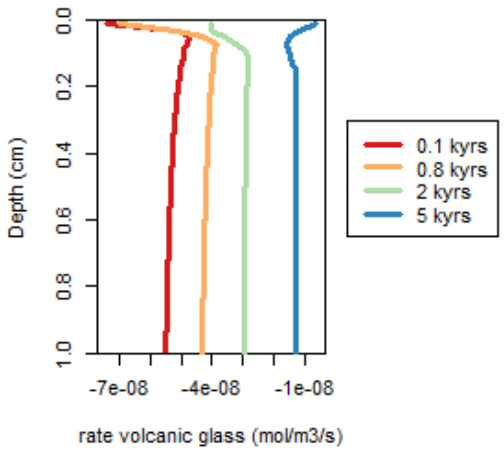

Figure 36. M3TU model's prediction of the dissolution rate of volcanic glass.

5.3.2. Cushion-forming plants (M3CU)

The addition of oxalic acid to the solution at a concentration similar to that measured in the CU soil affects the results significantly. This is largely due to the much lower pH values generated in the soil solution. After respectively 0.8 and 5 kyr of weathering, the soil solution in the first 20 and 50 cm of the weathering profile has a pH < 5 (Figure 15a). Thus, the free Al^{3+} concentration continues to increase down to these depths (Figure 15c). Since the low pH values occur across a larger part of the weathering profile compared to what was seen in M3TU, the concentration of Al-oxalate is also greater (10-100 times higher) (Figure A. 14) and more Al is leached (Figure 38a). After 5 kyr, the first 20 cm of the weathering profile are devoid (τ = -1) of Al, Si, Ca, Na and K (Figure 38). The effects of this low pH on the evolution of volcanic glass and allophanes are the same as for the M3TU model, but are more pronounced and are also observed deeper in the profile (Figure 16b, c). As for the M3TU model, halloysite, $SiO_{2(am)}$ and gibbsite are always undersaturated (Figure 37d, e, f) and never precipitate in M3CU (Figure 14d, e, f).

It is noteworthy that the solution pH modelled in M3CU shows a different evolution than in M3TU. The M3TU model's pH has one inflection point (Figure 13a), while the pH depth profile in M3CU shows two inflection points (Figure 15a). The first inflection point in M3CU is at pH ~4.1, which corresponds to the second pKa (pKa_2) of oxalic acid. When the pH < pKa_2, $HC_2O_4^-$ is the predominant form in solution and buffers the pH. When the pH > pKa_2, $C_2O_4^{2-}$ is dominant and more Al^{3+} can complex with it. The Al^{3+} concentration depends on the pH, which explains why the saturation curves of the solid phases follow the pH evolution (Figure 37). Amorphous silica is the only solid phase that does not contain Al and therefore, its SI is not affected by the changes in pH with depth.

The soil solution pH predicted by the M3CU model is very close (underestimation by only half a unit) to the pH measured in the field at 20 cm depth.

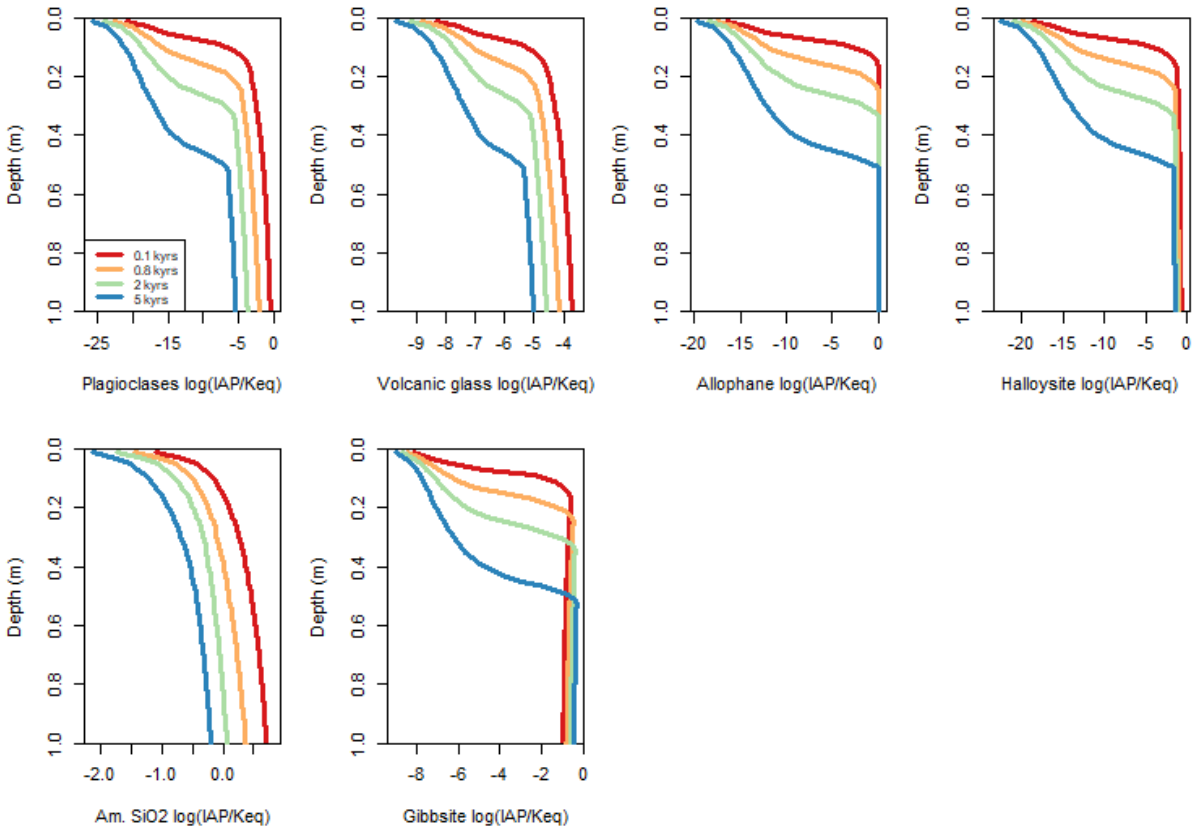

Figure 37. M3CU model's prediction of the SI of (a) plagioclases, (b) volcanic glass, (c) allophanes, (d) halloysite, (e) amorphous silica, and (f) gibbsite.

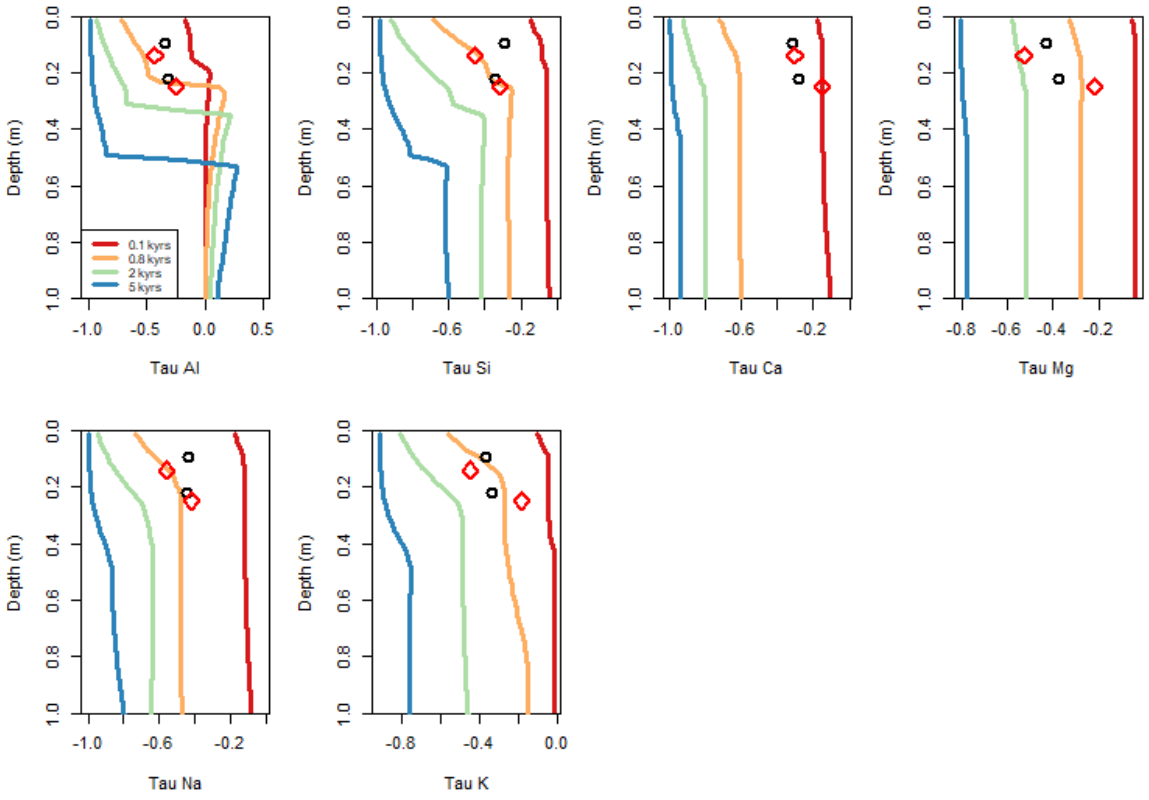

Figure 38. M3CU model's weathering profile predictions. Profiles of: (a) Al, (b) Si, (c) Ca, (d) Mg, (e) Na and (f) K. Same legend as for Figure 9.

5.4. Effects of changes in rainfall

5.4.1. Increased water infiltration (F2 & F3)

Both under TU and CU, a higher flow (0.6 and 0.8 m/yr, compared to the current 0.4 m/yr) leads to a lower pH soil solution. For TU, the decrease is always below 0.5 pH unit (Figure 19a & Figure 21a). Depending on the depth, the difference of the soil solution pH between M3CU and the increased flow models F2CU and F3CU varies from 0.5 to 1.5 units (Figure 25a & Figure 27a).

The plagioclases, pargasite and phlogopite weathering profiles are not influenced by the flow increase, whereas differences are noticed for volcanic glass, riebeckite and annite. These three solid phases weather more rapidly and their weathering front moves downwards as the rainwater flow increases (Figure 20b, Figure 22b, Figure 26b, Figure 28b, Figure A. 19a, d, Figure A. 23a, d, Figure A. 27a, d & Figure A. 30a, d). With a higher flow, more H^+ are added to the soil during a given period of time. As a result, more weathering can take place. Additionally, when the flow is increased, the cations that have been dissolved from the primary solid phases are removed faster. This tends to maintain undersaturated conditions in the soil solution (Figure 39, Figure 41, Figure A. 24 & Figure A. 31), which in turn drives more dissolution. Under CU, the more rapid removal of the cations released in solution, is reflected by the slightly lower τ values (Figure 42 & Figure A. 25). Under TU, except for Al and Si, no difference in the τ values for the cations is observed (Figure 40 & Figure A. 25). This may be due to the low proportion of annite and riebeckite in the weathering profile.

From our results, it appears that riebeckite only dissolves below a pH of ~5.5. This is why, as the water flow is increased (i.e. pH decreases) more riebeckite dissolves. The higher water flow enhances the volcanic glass dissolution in the first 25 and 70 cm under TU and CU, respectively. The results show that volcanic glass dissolution is enhanced at pH < 5 (i.e. when free Al^{3+} is soluble).

The plagioclases ($-20 < SI_{TU} < 0$ and $-25 < SI_{CU} < 0$), pargasite ($-100 < SI_{TU} < -20$ and $-120 < SI_{CU} < -20$) and phlogopite ($-40 < SI_{TU} < 0$ and $-50 < SI_{CU} < 0$) are already highly undersaturated in F2&F3TU (Figure 39, Figure A. 20 & Figure A. 28) and F2&F3CU (Figure 41, Figure A. 20 & Figure A. 24) and dissolve all the way down.

The $SiO_{2(aq)}$, Ca^{2+}, Mg^{2+}, Na^+ and K^+ concentrations decrease as the rainwater flow increases (Figure 19, Figure 21, Figure 25 & Figure 27). Volcanic glass, riebeckite and annite dissolve a bit more. However, as the flow is higher, these elements are less concentrated in the soil solution. The first 60 cm of the F3CU profile are less concentrated in free Al^{3+} than in M3CU, whereas the last 40 cm of the profile are more concentrated in free Al^{3+} than in M3CU. As the flow is increased, a greater part of the soil solution has a pH < 5 and is undersaturated with respect to allophanes. Thus, the precipitation of allophanes is inhibited and free Al^{3+} and Al-oxalates accumulate in that part of the profile (Figure A. 22 & Figure A. 26 & Figure A. 29 & Figure A. 32). This is reflected in the greater mobility of Al and Si in the weathering profile (Figure 40, Figure

42, Figure A. 21 & Figure A. 25). This is especially visible in the profile under CU. After 5 kyr of weathering, Al and Si leach in the first 80 cm of the profile in F3CU and only in the first 50 cm in M3CU. Allophanes begin to precipitate deeper in the profile when the pH is > 5 and SI > 0. Gibbsite and halloysite are not influenced by the rainwater flow and stay undersaturated. Amorphous silica is slightly oversaturated during the first 0.8 kyr of weathering but does not precipitate, as it is kinetically disadvantaged compared to the allophanes.

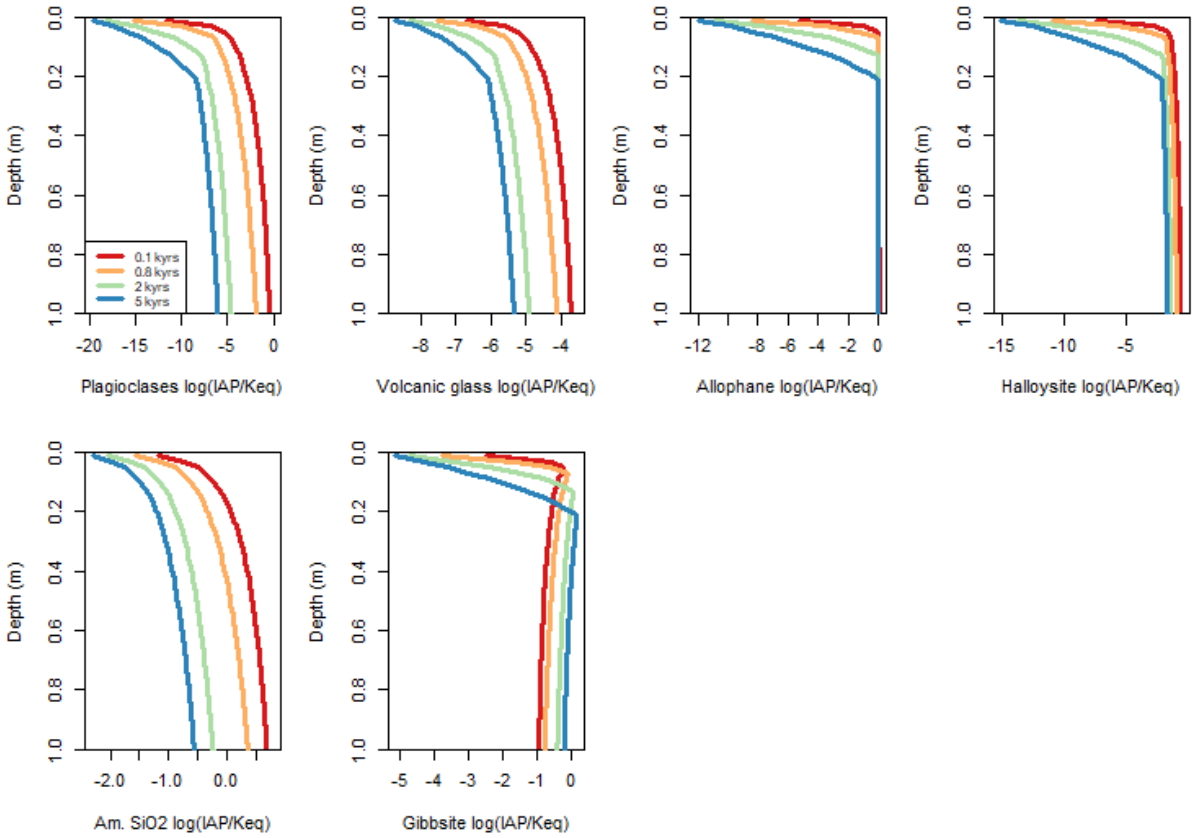

Figure 39. F3TU model's prediction of the SI of (a) plagioclases, (b) volcanic glass, (c) allophanes, (d) halloysite, (e) amorphous silica, and (f) gibbsite.

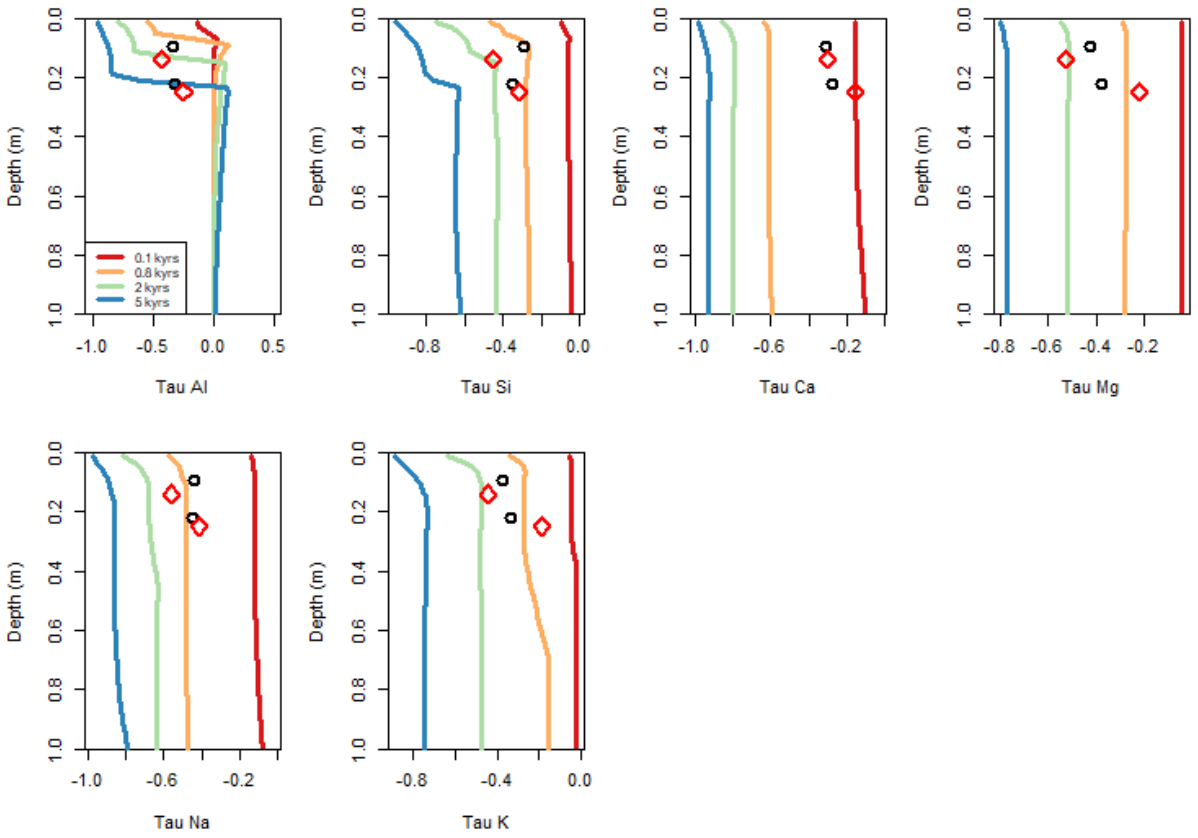

Figure 40. F3TU model's prediction of the mass-transfer coefficients of: (a) Al, (b) Si, (c) Ca, (d) Mg, (e) Na and (f) K.

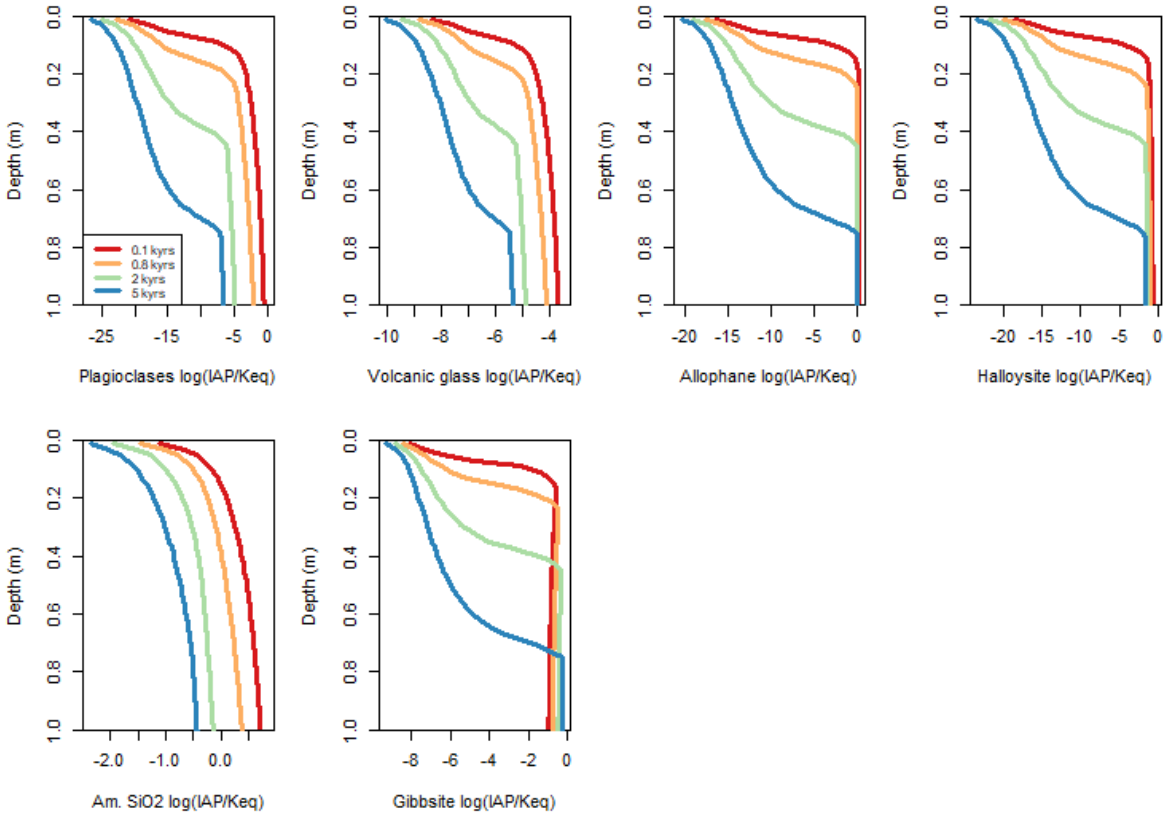

Figure 41. F3CU model's prediction of the SI of (a) plagioclases, (b) volcanic glass, (c) allophanes, (d) halloysite, (e) amorphous silica, and (f) gibbsite.

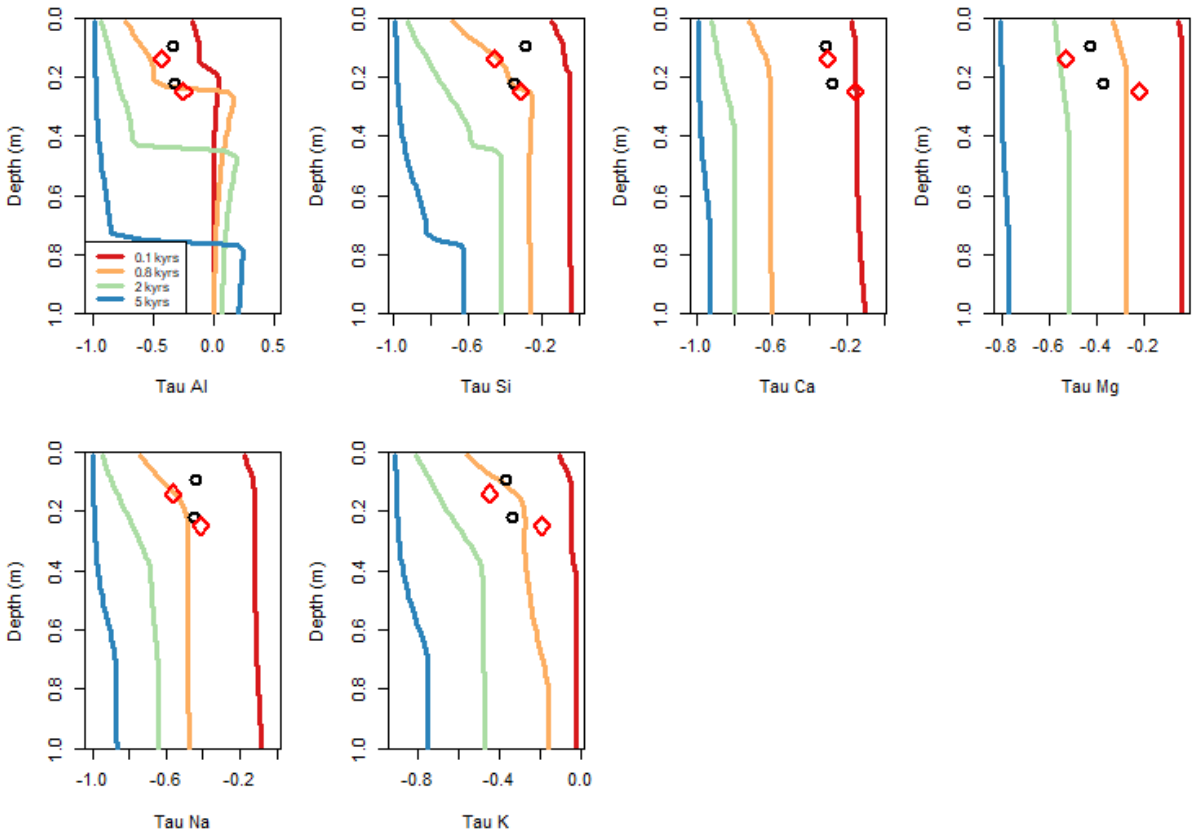

Figure 42. F3CU model's prediction of the mass-transfer coefficients of: (a) Al, (b) Si, (c) Ca, (d) Mg, (e) Na and (f) K.

5.4.2. Decreased water infiltration (F1)

With a lower flux (F1TU (Figure 23a) and F1CU (Figure 23a)), the soil solution pH is higher (~0.5 units at 1 m depth) compared to M3TU and M3CU, respectively. The lower rainwater flow means that less acidity is brought to the soil in a given time and the residence time in the soil is longer. This means that less H^+ are available for weathering and thus, less solid phases dissolve. This is reflected in the less negative mass transfer coefficients (**τ**) of the cations, i.e. the soil losses less cations (Figure 44 & Figure 46). Moreover, the lower flow eliminates more slowly the cations released by the dissolution of the primary solid phases. Hence, the primary solid phases are more saturated (Figure 43, Figure 45, Figure A. 16 & Figure A. 18). The weathering fronts of riebeckite, annite and volcanic glass move upwards. Similarly in the F2 and F3 models, plagioclases, pargasite and phlogopite are not influenced by the change in water flow. Although less weathering takes place, the residence time of water in the weathering profile is longer, as already mentioned, which concentrates more the ions in solution.

Some $SiO_{2(am)}$ precipitates (~2 %v) after 5 kyr of weathering in the last 20 cm of the profile in both F1TU and F1CU, whereas it never does in M3. At this depth, $SiO_{2(am)}$ is undersaturated in the 5 kyr simulation, whereas it is oversaturated during the first 2 kyr of weathering. Therefore, the content of $SiO_{2(am)}$ observed in the 5 kyr simulation is what is left from the precipitation that

took place before 5 kyr. Given that the pH gets > 5, at shallower depths when the water flow is decreased, the allophanes precipitate at higher depths.

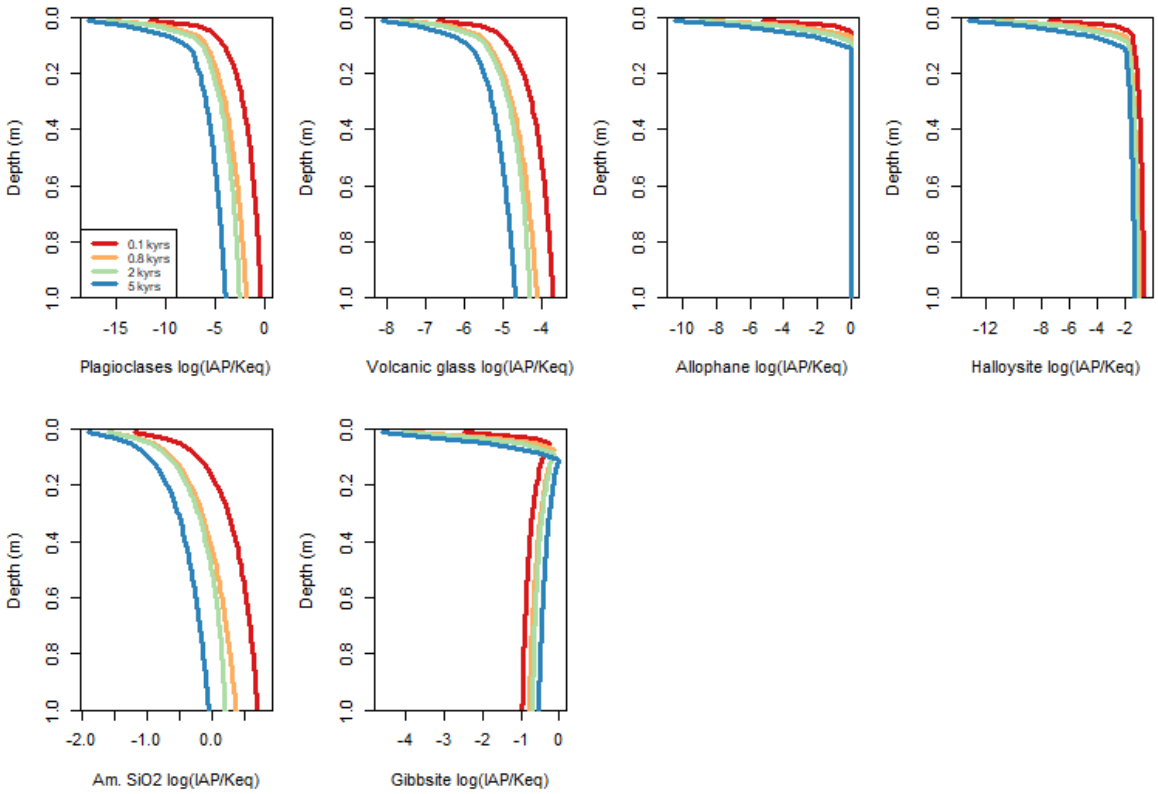

Figure 43. F1TU model's prediction of the SI of (a) plagioclases, (b) volcanic glass, (c) allophanes, (d) halloysite, (e) amorphous silica, and (f) gibbsite.

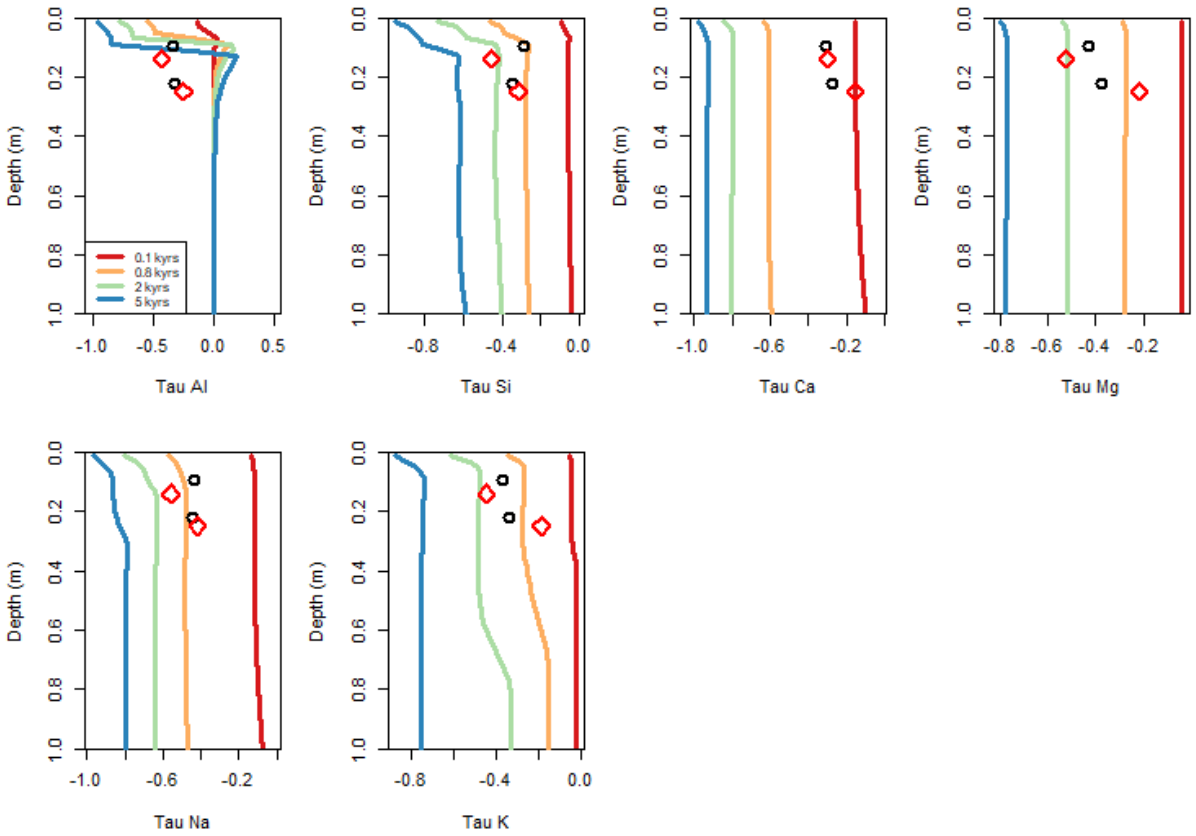

Figure 44. F1TU model's prediction of the mass-transfer coefficients τ of: (a) Al, (b) Si, (c) Ca, (d) Mg, (e) Na and (f) K.

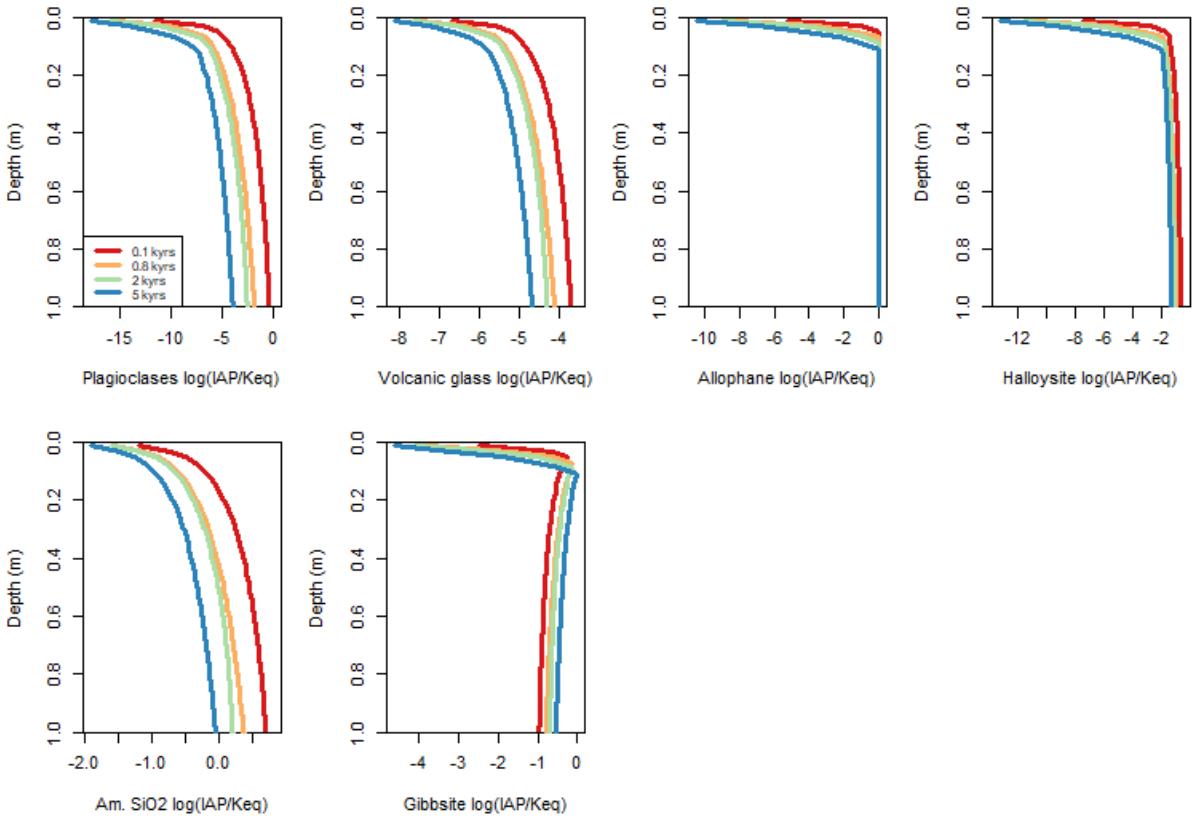

Figure 45. F1CU model's prediction of the SI of (a) plagioclases, (b) volcanic glass, (c) allophanes, (d) halloysite, (e) amorphous silica, and (f) gibbsite.

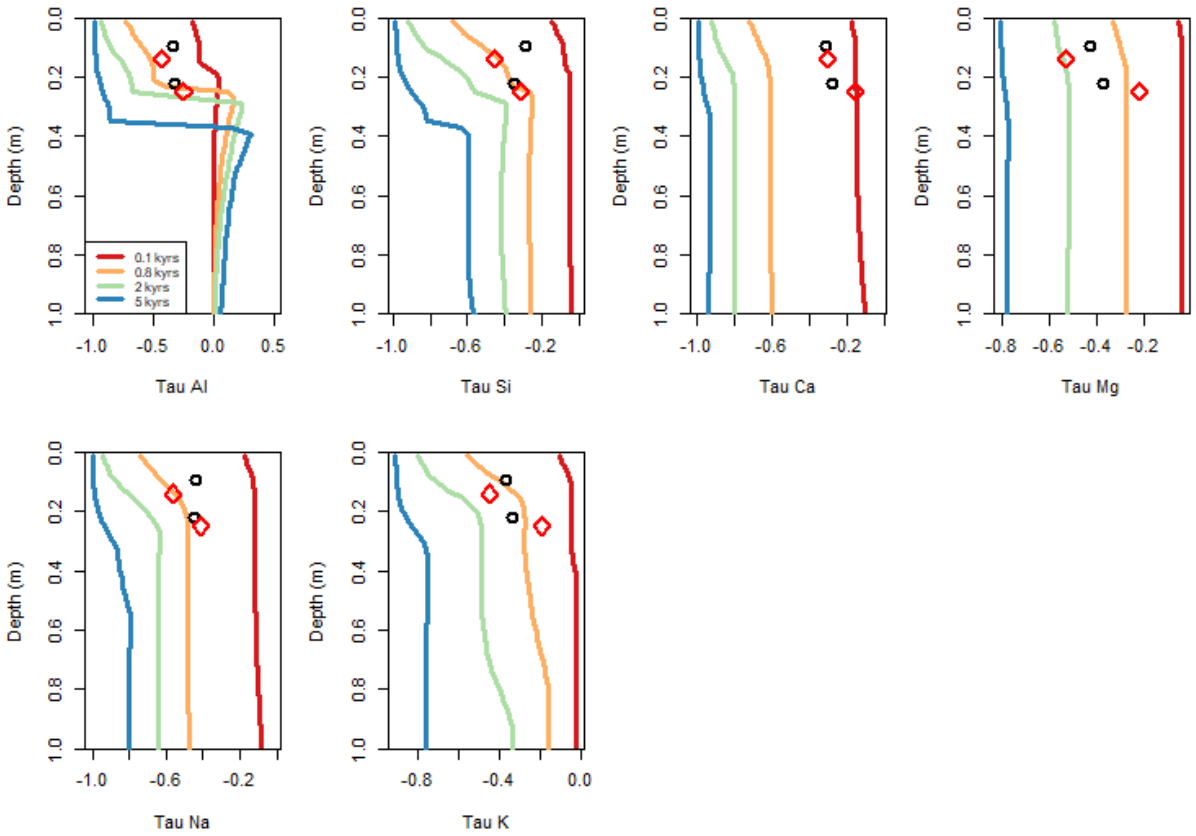

Figure 46. F1CU model's prediction of the mass-transfer coefficients τ of: (a) Al, (b) Si, (c) Ca, (d) Mg, (e) Na and (f) K.

5.5. Model limitations

Our modelling approach has several limitations. First, it is a one-dimension model with constant and steady state flow. In a real system, the water infiltration rate varies with time and there are preferential flow paths. This results in heterogeneous water residence time in the soil. This may influence the weathering profiles and dissolution/precipitation rates of the solid phases.

Second, our study is based on a restricted number of field data. Therefore, comparing the model predictions with the field measurements is difficult. In mountainous areas, precipitation has a high spatial variability and thus, the soil properties can vary a lot from places to places in the same paramo region. More field measurements would be needed to assess the robustness of the simulations.

Third, a point to improve in our study is the thermodynamic and kinetic descriptions of the allophanes. Allophanes are the main secondary solid phase precipitating in the models but no kinetics values are yet documented in the literature. Therefore, the $SiO_{2(am)}$ rate is used in the simulations. New experimental studies should be conducted in order to characterize better the rate law of allophanes precipitation/dissolution.

Finally, some uncertainties remain on the dependence of volcanic glass' dissolution rate on the affinity term. As long as far-from-equilibrium conditions are maintained in the weathering system being studied, affinity should not affect the rate of volcanic glass dissolution significantly.

However, problems with the geochemical simulations may emerge when equilibrium is approached. While the kinetics of the volcanic rate have been relatively well studied in laboratory experiments, the timescale (a few days) at which these investigations have been carried out does not provide the information necessary to assess the impact of the affinity on the dissolution rate over longer time scales (> 10 yr). New dissolution experiments lasting several years should be carried out to shed light on this potential issue.

Despite these limitations, and based on the few actual observations available so far, the M3 models have produced a rather realistic representation of the current Antisana páramo soil solid phase and solution, with extrapolation possible regarding impact of changes in vegetation coverage and rain quantities. It can be used to deepen the knowledge on the weathering processes and to study potential impacts of human interventions and climate change.

6. Conclusion & Future Perspectives

In this dissertation, we successfully developed an RTM to study the chemical weathering of an ash deposit in the Antisana páramo. Our results suggest that the effect of soil respiration on the concentration of CO_2 in the soil solution must be incorporated into the model in order to generate pH values that are comparable to those measured in the field. However, increasing only the partial pressure of CO_2 produces results that does not correctly represent the mobility of Al in the weathering profile. We showed that the addition of oxalic acid to the weathering solution improves the results significantly. Thus, two different models were created: one mimicking the concentration of DOC in the soil under TU and the other for the (higher) concentration found in soils under CU. The computer simulations confirmed that organic acids play a critical role in the pedogenesis of the volcanic soils from a silica-rich ash deposit. In particular, they showed that the formation of Al-oxalate complexes impedes the precipitation of allophanes, while enhancing the dissolution of volcanic glass due to lower concentrations of free Al^{3+} in solution.

The RTM algorithm predicts an increase in the soil solution pH with depth, which is traceable to acidity consumption by silicate weathering. Further mechanisms visible with the simulations, as follows. With time, the solution pH decreases as there are less and less primary silicate minerals available for neutralising the acid inputs. All the primary solid phases dissolve through time. Plagioclases, pargasite and phlogopite do not show a weathering front and dissolve all the way down, whereas riebeckite, annite and volcanic glass exhibit a weathering front. Concomitantly, the dissolved $SiO_{2(aq)}$, Ca^{2+}, Mg^{2+}, Na^{+}, and K^{+} concentrations increase with depth and decrease with time. Free Al^{3+} is the only species which decreases with depth and increases with time. Halloysite, $SiO_{2(am)}$ and gibbsite never precipitate in the system. Allophanes precipitate only after a certain depth in the profile, i.e. when the solution pH > 5.

The simulations enable us also to see consequences of changing parameters. Decreasing the infiltration (flow) rate of rainwater (less precipitation or more evapotranspiration due to higher external temperatures) into the weathering profile (in the presence of DOC) tends to generate higher soil solution pH values. Compared to the current situation, a soil under TU is slightly affected by this change, whereas the difference is more pronounced, particularly in the first 40 cm of the weathering profile for a soil under CU. A lower water infiltration rate limits the mobility of Al deeper in the profile. It also slows down the dissolution of the primary solid phases, which release less $SiO_{2(aq)}$, Al^{3+}, Ca^{2+}, Mg^{2+}, Na^{+}, and K^{+} into solution. Nevertheless, the dissolved Si and cation concentrations are higher in the soil solution. We also notice that allophanes precipitate at greater depths than in the model with a higher infiltration rate.

Our findings reveal that, one the contrary, when the water flow rate is increased (more precipitation), the pH of the soil solution decreases. Moreover, the primary solid phases dissolve more rapidly, thereby releasing more chemical elements in solution. The

concentrations of these elements decrease in the weathering solution as they are quickly flushed away. Allophanes begin to precipitate deeper in the weathering profile and are the major secondary solid phases that form.

However, our study has some limitations. An important one is the restricted amount of field data that can be used to confront the model results. Thus, future work should aim at collecting additional field measurements of pH, Al^{3+}, $SiO_{2(aq)}$, Ca^{2+}, Mg^{2+}, Na^{+} and K^{+} concentrations in the soil solution. A robust determination of the water infiltration rate is also required in order to better calibrate the model. Given the important impact of organic acids, a wider range of concentrations should be tested. Further investigations should also be carried out by including citric acid in addition to oxalic acid, as it is commonly present in soils and can also form complexes with Al and Fe.

Future studies should examine the effect of increasing temperature – due to global warming – on the soil physicochemical properties. Indeed, higher temperatures could speed up the decomposition process of OM, thereby increasing even more DOC. Finally, the tangible impact of the ecosystem should be studied, in particular the evolution of water quality and availability, using the predictions made on the soil solution and soil mineralogy, as many populations depend on it.

Nevertheless, this study is a convincing first step towards enhancing our understanding of the páramo soils and the impacts of climate change-related precipitation variations thanks to modelling. We hope our RTM research will serve also as a basis for future studies on other tropical Andean regions.

7. Bibliography

Agrawal, P., Raoof, A., Iliev, O., Koskamp, J., Wolthers, M., 2017. Reactive transport modeling in carbonate rocks: Single pore model 7.

Anderson, E.P., Marengo, J., Villalba, R., Halloy, S., Young, B., Cordero, D., Gast, F., Jaimes, E., Ruiz, D., 2011. Consequences of Climate Change for Ecosystems and Ecosystem Services in the Tropical Andes, in: Herzog, S.K., Martínez, R., Jørgensen, P.M., Tiessen, H. (Eds.), Climate Change and Biodiversity in the Tropical Andes. Unpublished, pp. 1–18. https://doi.org/10.13140/2.1.3718.4969

Anderson, S.P., Dietrich, W.E., Jr, G.H.B., 2002. Weathering profiles, mass-balance analysis, and rates of solute loss: Linkages between weathering and erosion in a small, steep catchment. Geological Society of America Bulletin 114, 1143–1158.

Antos, J.A., Zobel, D.B., 2005. Plant Responses in Forests of the Tephra-Fall Zone, in: Dale, V.H., Swanson, F.J., Crisafulli, C.M. (Eds.), Ecological Responses to the 1980 Eruption of Mount St. Helens. Springer, New York, NY, pp. 47–58. https://doi.org/10.1007/0-387-28150-9_4

Aradóttir, E.S.P., Sonnenthal, E.L., Jónsson, H., 2012. Development and evaluation of a thermodynamic dataset for phases of interest in CO2 mineral sequestration in basaltic rocks. Chemical Geology 304–305, 26–38. https://doi.org/10.1016/j.chemgeo.2012.01.031

Bao, C., Wu, H., Li, L., Newcomer, D., Long, P.E., Williams, K.H., 2014. Uranium Bioreduction Rates across Scales: Biogeochemical Hot Moments and Hot Spots during a Biostimulation Experiment at Rifle, Colorado. Environ. Sci. Technol. 48, 10116–10127. https://doi.org/10.1021/es501060d

Beltrán, K., Salgado, S., Cuesta, F., León-Yánez, S., Romoleroux, K., Ortiz, E., Cárdenas, A., Velástegui, A., 2009. Distribución espacial, sistemas ecológicos y caracterización florística de los páramos en el Ecuador. EcoCiencia, Proyecto Páramo Andino y Herbario QCA. Quito.

Benavides, I.F., Solarte, M.E., Pabón, V., Ordoñez, A., Beltrán, E., Rosero, S., Torres, C., 2018. The variation of infiltration rates and physical-chemical soil properties across a land cover and land use gradient in a Paramo of southwestern Colombia. Journal of Soil and Water Conservation 73, 400–410. https://doi.org/10.2489/jswc.73.4.400

Biass, S., Bonadonna, C., Connor, L., Connor, C., 2016. TephraProb: a Matlab package for probabilistic hazard assessments of tephra fallout. Journal of Applied Volcanology 5, 16. https://doi.org/10.1186/s13617-016-0050-5

Blanc, Ph., Lassin, A., Piantone, P., Azaroual, M., Jacquemet, N., Fabbri, A., Gaucher, E.C., 2012. Thermoddem: A geochemical database focused on low temperature water/rock interactions and waste materials. Applied Geochemistry 27, 2107–2116. https://doi.org/10.1016/j.apgeochem.2012.06.002

Bradley, R.S., 2006. Climate change. Threats to Water Supplies in the Tropical Andes. Science 312, 1755–1756. https://doi.org/10.1126/science.1128087

Brunet, J.-P.L., Li, L., Karpyn, Z.T., Kutchko, B.G., Strazisar, B., Bromhal, G., 2013. Dynamic Evolution of Cement Composition and Transport Properties under Conditions Relevant to Geological Carbon Sequestration. Energy & Fuels 27, 4208–4220. https://doi.org/10.1021/ef302023v

Buytaert, W., Célleri, R., De Bièvre, B., Cisneros, F., Wyseure, G., Deckers, J., Hofstede, R., 2006a. Human impact on the hydrology of the Andean páramos. Earth-Science Reviews 79, 53–72. https://doi.org/10.1016/j.earscirev.2006.06.002

Buytaert, W., Cuesta-Camacho, F., Tobón, C., 2011. Potential impacts of climate change on the environmental services of humid tropical alpine regions: Climate change and environmental services. Global Ecology and Biogeography 20, 19–33. https://doi.org/10.1111/j.1466-8238.2010.00585.x

Buytaert, W., De Bièvre, B., 2012. Water for cities: The impact of climate change and demographic growth in the tropical Andes. Water Resour. Res. 48. https://doi.org/10.1029/2011WR011755

Buytaert, W., Deckers, J., Wyseure, G., 2006b. Description and classification of nonallophanic Andosols in south Ecuadorian alpine grasslands (páramo). Geomorphology 73, 207–221. https://doi.org/10.1016/j.geomorph.2005.06.012

Buytaert, W., Sevink, J., Cuesta, F., 2014. Cambio climático: la nueva amenaza para los páramos, in: Cuesta, F., Sevink, J., Llambí, L., De Bièvre, B., Posner, J. (Eds.), Avances en investigación para la conservación de los páramos andinos, CONDENSAN. pp. 506–526.

Buytaert, W., Sevink, J., De Leeuw, B., Deckers, J., 2005. Clay mineralogy of the soils in the south Ecuadorian páramo region. Geoderma 127, 114–129. https://doi.org/10.1016/j.geoderma.2004.11.021

Cailleteau, C., Angeli, F., Devreux, F., Gin, S., Jestin, J., Jollivet, P., Spalla, O., 2008. Insight into silicate-glass corrosion mechanisms. Nature Mater 7, 978–983. https://doi.org/10.1038/nmat2301

Carrillo-Rojas, G., Silva, B., Rollenbeck, R., Célleri, R., Bendix, J., 2019. The breathing of the Andean highlands: Net ecosystem exchange and evapotranspiration over the páramo of southern Ecuador. Agricultural and Forest Meteorology 265, 30–47. https://doi.org/10.1016/j.agrformet.2018.11.006

Célleri, R., Feyen, J., 2009. The Hydrology of Tropical Andean Ecosystems: Importance, Knowledge Status, and Perspectives. Mountain Research and Development 29, 350–355. https://doi.org/10.1659/mrd.00007

Chapman, B.M., 1982. Numerical simulation of the transport and speciation of nonconservative chemical reactants in rivers. Water Resour. Res. 18, 155–167. https://doi.org/10.1029/WR018i001p00155

Christmann, T., Oliveras, I., 2020. Nature of Alpine Ecosystems in Tropical Mountains of South America, in: Encyclopedia of the World's Biomes. Elsevier, pp. 282–291. https://doi.org/10.1016/B978-0-12-409548-9.12481-9

Correa, A., Ochoa-Tocachi, B.F., Birkel, C., Ochoa-Sánchez, A., Zogheib, C., Tovar, C., Buytaert, W., 2020. A concerted research effort to advance the hydrological understanding of tropical páramos. Hydrological Processes 1–18. https://doi.org/10.1002/hyp.13904

Crespo, P., Célleri, R., Buytaert, W., Feyen, J., Iñiguez, V., Borja, P., Bievre, B.D., 2010. Land use change impacts on the hydrology of wet Andean páramo ecosystems. Status and perspectives of hydrology in small basins 336, 71–76. https://doi.org/10.13140/2.1.5137.6320

Dahlgren, R.A., Saigusa, M., Ugolini, F.C., 2004. The Nature, Properties and Management of Volcanic Soils, in: Advances in Agronomy. Elsevier, pp. 113–182. https://doi.org/10.1016/S0065-2113(03)82003-5

Declercq, J., Diedrich, T., Perrot, M., Gislason, S.R., Oelkers, E.H., 2013. Experimental determination of rhyolitic glass dissolution rates at 40–200°C and 2<pH<10.1. Geochimica et Cosmochimica Acta 100, 251–263. https://doi.org/10.1016/j.gca.2012.10.006

Delmelle, P., Opfergelt, S., Cornelis, J.-T., 2015. Volcanic Soils, in: The Encyclopedia of Volcanoes. Elsevier, pp. 1253–1264. https://doi.org/10.1016/B978-0-12-385938-9.00072-9

Dontsova, K., Steefel, C.I., Desilets, S., Thompson, A., Chorover, J., 2009. Solid phase evolution in the Biosphere 2 hillslope experiment as predicted by modeling of hydrologic and geochemical fluxes. Hydrol. Earth Syst. Sci. 13, 2273–2286. https://doi.org/10.5194/hess-13-2273-2009

Fang, Y., Yabusaki, S.B., Morrison, S.J., Amonette, J.P., Long, P.E., 2009. Multicomponent reactive transport modeling of uranium bioremediation field experiments. Geochimica et Cosmochimica Acta 73, 6029–6051.

Farley, K.A., Kelly, E.F., Hofstede, R.G.M., 2004. Soil Organic Carbon and Water Retention after Conversion of Grasslands to Pine Plantations in the Ecuadorian Andes. Ecosystems 7, 729–739. https://doi.org/10.1007/s10021-004-0047-5

Feng, X., 1993. Surface Layer Effects on Waste Glass Corrosion. MRS Proc. 333, 55. https://doi.org/10.1557/PROC-333-55

Flores-López, F., Galaitsi, S., Escobar, M., Purkey, D., 2016. Modeling of Andean Páramo Ecosystems' Hydrological Response to Environmental Change. Water 8, 94. https://doi.org/10.3390/w8030094

Gin, S., Neill, L., Fournier, M., Frugier, P., Ducasse, T., Tribet, M., Abdelouas, A., Parruzot, B., Neeway, J., Wall, N., 2016. The controversial role of inter-diffusion in glass alteration. Chemical Geology 440, 115–123. https://doi.org/10.1016/j.chemgeo.2016.07.014

Gislason, S.R., Oelkers, E.H., Eiriksdottir, E.S., Kardjilov, M.I., Gisladottir, G., Sigfusson, B., Snorrason, A., Elefsen, S., Hardardottir, J., Torssander, P., Oskarsson, N., 2009. Direct evidence of the feedback between climate and weathering. Earth and Planetary Science Letters 277, 213–222. https://doi.org/10.1016/j.epsl.2008.10.018

Gunnarsson, I., Arnórsson, S., 2000. Amorphous silica solubility and the thermodynamic properties of H4SiO°4 in the range of 0° to 350°C at Psat. Geochimica et Cosmochimica Acta 64, 2295–2307. https://doi.org/10.1016/S0016-7037(99)00426-3

Gutiérrez-Salazar, P., Medrano-Vizcaíno, P., 2019. The effects of climate change on decomposition processes in Andean paramo ecosystem-synthesis, a systematic review. Appl. Ecol. Env. Res. 17, 4957–4970. https://doi.org/10.15666/aeer/1702_49574970

Harden, C.P., 2006. Human impacts on headwater fluvial systems in the northern and central Andes. Geomorphology 79, 249–263. https://doi.org/10.1016/j.geomorph.2006.06.021

Harris, W.R., Berthon, G., Day, J.P., Exley, C., Flaten, T.P., Forbed, W.F., Kiss, T., Orvig, C., Zatta, P.F., 1996. Speciation of aluminium in biological systems. Journal of Toxicology and Environmental Health 48, 543–568.

Haylock, M.R., Peterson, T.C., Alves, L.M., Ambrizzi, T., Anunciação, Y.M.T., Baez, J., Barros, V.R., Berlato, M.A., Bidegain, M., Coronel, G., Corradi, V., Garcia, V.J., Grimm, A.M., Karoly, D., Marengo, J.A., Marino, M.B., Moncunill, D.F., Nechet, D., Quintana, J., Rebello, E., Rusticucci, M., Santos, J.L., Trebejo, I., Vincent, L.A., 2006. Trends in Total and Extreme South American Rainfall in 1960–2000 and Links with Sea Surface Temperature. Journal of Climate 19, 1490–1512. https://doi.org/10.1175/JCLI3695.1

Heidari, P., Li, L., Jin, L., Williams, J.Z., Brantley, S.L., 2017. A reactive transport model for Marcellus shale weathering. Geochimica et Cosmochimica Acta 217, 421–440. https://doi.org/10.1016/j.gca.2017.08.011

Herzog, S.K., Martínez, R., Jørgensen, P.M., Tiessen, H. (Eds.), 2011. Climate Change and Biodiversity in the Tropical Andes. Inter-American Institute for Global Change Research (IAI) and Scientific Committee on Problems of the Environment (SCOPE).

Hofstede, R., Calles, J., López, V., Polanco, R., Torres, F., Ulloa, J., Vásquez, A., Cerra, M., 2014. Los Páramos Andinos ¿Qué sabemos? Estado de conocimiento sobre el impacto del cambio climático en el ecosistema páramo. UICN, Quito, Ecuador.

Hribljan, J.A., Suárez, E., Heckman, K.A., Lilleskov, E.A., Chimner, R.A., 2016. Peatland carbon stocks and accumulation rates in the Ecuadorian páramo. Wetlands Ecol Manage 24, 113–127. https://doi.org/10.1007/s11273-016-9482-2

IPCC, 2014. Climate change 2014: Impacts, Adaptation, and Vulnerability. Part B: Regional Aspects. Contribution of Working Group II to the Fifth Assessment Report of the Intergovernmental Panel on Climate Change. Barros, V.R., C.B. Field, D.J. Dokken, M.D. Mastrandrea, K.J. Mach, T.E. Bilir, M. Chatterjee, K.L. Ebi, Y.O. Estrada, R.C. Genova, B. Girma, E.S. Kissel, A.N. Levy, S. MacCracken, P.R. Mastrandrea, and L.L.White (eds.). Cambridge University Press, Cambrige, United Kingdom and New York, NY, USA.

ISSS Working Group RB, 1998. World Reference Base for Soil Resources: Introduction (J.A. Deckers, F.O. Nachtergaele and O.C. Spaargaren, Eds). First Edition. International Society of Soil Science (ISSS), International Soil Reference and Information Centre (ISRIC) and Food and Agriculture Organization of the United Nations (FAO). Acco. Leuven.

IUSS Working Group, 2015. World reference base for soil resources 2014, update 2015. International soil classification system for naming soils and creating legends for soil maps, World Soil Resources Reports. FAO, Rome.

Lasaga, A.C., 1984. Chemical Kinetics of Water-Rock Interactions. J. Geophys. Res. 89, 4009–4025. https://doi.org/10.1029/JB089iB06p04009

Ma, T., Jivkov, A.P., Li, W., Liang, W., Wang, Y., Xu, H., Han, X., 2017. A mechanistic model for long-term nuclear waste glass dissolution integrating chemical affinity and interfacial diffusion barrier. Journal of Nuclear Materials 486, 70–85. https://doi.org/10.1016/j.jnucmat.2017.01.001

Madriñán, S., Cortés, A.J., Richardson, J.E., 2013. Páramo is the world's fastest evolving and coolest biodiversity hotspot. Front. Genet. 4. https://doi.org/10.3389/fgene.2013.00192

Maher, K., Mayer, K.U., 2019a. The Art of Reactive Transport Model Building. Elements 15, 117–118. https://doi.org/10.2138/gselements.15.2.117

Maher, K., Mayer, K.U., 2019b. Tracking Diverse Minerals, Hungry Organisms, and Dangerous Contaminants Using Reactive Transport Models. Elements 15, 81–86. https://doi.org/10.2138/gselements.15.2.81

Mayer, K.U., Frind, E.O., Blowes, D.W., 2002. Multicomponent reactive transport modeling in variably saturated porous media using a generalized formulation for kinetically controlled reactions. Water Resour. Res. 38, 13-1-13–21. https://doi.org/10.1029/2001WR000862

Molina, A., Vanacker, V., Corre, M.D., Veldkamp, E., 2019. Patterns in Soil Chemical Weathering Related to Topographic Gradients and Vegetation Structure in a High Andean Tropical Ecosystem. J. Geophys. Res. Earth Surf. 124, 666–685. https://doi.org/10.1029/2018JF004856

Moore, J., Lichtner, P.C., White, A.F., Brantley, S.L., 2012. Using a reactive transport model to elucidate differences between laboratory and field dissolution rates in regolith. Geochimica et Cosmochimica Acta 93, 235–261. https://doi.org/10.1016/j.gca.2012.03.021

Morales, M., Otero, J., Van der Hammen, T., Torres, A., Cadena, C., Pedraza, C., Rodríguez, N., Franco, C., Betancourth, J.C., Olaya, E., Posada, E., Cárdenas, L., 2007. Atlas de páramos de Colombia. Instituto de Investigación de Recursos Biológicos Alexander von Humboldt, Bogotá, D. C.

Morrey, J.R., Krupka, K.M., Dove, F.H., 1985. MINTEQ2 Geochemical Code: Provisionary Organic Data Base (No. PNL-5609, 6415928). United States. https://doi.org/10.2172/6415928

Nanzyo, M., 2002. Unique Properties of Volcanic Ash Soils 14.

Navarre-Sitchler, A., Steefel, C.I., Sak, P.B., Brantley, S.L., 2011. A reactive-transport model for weathering rind formation on basalt. Geochimica et Cosmochimica Acta 75, 7644–7667. https://doi.org/10.1016/j.gca.2011.09.033

Neall, V.E., 2009. Volcanic soils, in: Verheye, W.H. (Ed.), Land Use, Land Cover and Soil Sciences. pp. 23–45.

Ochoa-Tocachi, B.F., Buytaert, W., De Bièvre, B., Célleri, R., Crespo, P., Villacís, M., Llerena, C.A., Acosta, L., Villazón, M., Guallpa, M., Gil-Ríos, J., Fuentes, P., Olaya, D., Viñas, P., Rojas, G., Arias, S., 2016. Impacts of land use on the hydrological response of tropical Andean catchments. Hydrol. Process. 30, 4074–4089. https://doi.org/10.1002/hyp.10980

Palandri, J.L., Kharaka, Y.K., 2004. A compilation of rate parameters of water-mineral interaction kinetics for application to geochemical modeling (U.S. Geological Survey. Open-File Report No. 1068), Open-File Report. Menlo Park, California.

Parfitt, R.L., 2009. Allophane and imogolite: role in soil biogeochemical processes. Clay miner. 44, 135–155. https://doi.org/10.1180/claymin.2009.044.1.135

Parfitt, R.L., Wilson, L.H., 1985. Estimation of allophane and halloysite in three sequences of volcanic soils, New Zealand, in: Volcanic Soils: Weathering and Landscape Relationships on Soils on Tephra and Basalt, Catena Supplement. Presented at the Congreso internacional de suelos volcanicos, pp. 1–8.

Parkhurst, D.L., Appelo, C.A.J., 1999. User's guide to PHREEQC (Version 2) : a computer program for speciation, batch-reaction, one-dimensional transport, and inverse geochemical

calculations (Water-Resources Investigations No. 99–4259). Denver, Colorado. https://doi.org/10.3133/wri994259

Paul, A., 1977. Chemical durability of glasses; a thermodynamic approach. J Mater Sci 12, 2246–2268. https://doi.org/10.1007/BF00552247

Perez-Fodich, A., Derry, L.A., 2019. Organic acids and high soil CO2 drive intense chemical weathering of Hawaiian basalts: Insights from reactive transport models. Geochimica et Cosmochimica Acta 249, 173–198. https://doi.org/10.1016/j.gca.2019.01.027

Podwojewski, P., Poulenard, J., 2004. Paramos Soils. Encyclopedia of Soil Science 4.

Podwojewski, P., Poulenard, J., Zambrana, T., Hofstede, R., 2002. Overgrazing effects on vegetation cover and properties of volcanic ash soil in the páramo of Llangahua and La Esperanza (Tungurahua, Ecuador). Soil Use and Management 18, 45–55. https://doi.org/10.1111/j.1475-2743.2002.tb00049.x

Poulenard, J., Podwojewski, P., Janeau, J.-L., Collinet, J., 2001. Runoff and soil erosion under rainfall simulation of Andisols from the Ecuadorian Páramo: effect of tillage and burning. Catena 45, 185–207. https://doi.org/10.1016/S0341-8162(01)00148-5

Renella, G., Landi, L., Nannipieri, P., 2004. Degradation of low molecular weight organic acids complexed with heavy metals in soil. Geoderma 122, 311–315. https://doi.org/10.1016/j.geoderma.2004.01.018

Rosi, M., Landi, P., Polacci, M., Di Muro, A., Zandomeneghi, D., 2004. Role of conduit shear on ascent of the crystal-rich magma feeding the 800-year-B.P. Plinian eruption of Quilotoa Volcano (Ecuador). Bull Volcanol 66, 307–321. https://doi.org/10.1007/s00445-003-0312-z

Saunders, J.A., Toran, L.E., 1995. Modeling of radionuclide and heavy metal sorption around low- and high- pH waste disposal sites at Oak Ridge, Tennessee. Applied Geochemistry 10, 673–684.

Schwertmann, U., 1958. The Effect of Pedogenic Environments on Iron Oxide Minerals, in: Stewart, B.A. (Ed.), Advances in Soil Science, Advances in Soil Science. Springer, New York, NY, pp. 171–200. https://doi.org/10.1007/978-1-4612-5046-3_5

Shoji, S., 1985. Genesis and properties of non-allophanic andisols in Japan. Applied Clay Science 1, 83–88. https://doi.org/10.1016/0169-1317(85)90564-2

Shoji, S., Dahlgren, R., Nanzyo, M., 1993a. Chapter 1: Terminology, Concepts and Geographic Distribution of Volcanic Ash Soils, in: Developments in Soil Science. Elsevier, pp. 1–5. https://doi.org/10.1016/S0166-2481(08)70262-9

Shoji, S., Dahlgren, R., Nanzyo, M., 1993b. Chapter 3 - Genesis of Volcanic Ash Soils, in: Developments in Soil Science. Elsevier, pp. 37–71. https://doi.org/10.1016/S0166-2481(08)70264-2

Shoji, S., Kodayashi, S., Yamada, I., Masui, J., 1975. Chemical and mineralogical studies on volcanic ashes I. Chemical composition of volcanic ashes and their classification. Soil Science and Plant Nutrition 21, 311–318. https://doi.org/10.1080/00380768.1975.10432646

Shoji, S., Nanzyo, M., Dahlgren, R., 1993c. Volcanic ash soils: Genesis, properties and utilization. Elsevier.

Shoji, S., Nanzyo, M., Dahlgren, R.A., Quantin, P., 1996. Evaluation and proposed revisions of criteria for Andosols in the World Reference Base for Soil Resources. Soil Science 161, 604–615. https://doi.org/10.1097/00010694-199609000-00005

Silber, A., Bar-Tal, A., 2008. Ch8. Nutrition of substrate-grown plants, in: Raviv, M., Heinrich Lieth, J. (Eds.), Soilless Culture. Theory and Practice. Academic Press, San Diego, pp. 291–340. https://doi.org/10.1016/B978-044452975-6.50010-1

Sklenář, P., Dušková, E., Balslev, H., 2011. Tropical And Temperate: Evolutionary History of Páramo Flora. The Botanical Review 77, 71–108. https://doi.org/10.1007/s12229-010-9061-9

Soil Survey Staff, 1999. Soil taxonomy: A basic system of soil classification for making and interpreting soil surveys. 2nd edition. Natural Resources Conservation Service. U.S. Departmenet of Agriculture Handbook 436.

Steefel, C., Depaolo, D., Lichtner, P., 2005. Reactive transport modeling: An essential tool and a new research approach for the Earth sciences. Earth and Planetary Science Letters 240, 539–558. https://doi.org/10.1016/j.epsl.2005.09.017

Steefel, C.I., 2009. CrunchFlow. Software for Modeling Multicomponent Reactive Flow and Transport . User's Manual.

Steefel, C.I., Appelo, C.A.J., Arora, B., Jacques, D., Kalbacher, T., Kolditz, O., Lagneau, V., Lichtner, P.C., Mayer, K.U., Meeussen, J.C.L., Molins, S., Moulton, D., Shao, H., Šimůnek, J., Spycher, N., Yabusaki, S.B., Yeh, G.T., 2015. Reactive transport codes for subsurface environmental simulation. Comput Geosci 19, 445–478. https://doi.org/10.1007/s10596-014-9443-x

Steefel, C.I., Lasaga, A.C., 1994. A coupled model for transport of multiple chemical species and kinetic precipitation/dissolution reactions with application to reactive flow in single phase hydrothermal systems. American Journal of Science 294, 529–592. https://doi.org/10.2475/ajs.294.5.529

Stefánsson, A., 2001. Dissolution of primary minerals of basalt in natural waters I. Calculation of mineral solubilities from 0 °C to 350 °C. Chemical Geology 172, 225–250.

Stefánsson, A., Gíslason, S.R., 2001. Chemical weathering of basalts, southwest Iceland: effect of rock crystallinity and secondary minerals on chemical fluxes to the ocean. American Journal of Science 301, 513–556. https://doi.org/10.2475/ajs.301.6.513

Takahashi, T., Shoji, S., 2002. Distribution and Classification of Volcanic Ash Soils 16.

Tonneijck, F.H., Jansen, B., Nierop, K.G.J., Verstraten, J.M., Sevink, J., De Lange, L., 2010. Towards understanding of carbon stocks and stabilization in volcanic ash soils in natural Andean ecosystems of northern Ecuador. European Journal of Soil Science 61, 392–405. https://doi.org/10.1111/j.1365-2389.2010.01241.x

Ugolini, F.C., Dahlgren, R.A., 2002. Soil Development in Volcanic Ash. Global Environmental Research 69–81.

Ugolini, F.C., Dahlgren, R.A., 1991. Weathering Environments and Occurrence of Imogolite/Allophane in Selected Andisols and Spodosols. Soil Science Society of America Journal 55, 1166–1171. https://doi.org/10.2136/sssaj1991.03615995005500040045x

van Hees, P.A.W., Lundström, U.S., 2000. Equilibrium models of aluminium and iron complexation with different organic acids in soil solution. Geoderma 94, 201–221. https://doi.org/10.1016/S0016-7061(98)00139-6

Wanner, C., Eggenberger, U., Mäder, U., 2012. A chromate-contaminated site in southern Switzerland – Part 2: Reactive transport modeling to optimize remediation options. Applied Geochemistry 27, 655–662. https://doi.org/10.1016/j.apgeochem.2011.11.008

White, A.F., Blum, A.E., Schulz, M.S., Bullen, T.D., Harden, J.W., Peterson, M.L., 1996. Chemical weathering rates of a soil chronosequence on granitic alluvium: I. Quantification of mineralogical and surface area changes and calculation of primary silicate reaction rates. Geochimica et Cosmochimica Acta 60, 2533–2550. https://doi.org/10.1016/0016-7037(96)00106-8

Wilson, J.C., Benbow, S., Metcalfe, R., 2018. Reactive transport modelling of a cement backfill for radioactive waste disposal. Cement and Concrete Research 111, 81–93. https://doi.org/10.1016/j.cemconres.2018.06.007

Wolery, T.J., 1992. EQ3NR, A Computer Program for Geochemical Aqueous Speciation-Solubility Calculations: Theoretical Manual, User's Guide, and Related Documentation (Version 7.0) (No. UCRL-MA-110662 PT III). Lawrence Livermore National Laboratory, Livermore, California. https://doi.org/10.2172/138643

Wolery, T.J., Jové Colón, C.F., 2017. Chemical thermodynamic data. 1. The concept of links to the chemical elements and the historical development of key thermodynamic data. Geochimica et Cosmochimica Acta 213, 635–676. https://doi.org/10.1016/j.gca.2016.09.028

Wolff-Boenisch, D., Gislason, S.R., Oelkers, E.H., Putnis, C.V., 2004. The dissolution rates of natural glasses as a function of their composition at pH 4 and 10.6, and temperatures from 25 to 74°C. Geochimica et Cosmochimica Acta 68, 4843–4858. https://doi.org/10.1016/j.gca.2004.05.027

Xu, T., Zheng, L., Tian, H., 2011. Reactive transport modeling for CO2 geological sequestration. Journal of Petroleum Science and Engineering 78, 765–777. https://doi.org/10.1016/j.petrol.2011.09.005

Yang, L., Steefel, C.I., 2008. Kaolinite Dissolution and Precipitation Kinetics at 22°C and pH 4. Geochimica et Cosmochimica Acta 72, 99–116. https://doi.org/10.1016/j.gca.2007.10.011

Yeh, G.-T., Tripathi, V.S., 1991. A Model for Simulating Transport of Reactive Multispecies Components: Model Development and Demonstration. Water Resour. Res. 27, 3075–3094. https://doi.org/10.1029/91WR02028

Zehetner, F., Miller, W.P., West, L.T., 2003. Pedogenesis of Volcanic Ash Soils in Andean Ecuador. Soil Sci. Soc. Am. J. 67, 1797–1809. https://doi.org/10.2136/sssaj2003.1797

Zhang, L., Soong, Y., Dilmore, R., Lopano, C., 2015. Numerical simulation of porosity and permeability evolution of Mount Simon sandstone under geological carbon sequestration conditions. Chemical Geology 403, 1–12. https://doi.org/10.1016/j.chemgeo.2015.03.014

Zimmer, K., Zhang, Y., Lu, P., Chen, Y., Zhang, G., Dalkilic, M., Zhu, C., 2016. SUPCRTBL: A revised and extended thermodynamic dataset and software package of SUPCRT92. Computers & Geosciences. https://doi.org/10.1016/j.cageo.2016.02.013

Annexes

Model M1

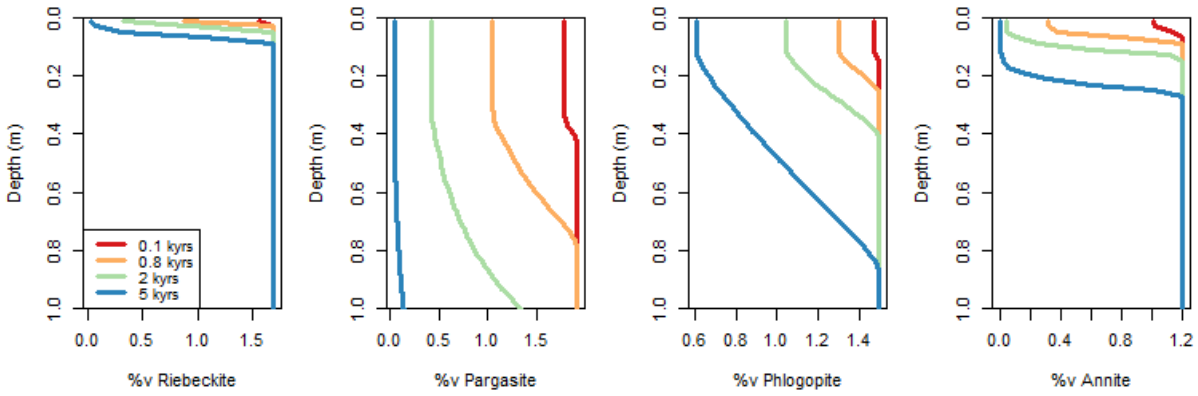

Figure A. 1. M1 modelled volume percentage of (a) riebeckite, (b) pargasite, (c) phlogopite, and (d) annite.

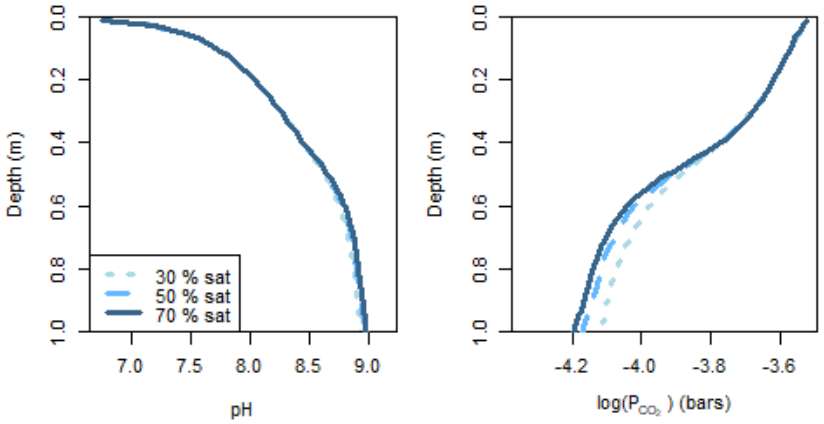

Figure A. 2. Effect of different water saturation level (30, 50 and 70 %) on (a) soil solution pH and (b) pCO_2 at 0.8 kyr, predicted by the M1 model.

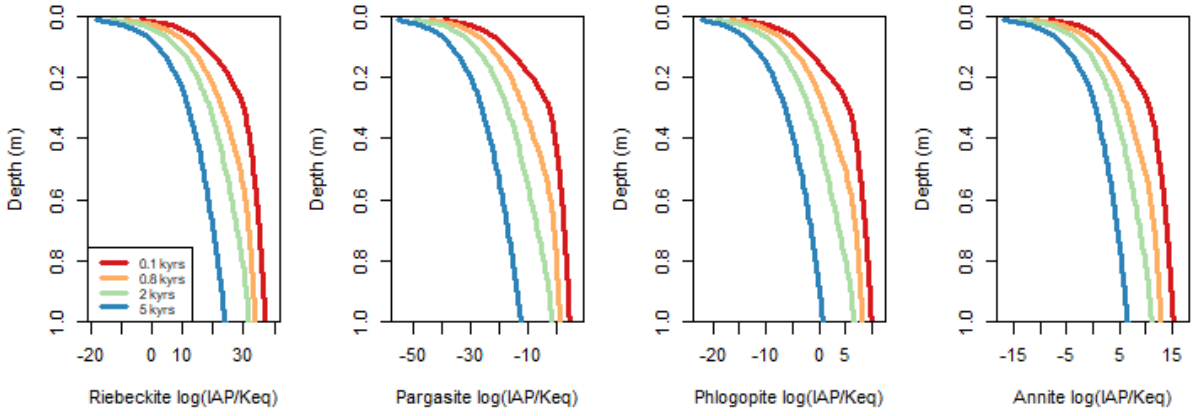

Figure A. 3. M1 modelled SI of: (a) riebeckite, (b) pargasite, (c) phlogopite, and (d) annite.

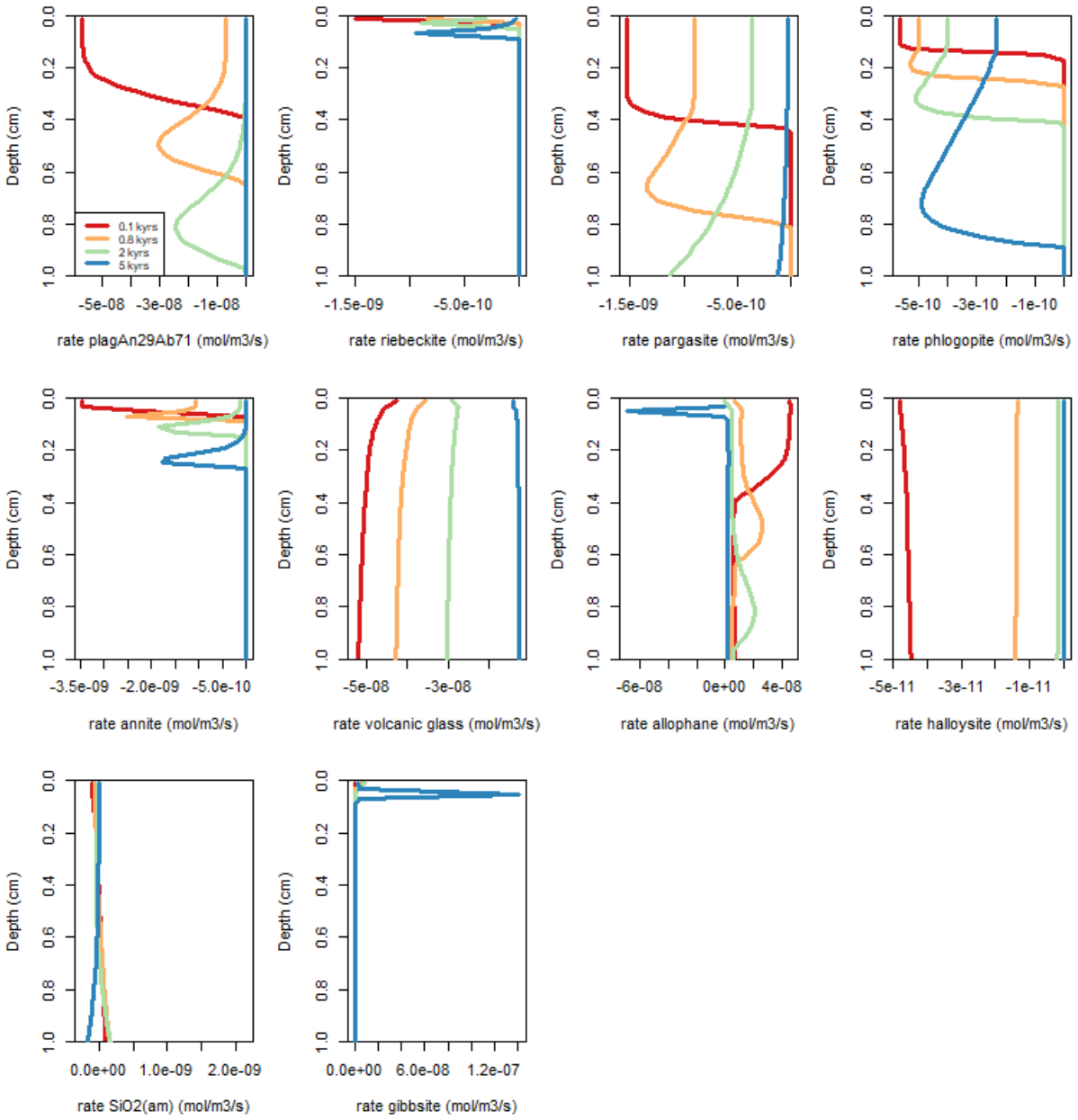

Figure A. 4. M1 model's prediction of the dissolution/precipitation rate of: (a) plagioclases, (b) riebeckite, (c) pargasite, (d) phlogopite, (e) annite, (f) volcanic glass, (g) allophanes, (h) halloysite, (i) $SiO_{2(am)}$ and (j) gibbsite.

Model M2

Model M2a

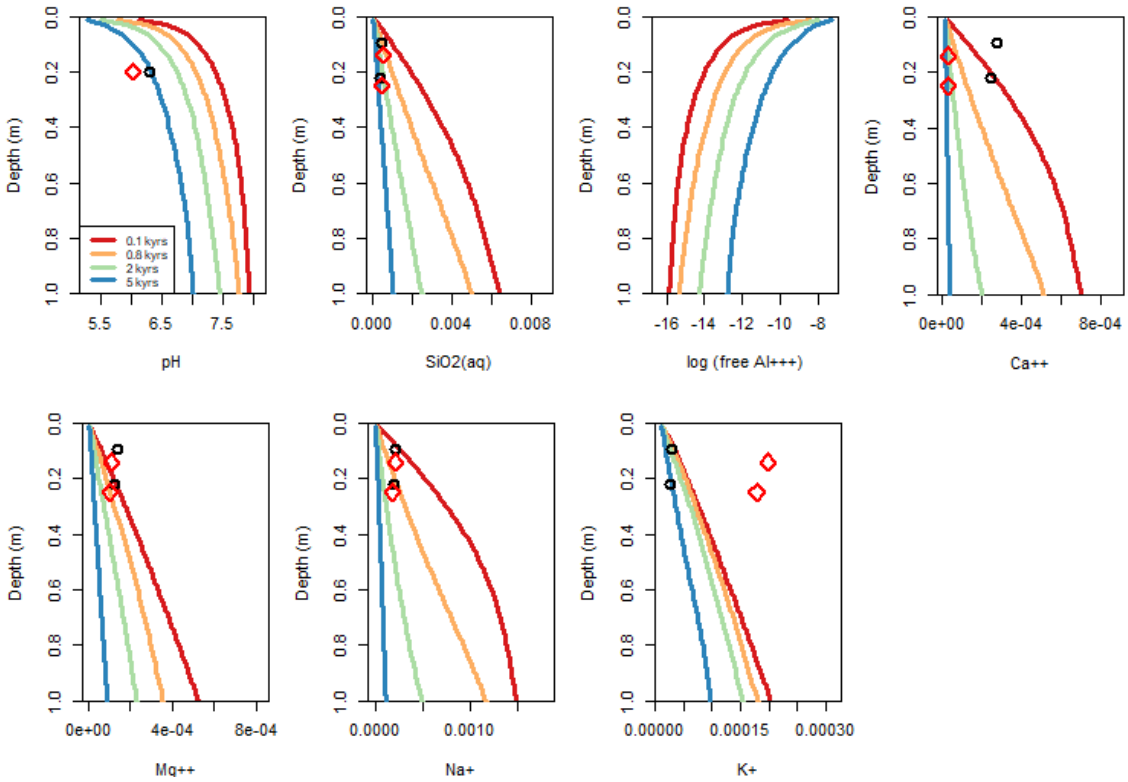

Figure A. 5. M2a model prediction of (a) pH, and concentrations in solution of (b) $SiO_{2(aq)}$, (c) free Al^{3+}, (d) Fe, (e) Ca^{2+}, (f) Mg^{2+}, (g) Na^{+}, and (h) K^{+}. Same legend as Figure 9.

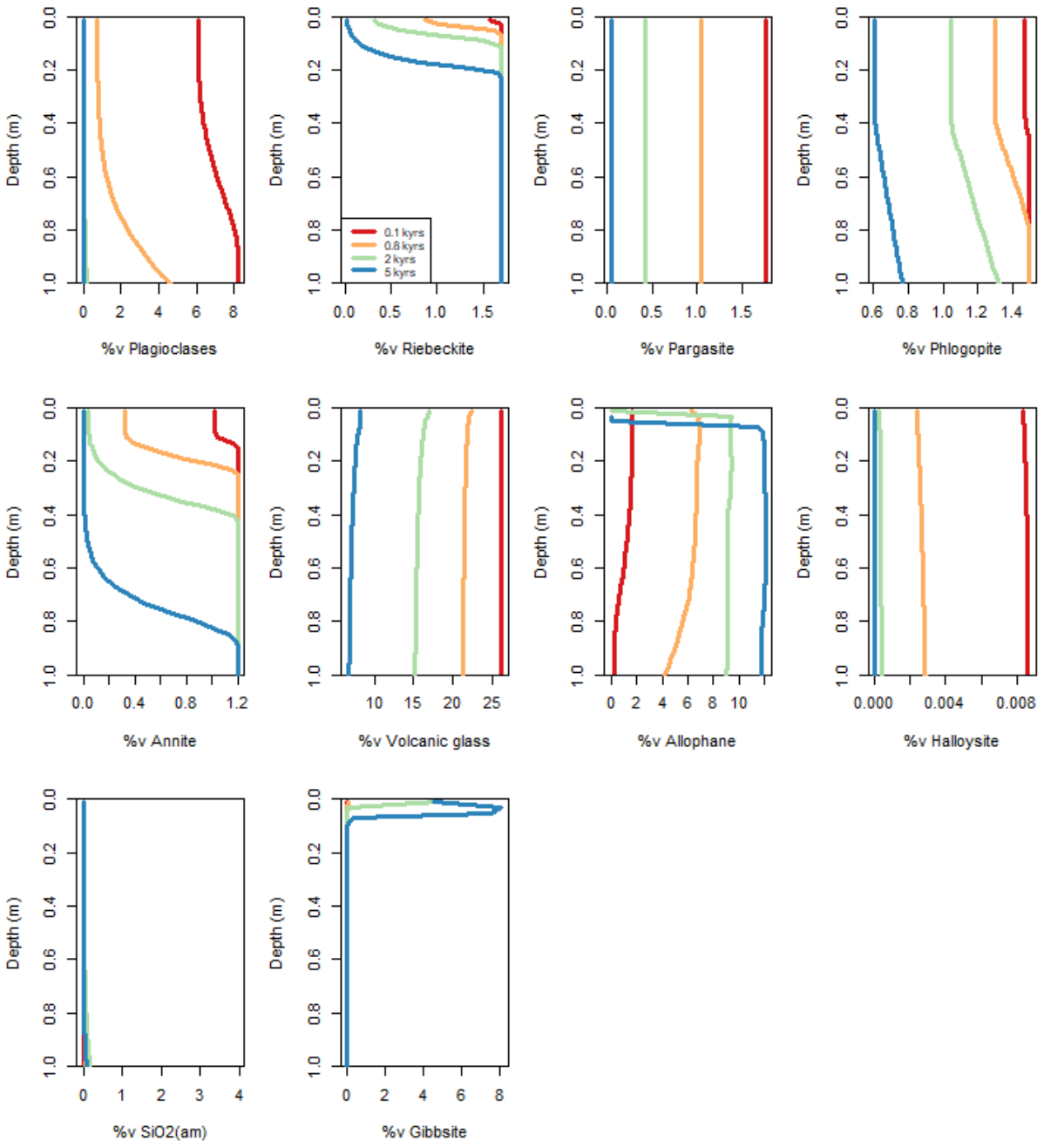

Figure A. 6. M2a modelled volume percentage of (a) plagioclases, (b) riebeckite, (c) pargasite, (d) phlogopite, (e) annite, (f) volcanic glass, (g) allophanes, (h) halloysite, (i) $SiO_{2(am)}$, and (j) gibbsite.

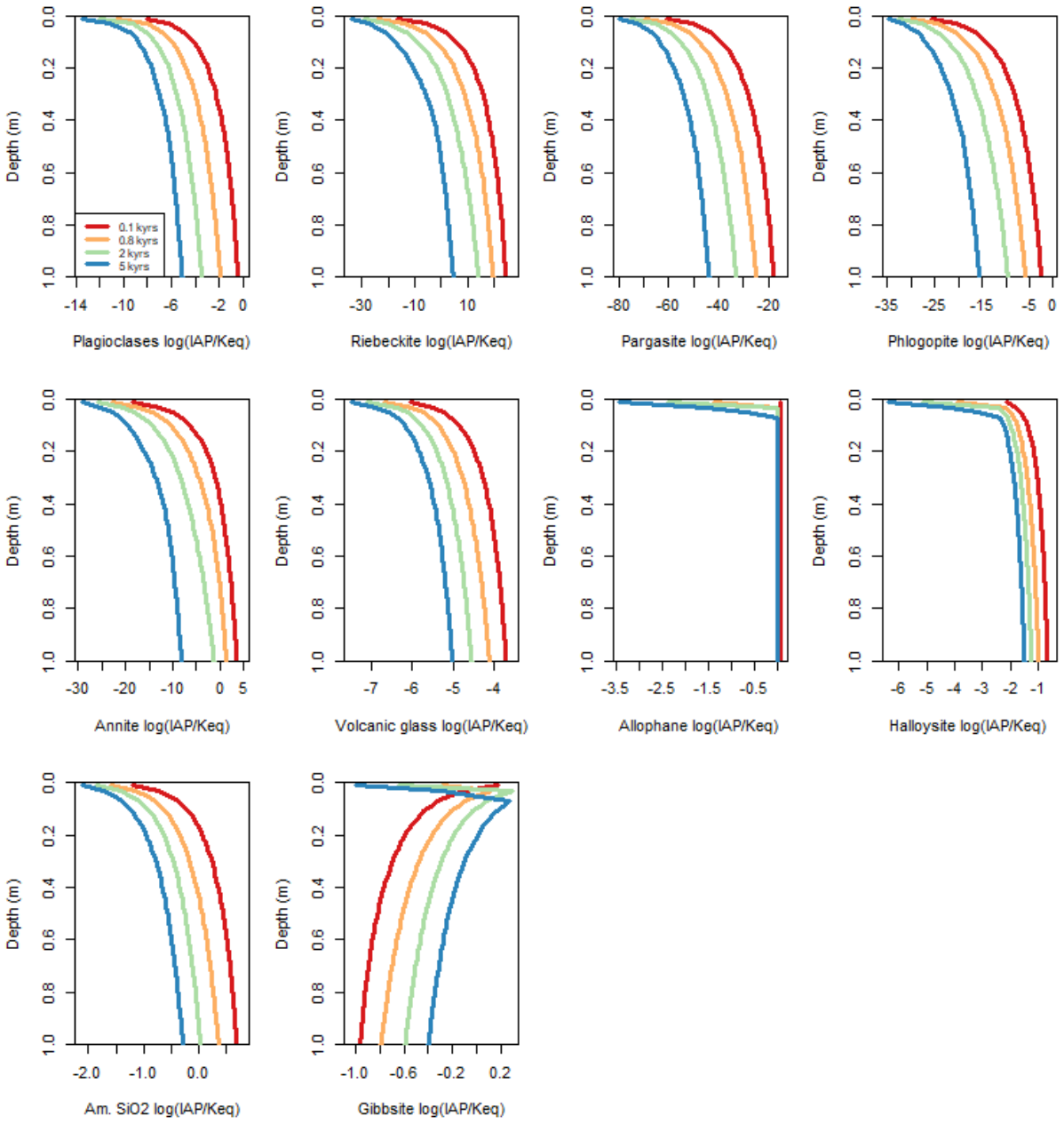

Figure A. 7. M2a model, saturation indexes of (a) plagioclases, (b) riebeckite, (c) pargasite, (d) phlogopite, (e) annite, (f) volcanic glass, (g) allophanes, (h) halloysite, (i) $SiO_{2(am)}$ and (k) gibbsite.

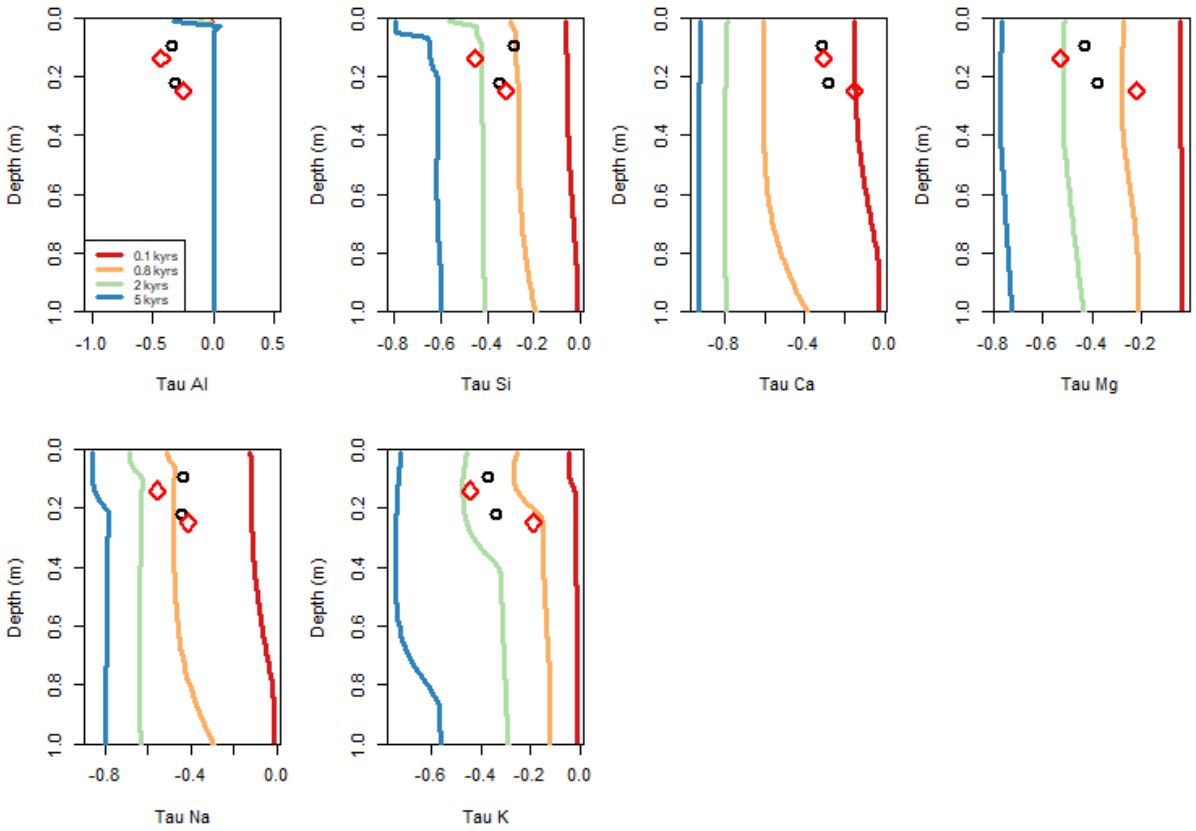

Figure A. 8. M2a model, mass-transfer coefficient of: (a) Al, (b) Si, (c) Ca, (d) Mg, (e) Na and (f) K. Same legend as Figure 9.

Model M2b

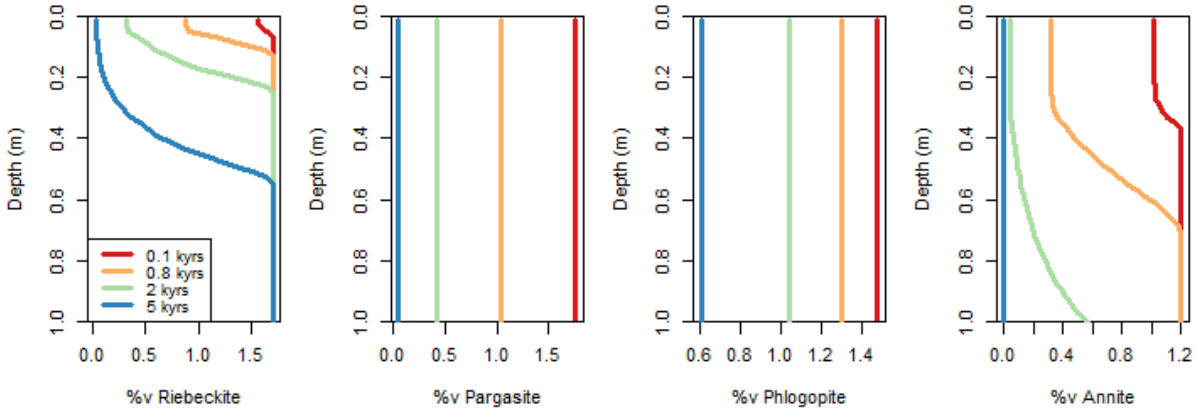

Figure A. 9. M2b modelled volume percentage of (a) riebeckite, (b) pargasite, (c) phologopite, and (d) annite.

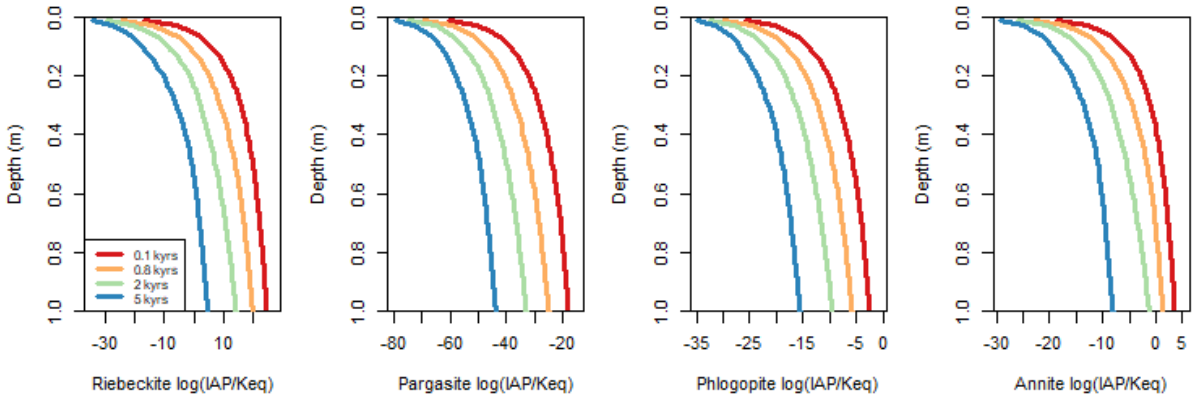

Figure A. 10. M2b model, saturation indexes of (a) riebeckite, (b) pargasite, (c) phlogopite and (d) annite.

Model M3

Model M3TU

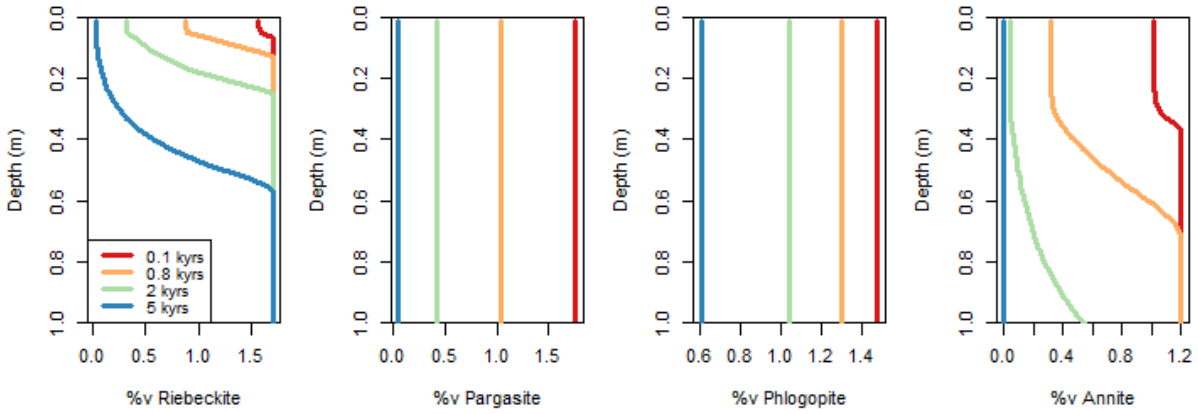

Figure A. 11. M3TU model's %v prediction for: (a) riebeckite, (b) pargasite, (c) phlogopite and (d) annite.

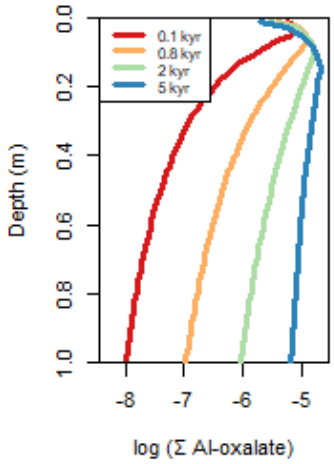

Figure A. 12. M3TU model's prediction of Al-oxalate complexes concentration.

Model M3CU

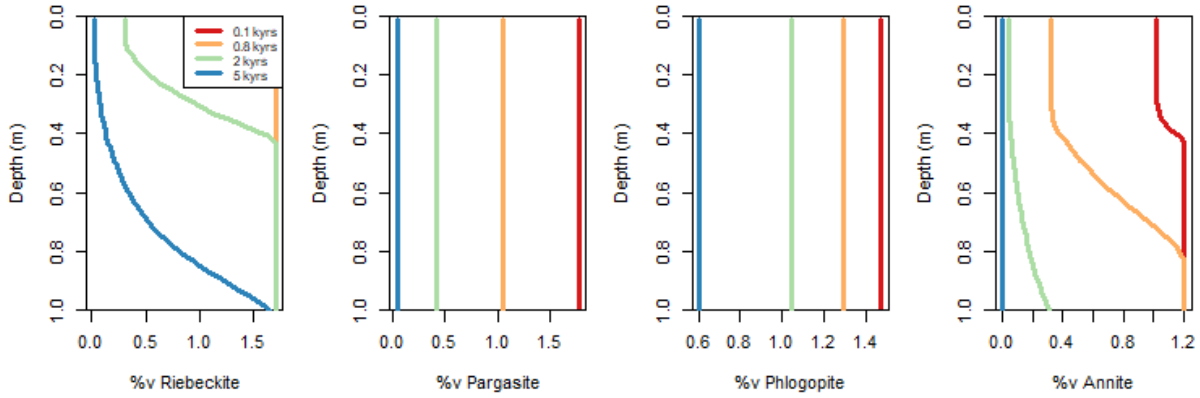

Figure A. 13. M3CU model's %v prediction for: (a) riebeckite, (b) pargasite, (c) phlogopite and (d) annite.

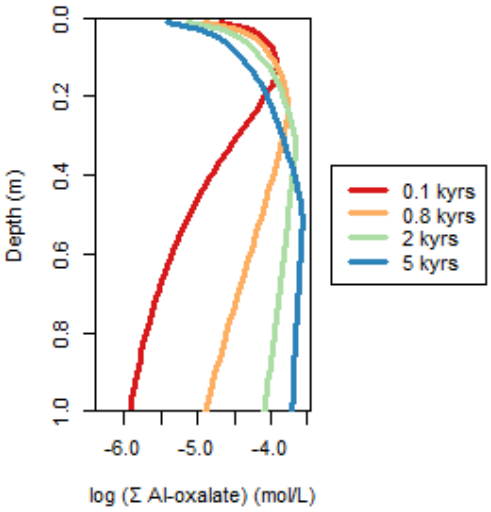

Figure A. 14. M3CU model's prediction of total Al-oxalate concentration in solution.

Model F1

Model F1TU

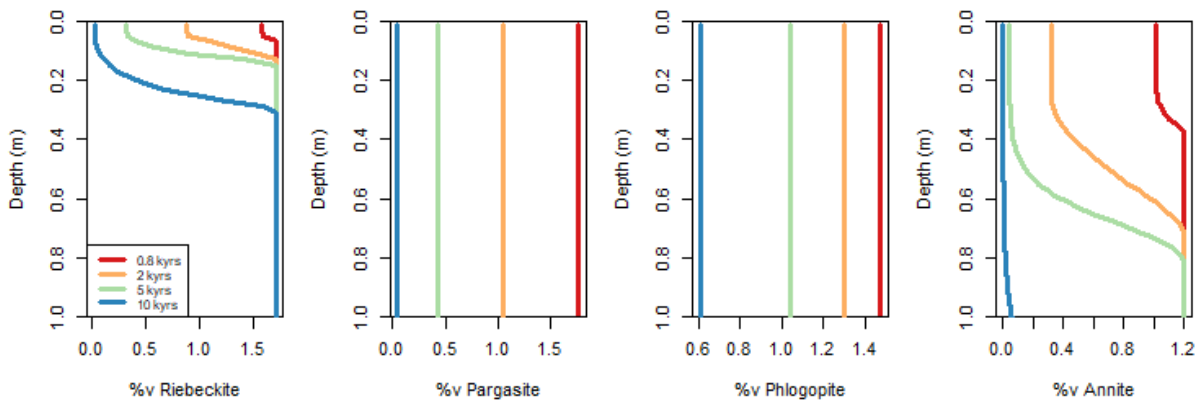

Figure A. 15. F1TU model's %v prediction for: (a) riebeckite, (b) pargasite, (c) phlogopite and (d) annite.

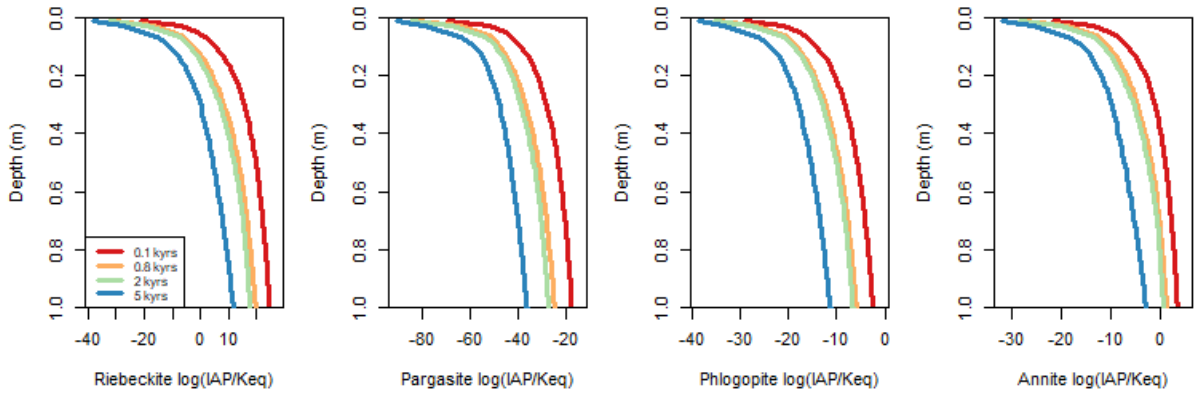

Figure A. 16. F1TU model's SI prediction for: (a) riebeckite, (b) pargasite, (c) phlogopite and (d) annite.

Model F1CU

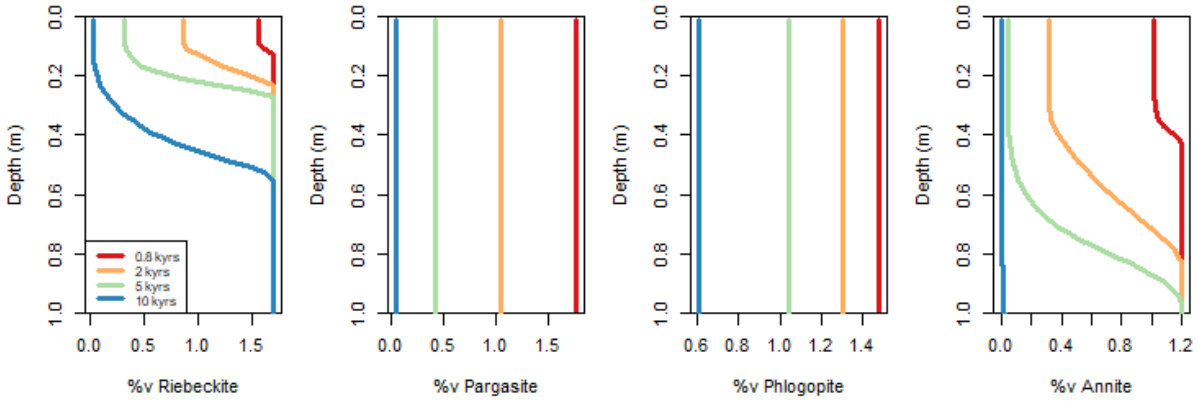

Figure A. 17. F1CU model's %v prediction for: (a) riebeckite, (b) pargasite, (c) phlogopite and (d) annite.

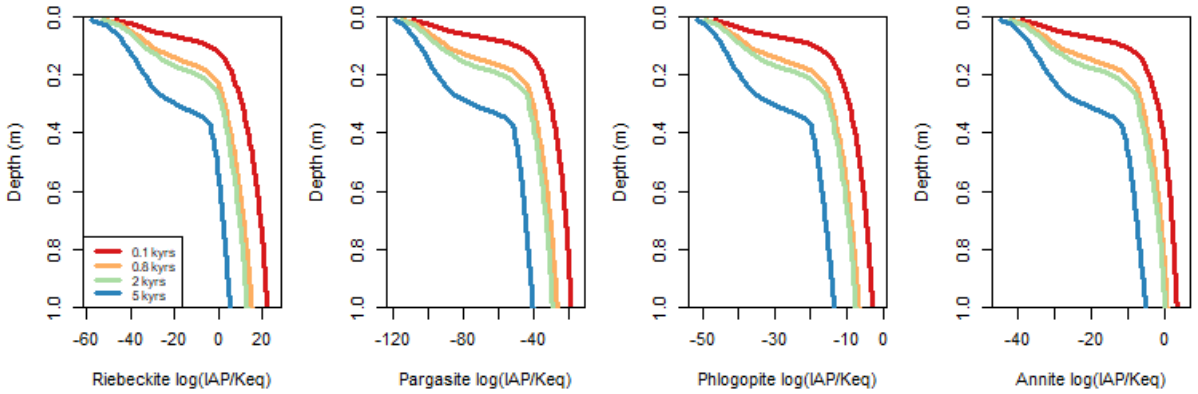

Figure A. 18. F1CU model's SI prediction for: (a) riebeckite, (b) pargasite, (c) phlogopite and (d) annite.

Model F2

Model F2TU

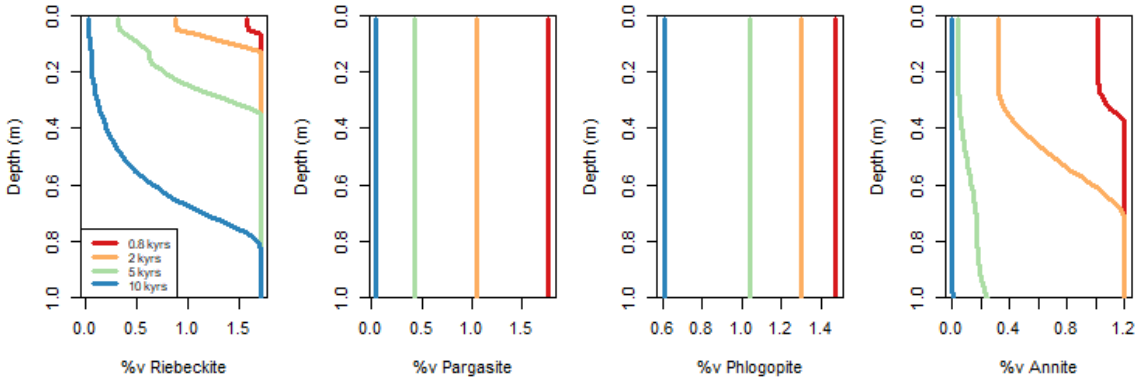

Figure A. 19. F2TU model's %v prediction for: (a) riebeckite, (b) pargasite, (c) phlogopite and (d) annite.

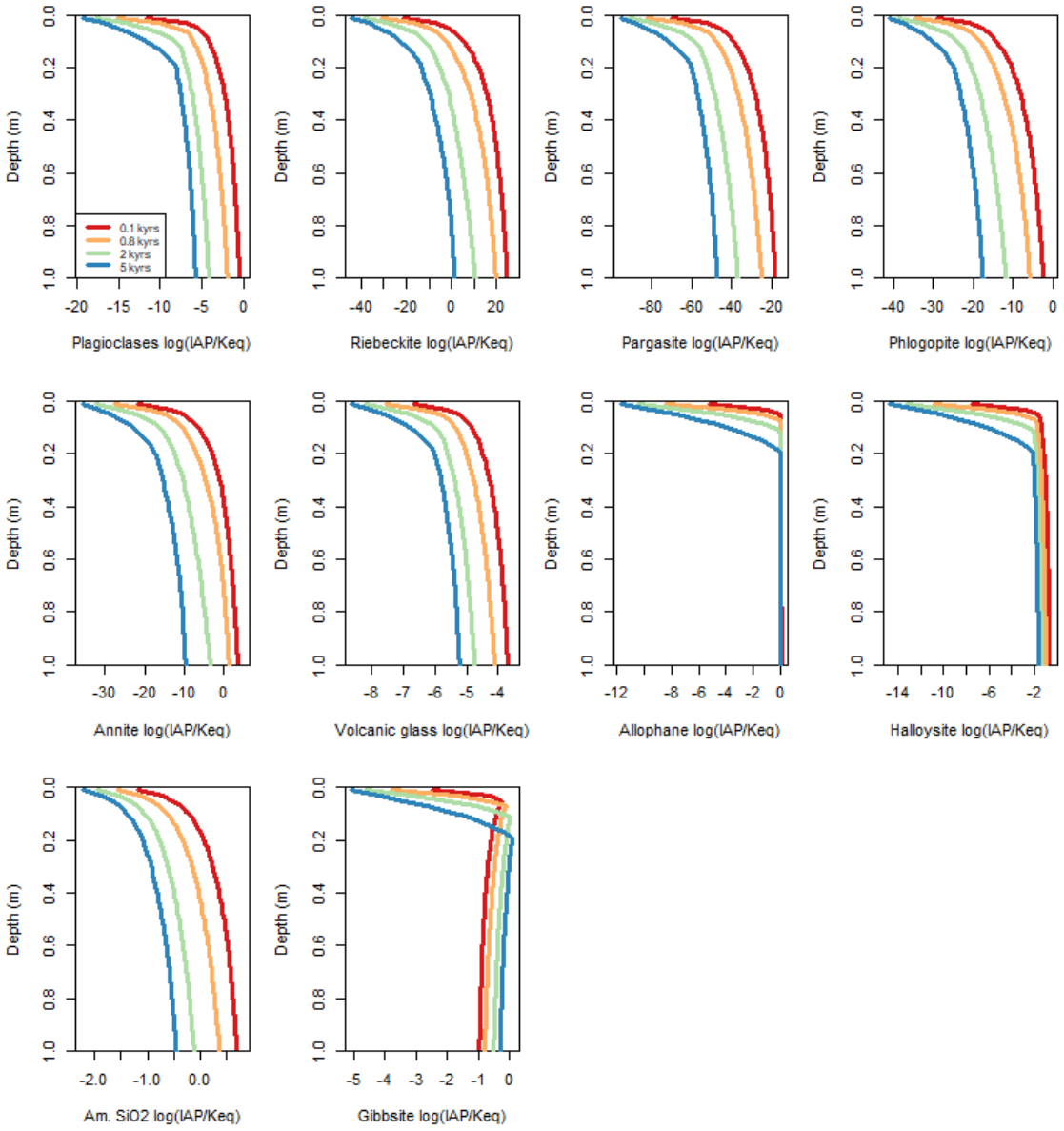

Figure A. 20. F2TU model prediction of the SI of: (a) plagioclases, (b) riebeckite, (c) pargasite, (d) phlogopite, (e) annite, (f) volcanic glass, (g) allophanes, (h) halloysite, (i) amorphous silica and (j) gibbsite.

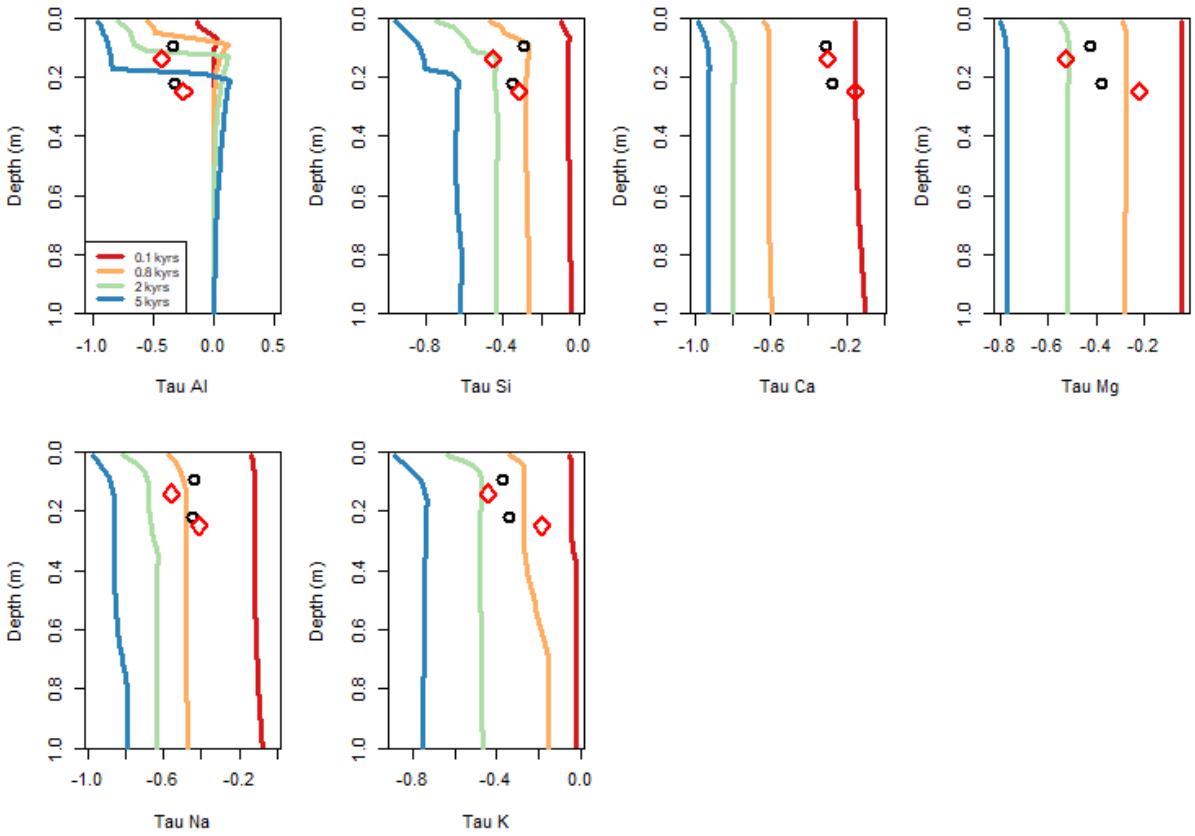

Figure A. 21. F2TU model's prediction of the mass-transfer coefficient τ of: (a) Al, (b) Si, (c) Ca, (d) Mg, (e) Na and (f) K.

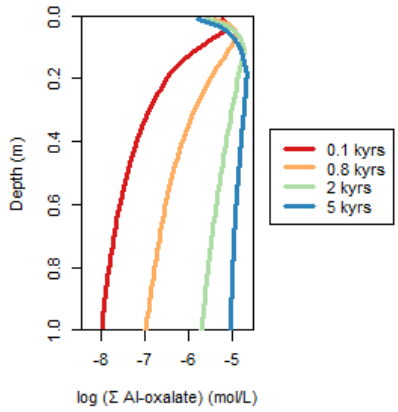

Figure A. 22. F2TU model's prediction of the total Al-oxalate concentration.

Model F2CU

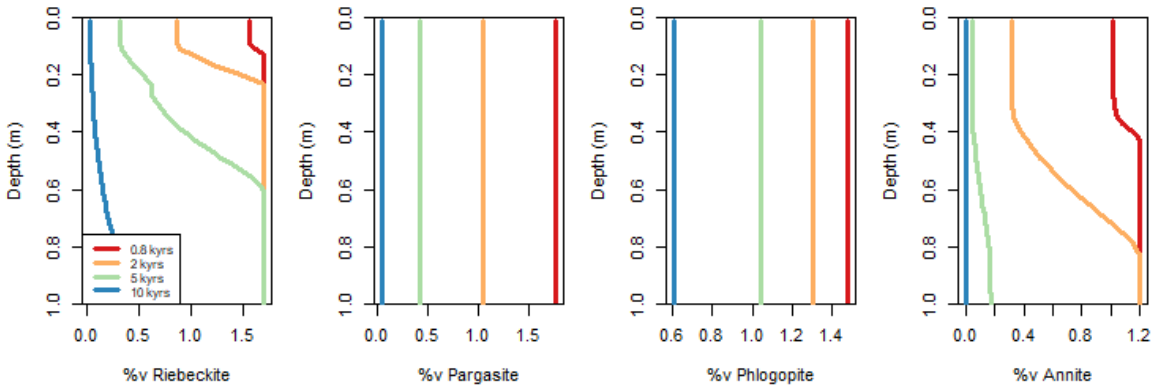

Figure A. 23. F2CU model's %v prediction for: (a) riebeckite, (b) pargasite, (c) phlogopite and (d) annite.

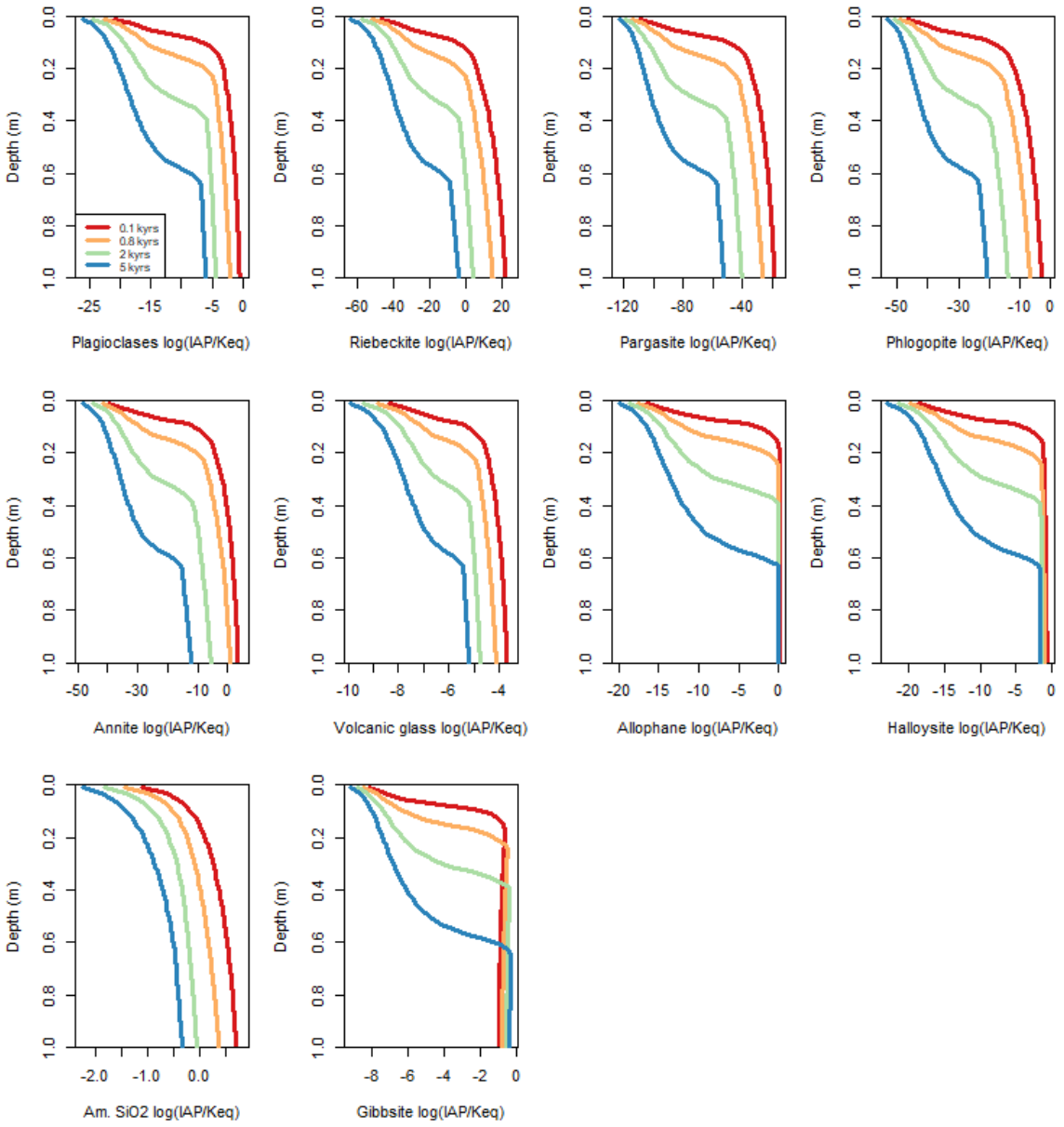

Figure A. 24. F2CU model prediction of the SI of: (a) plagioclases, (b) riebeckite, (c) pargasite, (d) phlogopite, (e) annite, (f) volcanic glass, (g) allophanes, (h) halloysite, (i) amorphous silica and (j) gibbsite.

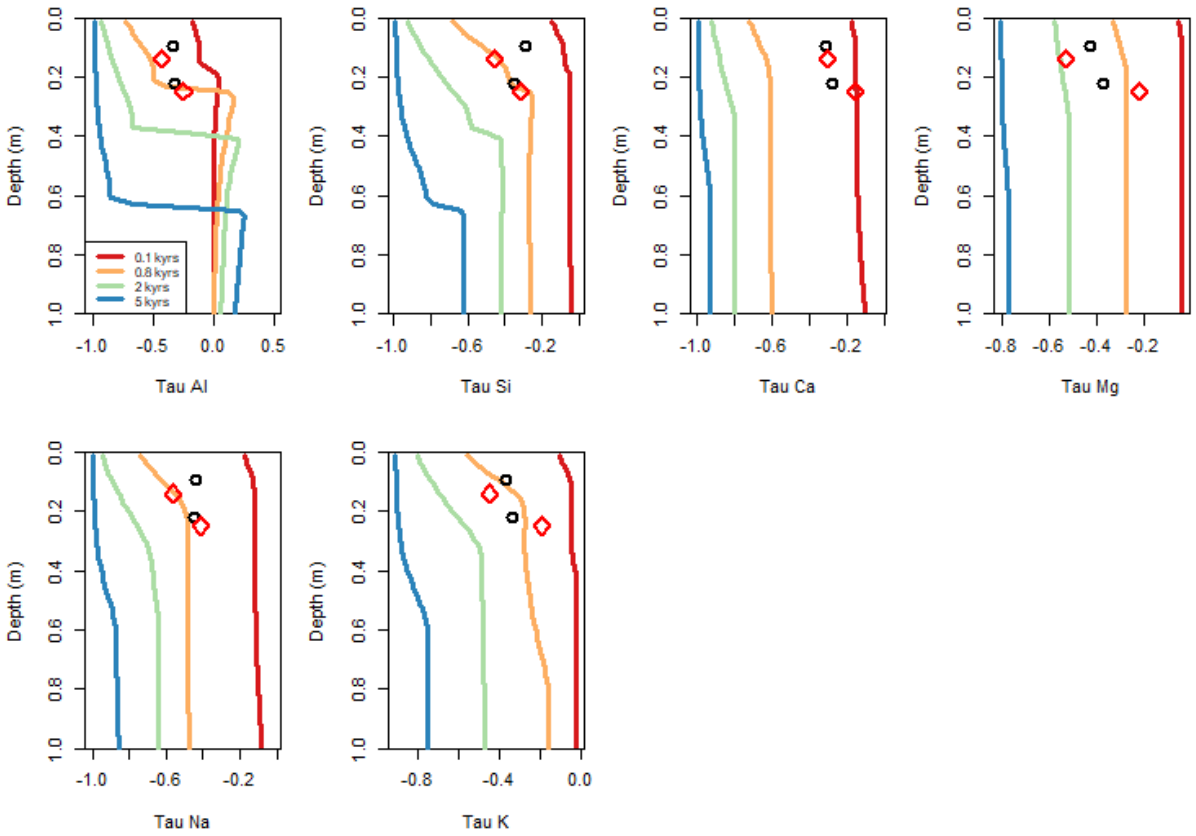

Figure A. 25. F2CU model's prediction of the mass-transfer coefficients τ of: (a) Al, (b) Si, (c) Ca, (d) Mg, (e) Na and (f) K.

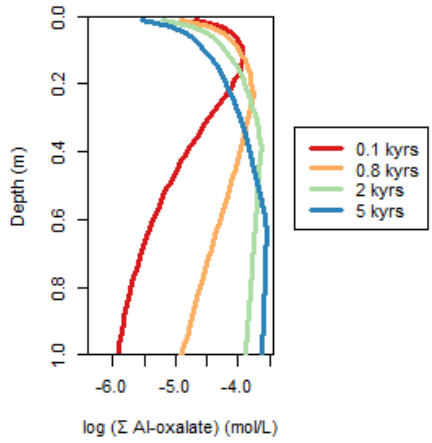

Figure A. 26. F2CU model's prediction of the total Al-oxalate concentration.

Model F3

Model F3TU

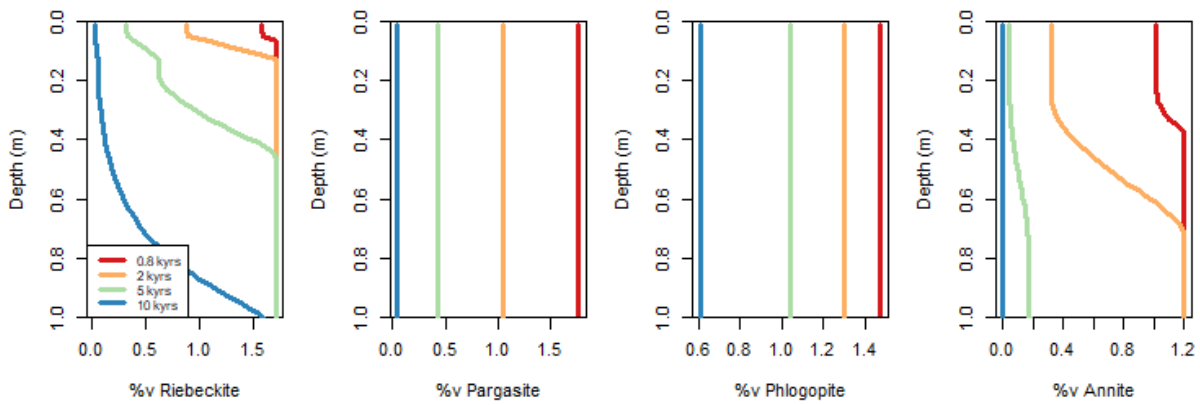

Figure A. 27. F3TU model's %v prediction for: (a) riebeckite, (b) pargasite, (c) phlogopite and (d) annite.

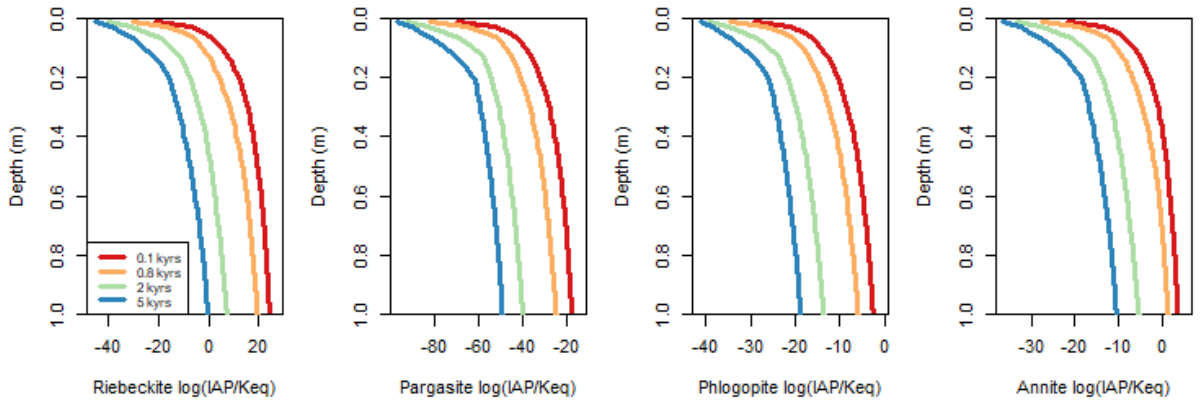

Figure A. 28. F3TU model's prediction of the SI of: (a) riebeckite, (b) pargasite, (c) phlogopite and (d) annite.

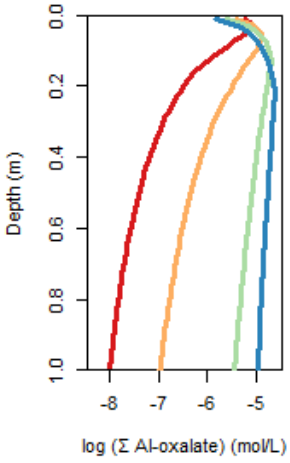

Figure A. 29. F3TU model's prediction of the total Al-oxalate concentration.

Model F3CU

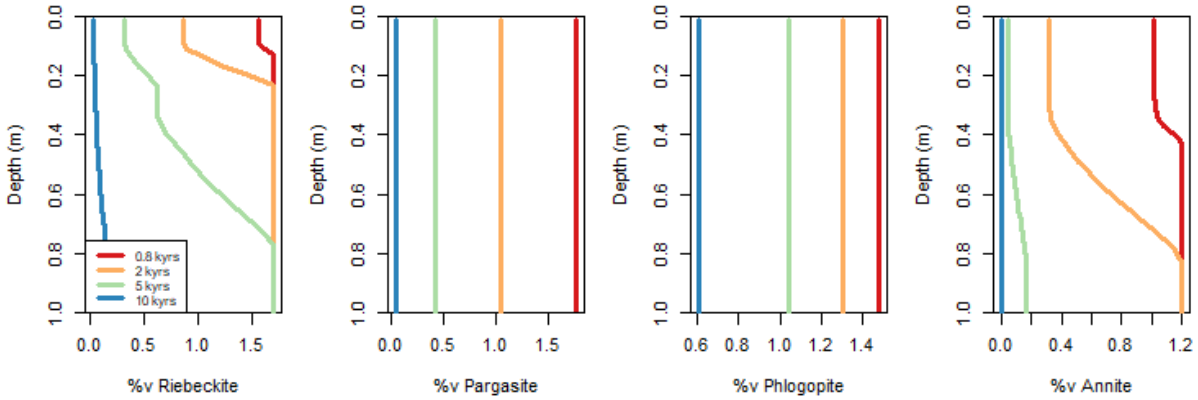

Figure A. 30. F3CU model's %v prediction for: (a) riebeckite, (b) pargasite, (c) phlogopite and (d) annite.

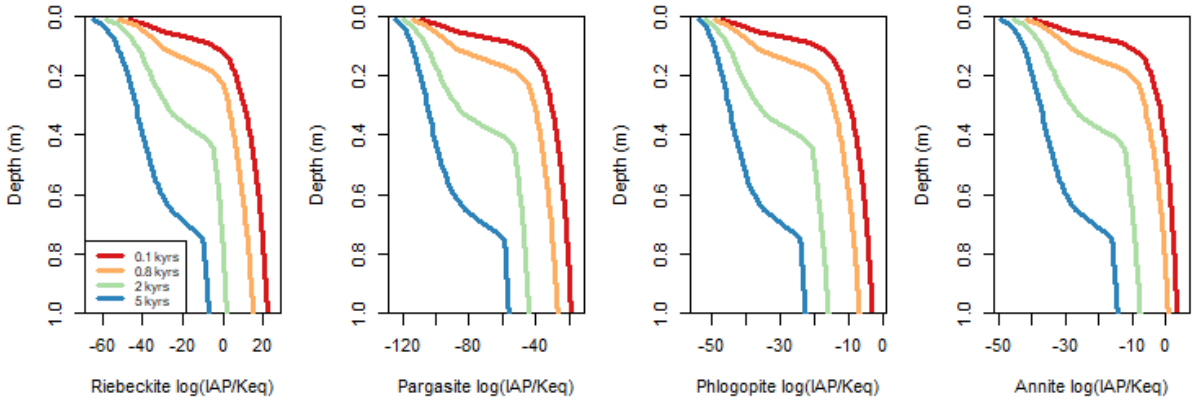

Figure A. 31. F3CU model's prediction of the SI of: (a) riebeckite, (b) pargasite, (c) phlogopite and (d) annite.

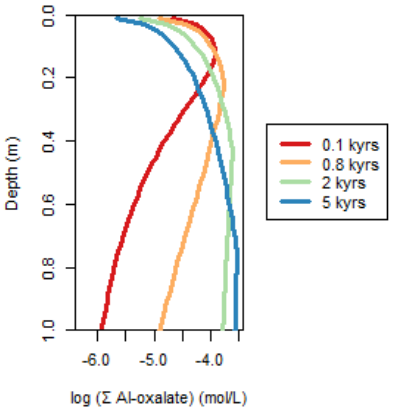

Figure A. 32. F3CU model's prediction of the total Al-oxalate concentration.

Tables

Table A. 1. Oxide dissolution reactions and equilibrium constants used for dacitic glass log K calculations at different temperatures (Aradóttir et al., 2012).

All oxides are from EQ3/6 database (Wolery, 1992) except SiO2(am) which is from (Gunnarsson and Arnórsson, 2000).

Oxide	Dissolution Reaction	Log K_i (25 °C)
SiO2(am)	$SiO_{2(aq)} = SiO_{2(aq)}$	-2.714
Al2O3 (Corundum)	$Al_2O_3 + 5H_3O = 2Al(OH)_4^- + 2H^+$	-60.369
FeO	$FeO + 2H^+ = Fe^{2+} + H_2O$	13.532
MgO (Periclase)	$MgO + 2H^+ = Mg^{2+} + H_2O$	21.355
CaO (Lime)	$CaO + 2H^+ = Ca^{2+} + H_2O$	32.576
Na2O	$Na_2O + 2H^+ = 2Na^+ + H_2O$	67.427
K2O	$K_2O + 2H^+ = 2K^+ + H_2O$	84.041

Table A. 2. Aqueous chemistry used in the model based on Minteq database (Morrey et al., 1985)

Complex reaction	Log K_{eq} (25 °C)
Fe-Oxalate → Fe^{3+} + $Oxalate^{2-}$	-9.15
Fe-$(Oxalate)_2^-$ → Fe^{3+} + 2 $Oxalate^{2-}$	-15.45
Fe-$(Oxalate)_3^{3-}$ → Fe^{3+} + 3 $Oxalate^{2-}$	-19.83
Al-Oxalate → Al^{3+} + $Oxalate^{2-}$	-7.73
Al-$(Oxalate)_2^-$ → Al^{3+} + 2 $Oxalate^{2-}$	-13.41
Al-$(Oxalate)_3^-$ → Al^{3+} + 3 $Oxalate^{2-}$	-17.09
Al-H-$Oxalate^{2+}$ → Al^{3+} + H^+ + $Oxalate^{2-}$	-7.46
Al-OH-$Oxalate_{(aq)}$ + H^+ → Al^{3+} + H_2O + $Oxalate^{2-}$	-2.57
Al-OH-$(Oxalate)_2^{2-}$ + H^+ → Al^{3+} + H_2O + $Oxalate^{2-}$	3.12
Al-$(OH)_2$-$(Oxalate)^-$ + $2H^+$ → Al^{3+} + H_2O + 2$Oxalate^{2-}$	-6.84

Modelling the influence of organic acids and rainfall inputs on the weathering of a volcanic ash deposit: a case study in the northern Ecuadorian Andes

Marion Junique

Abstract

The páramo in the tropical Andes is notable for its large water retention capacity, its high soil carbon content and rich biodiversity. The resulting ecosystem is the main source of water for many large Latin America cities. The current climate change affects these regions with predicted rainfall pattern alterations. In addition, human activities may lead to modifications in vegetation cover. However, very little is known about the impact of such changes on the weathering of the páramo soils. In this study, we innovatively used the reactive transport model approach to simulate the chemical weathering of a volcanic soil under different rainfall inputs and vegetation covers. We focus on the páramo of the Antisana region in northern Ecuador. Its soils developed on the ash deposit from the 800 years B.P. eruption of Quilotoa volcano.

Successive model versions were iteratively elaborated to progressively correspond to actual measurements of soil chemistry. The computer simulations were run using the Crunchflow engine and were based on a 1 m dacitic porous ash deposit reacting with an aqueous solution of rainfall composition (infiltration rate: 0.4 m/yr).

In order to take into account the soil respiration effect and to reproduce the pH values of the field soil solution, the CO_2 had to be increased 100 times (30 000 ppmv) compared to atmospheric CO_2. Due to the acidity consumption by the primary solid phases weathering, the pH increases with depth and decreases with time. Thus, the concentrations of $SiO_{2(aq)}$, Ca^{2+}, Mg^{2+}, Na^{+} and K^{+} increase with depth and decrease with time. Free Al^{3+} is the only cation which concentration decreases with depth and increases with time. Allophanes and gibbsite precipitation are visible.

Then, to represent the two different vegetation types, i.e. tussock-like grasses (TU, low DOC) and cushion-forming plants (CU, high DOC), oxalic acid was incorporated in the weathering solution in two different DOC concentrations. The soil solution pH under CU is lower and the mobilisation of Al is stronger, compared to under TU. Allophanes are the only secondary solid phases that precipitate (~12 %v at 5 kyr).

Once the model was tuned, different water flows were tested to study the impact of changing precipitation patterns on the soil solution and mineralogy. A double rainwater flow decreases slightly the soil solution pH under TU and up to 1.5 units under CU. It also decreases the concentrations of $SiO_{2(aq)}$, Ca^{2+}, Mg^{2+}, Na^{+} and K^{+} in solution, with a soil solution almost free of Ca^{2+} and Na^{+} after 5 kyr of weathering, but with a free Al^{3+} concentration at the bottom of the profile is 100 times higher under CU than under TU. The depth at which the allophanes precipitate is also lowered by respectively, 5 and 25 cm under TU and CU. On the contrary, decreasing the flow by half has an opposite effect: the pH and the dissolved element concentrations increase and the allophanes precipitate at shallower depths.

Further studies need to be carried out including for extrapolating consequences on the ecosystem and in particular on its water quality. However, it is also essential to significantly enrich the actual field data to further tune the model, specifically regarding pH, soil solution chemistry, as well as a robust determination of the water infiltration rate.

UNIVERSITÉ CATHOLIQUE DE LOUVAIN
Faculté des bioingénieurs
Croix du Sud, 2 bte L7.05.01, 1348 Louvain-la-Neuve, Belgique | **www.uclouvain.be/agro**